Structural controls and diagenetic conditions associated with fluid migration on the Moab Fault, UT

Keith R. Hodson

A dissertation

submitted in partial fulfillment of the

requirements for the degree of

Doctor of Philosophy

University of Washington

2018

Reading Committee:

Juliet G. Crider, Chair

Katharine W. Huntington

Darrel S. Cowan

Program Authorized to Offer Degree:

Earth and Space Sciences

University of Washington

Abstract

Structural controls and diagenetic conditions associated

with fluid migration on the Moab Fault, UT

Keith R. Hodson

Chair of the Supervisory Committee:

Juliet G. Crider

Department of Earth and Space Sciences

Faults and fault zones can have strong effects on fluid migration within the Earth's crust, with important implications for resource management and earthquake hazards. The research presented within this dissertation addresses the fluid migration history of the Moab Fault, Utah. Using the stable isotope compositions of fault-hosted carbonate cements in conjunction with field and petrographic observations, new insight is gained into the structural context, thermal and diagenetic conditions, and source fluids associated with cementation and vein formation along the fault zone. In particular, clumped isotope thermometry is used to directly estimate the formation temperature of carbonate minerals. Two generations of cement are identified, featuring distinct isotopic compositions, formation temperatures, and source fluids. The two cements are related to different styles of deformation within the fault zone, which we use to interpret the timing and burial conditions for both cementation and deformation. Spatial distributions of different cements suggest that the distribution of permeability was primarily controlled by fault-

segment interaction, producing localized zones of relatively intense deformation and fracturing. Relationships between carbonate and fluid isotopic compositions indicate that cementation and diagenesis occurred under rock-buffered conditions with low fluid-to-rock ratios.

Through the combination of clumped isotope thermometry with fluid inclusion microthermometry, a complementary thermometry method, a new approach is developed to aid in interpreting temperature measurements from carbonate veins. Expected relationships between these two methods allow a researcher to identify whether a measured temperature likely reflects primary crystal growth or secondary alteration. Additionally, the combination of these methods allows for the estimation of the fluid pressure associated with crystal growth, which may help identify elevated geothermal gradients or pressure conditions during the seismic cycle.

Included with this thesis are two supplementary files with additional data tables for chapters three and four. Supplementary tables for chapter three include a list of all replicate clumped isotope analyses, bulk isotope analyses, and recalculated data discussed in the text. Supplementary tables for chapter four include a list of all measurements of carbonate standards used in the study, a list of all replicate clumped isotope analyses, and a list of individual fluid inclusion measurements for each sample.

Acknowledgements

First, I would like to thank my academic advisor, Juliet Crider, for being an unwavering source of support, guidance, and wisdom over the last five years. Thank you as well to my committee members, Katharine Huntington and Darrel Cowan, for their help developing my research goals and directing my progress to meet them. Big thanks to Andrew Schauer, Julia Kelson and Casey Saenger for their help in IsoLab, particularly with the interpretation of carbonate standards, and to Patrick Leutkemeyer, Alex Lechler, Kyle Samek, William Keller, and Patrick Milstead for their help in the field and in the lab. Thank you to Charlotte Schreiber for her invaluable guidance on petrographic interpretation and reliably good conversation. Big thanks to Dennis Newell and David Brink-Roby for providing the fluid inclusion data that made my final chapter possible. I would like to thank the UW Department of Earth and Space Sciences for their academic and financial support throughout the course of my degree, and the American Chemical Society's Petroleum Research Fund, the National Science Foundation, and the Geological Society of America for providing the funding that made this research possible. Lastly, I would like to thank all my friends and family who have supported me along the way, including the ESS graduate student community, my parents, and my wife, Jess, to whom I owe the world.

Structural controls and diagenetic conditions associated with fluid migration on the Moab Fault, UT

Keith R. Hodson

Department of Earth and Space Sciences
University of Washington

Table of Contents

Chapter One

Introduction

Faults and fault zones are major structural discontinuities within the Earth's crust, fundamentally altering their host rock through deformation processes such as fracturing, brecciation, and localized grain size reduction. These mechanical processes go hand-in-hand with chemical processes such as diagenetic alteration and cementation, often driven by the migration of fluids along or across the fault zone (e.g. Laubach et al., 2010). Feedbacks and interrelationships between mechanical and diagenetic alteration are complex, but have important implications for the strength of the fault zone as well as the maintenance or loss of fault zone permeability to subsequent fluid flow. Because of these effects, the study of these combined processes, or "structural diagenesis", has important implications for fault hazard analysis as well as reservoir management within faulted aquifers or reservoir rocks. However, continued deformation and alteration during the lifespan of a fault system results in the evolution of fault strength and permeability. In this sense, the strength and permeability of a fault zone at any point in time is a function of that fault's integrated structural diagenetic history.

Modern permeability may be measured directly in the field or laboratory (e.g. Antonellini and Aydin, 1994), but these measurements cannot be taken as representative of the fault through time. Past permeability must be interpreted indirectly, commonly via the study of mineral cements and veins formed during episodes of fluid flow (e.g. Eichhubl et al., 2009). Within the three chapters of this dissertation, I use carbonate clumped isotope thermometry and traditional bulk stable isotopes of carbon and oxygen,

along with outcrop and thin-section observations, to interpret the conditions and timing for fluid migration and cementation along the Moab Fault in southeast Utah. This fault zone features excellent exposure and a wealth of prior research and characterization, making it an ideal target for our application of an emerging geochemical technique.

Since being introduced over a decade ago (Ghosh et al., 2006), clumped isotope thermometry has become a prominent stable isotope technique for interpreting the formation temperature of carbonate minerals. The power of the method comes from its dependence solely on temperature, as opposed to the combined dependence on temperature and source fluid composition for more routinely measured $\delta^{18}O$ compositions. Additionally, when combined with $\delta^{18}O$ measurements on the same sample, clumped isotope thermometry can allow estimation of the source fluid $\delta^{18}O$ composition (Kim and O'Neil, 1997). In this sense, properties that were previously assumptions can now become measureable aspects of a geochemical system. In the context of structural diagenesis, these properties allow us to interpret the thermal conditions and source fluids associated with fault zone cementation, which when combined with observations of the structural context can provide insight into the relationships between deformation and fluid flow, the depth and timing of cementation, and associated diagenetic processes.

In the first chapter of my dissertation, I present a detailed study of a prominent fault-segment intersection zone on the Moab Fault. At this locality, multiple deformation structures are readily observable across a well-exposed sandstone surface, including fractures and two styles of cataclastic deformation. Through careful inspection of the textural relationships between the deformation structures and distinct styles of

cementation, I link multiple episodes of cementation to distinct styles of deformation. Together, these data allow me to construct a combined deformation and fluid-migration history at the fault segment intersection, which I connect to the local burial history using temperatures determined from clumped isotope thermometry. This chapter was published in 2016 in a special issue of the journal Tectonophysics.

For the study presented in my second chapter, I return to the Moab Fault and use the combined deformation and cementation framework determined in chapter one to investigate larger-scale cementation patterns along the northern portion of the fault system. Samples distributed along the entire length of this portion of the fault span multiple distinct fault segments and intersection zones, featuring a range of fault displacements and sampled stratigraphic units. After determining sample context using the framework for chapter one, I explore the relationships between distinct cementation episodes and the variable displacement, lithologic, and structural geometry within the structure. I also use my temperature and stable isotopic compositions to model the diagenetic conditions along the fault, and provide evidence for low fluid-to-rock ratios and closed-system conditions during protracted post-faulting cementation. This chapter has been submitted to the journal Geological Society of America Bulletin, and is currently awaiting peer review.

In my third chapter, I present a study combining clumped isotope thermometry and fluid inclusion microthermometry; two complementary methods for estimating the formation temperature of carbonate minerals. Together, these methods provide a way to identify the presence of diagenetic alteration within a sample, providing additional support to an interpretation that measured temperatures truly reflect primary crystal

growth conditions. Additionally, the combination of these methods can provide information on the fluid pressure during crystal growth, which has implications for the depth, hydrologic conditions, and potentially fault behavior during cementation. I also present a statistical investigation of carbonate standards routinely measured during clumped isotope analysis, which I use to characterize the reproducibility of clumped isotope measurements in IsoLab at the University of Washington. Systematic biases towards lower temperature are evident from these data, and I propose a new standards-based correction method to compensate for measurement biases. This chapter is currently in preparation for publication in the scientific literature.

Together, these three chapters provide a new, clumped isotope perspective into the field of structural diagenesis. My ability to circumvent fundamental assumptions that were required for similar earlier studies has allowed me to characterize new aspects of the cementation history of the Moab Fault that would not have been previously possible. The methodologies presented in my third chapter address some of the major hurdles associated with the application of clumped isotope thermometry to higher-temperature applications such as fault zone cementation, and will hopefully help future researchers correctly interpret clumped isotope measurements and uncertainties.

Chapter Two

Multi-stage cementation and paleo fluid temperature in a faulted sandstone reservoir, Moab Fault, Utah, USA

2.0 - Abstract

Fluid-driven cementation and diagenesis within fault zones can influence host rock permeability and rheology, affecting subsequent fluid migration and rock strength. However, there are few constraints on the feedbacks between diagenetic conditions and structural deformation. We investigate the cementation history of a fault-intersection zone on the Moab Fault, a well-studied fault system within the exhumed reservoir rocks of the Paradox Basin, Utah, USA. The fault zone hosts brittle structures recording different stages of deformation, including joints and two types of deformation bands. Using stable isotopes of carbon and oxygen, clumped isotope thermometry, and cathodoluminescence, we identify distinct source fluid compositions for the carbonate cements within the fault damage zone. Each source fluid is associated with different carbonate precipitation temperatures, luminescence characteristics, and styles of structural deformation. Luminescent carbonates appear to be derived from meteoric waters mixing with an organic-rich or magmatic carbon source. These cements have warm precipitation temperatures and are closely associated with jointing, capitalizing on increases in permeability associated with fracturing during faulting and subsequent exhumation. Earlier-formed non-luminescent carbonates have source fluid compositions similar to marine waters, low precipitation temperatures, and are closely associated with deformation bands. The deformation bands formed at shallow depths very early in the

burial history, preconditioning the rock for fracturing and associated increases in permeability. Carbonate clumped isotope temperatures allow us to associate structural and diagenetic features with burial history, revealing that structural controls on fluid distribution are established early in the evolution of the host rock and fault zone, before the onset of major displacement.

2.1 - Introduction

Rock permeability is strongly influenced by deformation, with major implications for the paths and rates of fluid migration through the upper crust. Diagenetic processes coupled with structural deformation can have complex feedbacks, further affecting structurally enhanced permeability, as well as rheological properties of rocks (e.g. Laubach et al., 2010). As such, characterization of these processes can inform geologic models of fault zone evolution and fluid migration. Porous sandstones are important reservoirs for geologic fluids in the upper crust, making characterization of the interplay between brittle deformation and diagenesis in these rocks particularly relevant to predictions of fluid migration and storage (e.g. Eichhubl et al., 2004; Laubach et al., 2010; Balsamo et al., 2013).

Joints and deformation bands (DBs) are two styles of deformation structures commonly observed in porous sandstones. Jointing refers to mode-I (opening) fracturing of the host rock, while DBs include a family of mm- to cm-thick tabular structures with a range of deformation mechanisms and kinematics, including dilation, compaction and shear (e.g. Aydin et al., 2006; Fossen et al., 2007). Dilation associated with jointing

increases permeability of the host rock, creating conduits for fluid migration. Conversely, most types of DBs involve some degree of cataclasis, producing anastomosing zones of local grain size and porosity reduction (e.g. Aydin and Johnson, 1978; Antonellini et al., 1994). Some DBs are non-cataclastic, and may involve dilation and increases in permeability (e.g. Fossen et al., 2007). For cataclastic DBs, decreases in pore space can be quite substantial (e.g. Antonellini and Aydin, 1994; Eichhubl et al., 2009; Torabi et al., 2013) and have been commonly interpreted as an impedance to fluid flow (Knipe et al., 1997; Gibson, 1998). However, lateral outcrop-scale heterogeneities in DB zone continuity and thickness may diminish their effectiveness as barriers to fluid migration (e.g. Fossen and Bale, 2007). Furthermore, deformation bands may localize subsequent jointing (e.g. Tindall and Davis, 2003; Tindall and Eckert, 2015), enhancing cross-structure permeability (Tindall, 2014). Some DBs also develop band-parallel fracture networks, which may enhance band-parallel permeability (e.g. Johansen et al., 2005).

Cementation along a fault zone is a record of fluid migration through fractures and pore space (e.g. Sample et al., 1993; Ohtani et al., 2000; Kirschner and Kennedy, 2001; Graham Wall et al., 2006; Balsamo et al., 2012, 2013), as well as a record of the source fluid chemistry (e.g. McCaig et al., 1995; Parry, 1998; Chan et al., 2001, 2000; Ghisetti et al., 2001; Shipton et al., 2004; Eichhubl et al., 2009). Stable isotope analysis of carbonate cement can be a particularly powerful tool, as bulk carbon and oxygen isotope ratios ($\delta^{13}C$ and $\delta^{18}O$, where δ indicates the relative abundance of the heavy isotope relative to a standard) are sensitive to source fluid composition, mineral formation temperature, and diagenetic processes (Kim and O'Neil, 1997; Mook, 1986). The "clumped isotope" (or Δ_{47}) composition of carbonate cement describes the

abundance of carbonate ions containing both a heavy carbon and a heavy oxygen isotope (i.e., $^{13}C^{18}O^{16}O_2^{2-}$) relative to a stochastic distribution of isotopes. This isotope "clumping" is sensitive to temperature alone, and forms the basis of the carbonate clumped isotope paleothermometer (e.g. Ghosh et al., 2006; Schauble et al., 2006; Eiler, 2007, 2011). When conventional carbonate $\delta^{18}O$ measurements are paired with clumped isotope measurements, the relative influences of temperature and source-fluid composition on cement bulk isotope ratios can be determined. In the context of structural controls on fluid migration, paired temperature and source fluid composition provides insight into fault zone connectivity and thermal environments during cementation. When combined with micro-scale textural observations under polarized light and cathodoluminescence, the relative timing of cementation events during faulting, burial, and exhumation can be investigated (e.g. Loyd et al., 2012; Bergman et al., 2013; Budd et al., 2013; Huntington and Lechler, 2015).

Here, we use cements along the Moab Fault, southeast Utah, USA, to investigate the fluid migration history associated with the fault system. The surrounding Paradox Basin is interpreted to be an exhumed hydrocarbon system (e.g. Foxford et al., 1996; Nuccio and Condon, 1996), and the Moab Fault has hosted fluid migration within it. For this reason, the Moab Fault has been investigated by numerous workers interested in styles of structural deformation (e.g. Berg and Skar, 2005; Davatzes et al., 2005; Johansen et al., 2005) and their effects on fluid flow and associated carbonate cementation (e.g. Chan et al., 2000; Garden et al., 2001; Eichhubl et al., 2009; Bergman et al., 2013). Detailed mapping of structural (Davatzes et al., 2005; Johansen et al., 2005) and cementation patterns (Eichhubl et al., 2009) around a major fault-segment

intersection along the Moab fault, referred to herein as Courthouse Junction (CHJ), provides an exceptional framework to investigate the interplay between structure and diagenetic cementation. We build upon earlier work at CHJ, using carbonate clumped isotope thermometry to identify relationships between carbonate cementation temperature, stable isotope composition, and structural history of the fault zone. Carbonate cementation at CHJ occurred during at least two discrete episodes, spanning a range of formation temperatures. Source fluids differed between episodes of cementation, including both marine and meteoric compositions. We connect the episodes of cementation to the stages of structural deformation along at CHJ, providing a view into fault zone development in conjunction with fluid-driven cementation and diagenesis, constrained by structural relationships, fluid temperature and stable isotopes. Deformation bands, formed at shallow depths, appear to precondition rock for fracturing, leading to increased fault parallel permeability early on in the rock burial history.

2.2 - Geologic Setting of the Moab Fault

The Moab Fault is a NNW trending, ~45 km-long, normal fault system within the Paradox Basin of southeast Utah, USA (Fig. 2.1). The fault offsets a package of Pennsylvanian to Cretaceous sedimentary strata, deposited in basins associated with the ancestral and modern Rocky Mountain orogenies (Foxford et al., 1996) and salt diapirism within the Paradox Formation (Trudgill, 2011). Salt upwelling along the Moab Fault occurred throughout the Permian and Triassic (Trudgill, 2011). Dissolution of the Moab salt wall led to the eventual collapse of overlying strata (Gutiérrez, 2004), driving displacement along the Moab Fault beginning sometime after the late Triassic (Foxford et

al., 1996; Trudgill, 2011). Fault throw has a maximum of ~1 km at the central portion of the southern segment, decreasing northwards to ~300 m near Courthouse Junction (Foxford et al., 1996). The main phase of slip accumulation is taken to be coeval with peak burial during the early Tertiary (Nuccio and Condon, 1996; Foxford et al., 1996), an interpretation that is supported by fault-gouge dates of 63 to 43 Ma (Pevear et al., 1997; Solum et al., 2005).

The main unit sampled in this study is the Jurassic Moab Tongue Member of the Curtis Formation (Doelling et al., 2001), a very well sorted, ~30 m thick, quartz sandstone. The unit is composed of eolian dunes and interdune sediments with 17-25% porosity in undamaged rock, decreasing to as low as 1% in deformation bands around the Moab Fault (Eichhubl et al., 2009; Antonellini et al., 1994; Johansen et al., 2005). Liesegang banding is common in the area surrounding the fault zone, likely associated with observed bleaching of hematite grain coatings (Chan et al., 2000; Eichhubl et al., 2009; Garden et al., 2001).

Courthouse Junction (CHJ) and Mill Canyon represent zones of structural complexity associated with the linkage of fault segments. At CHJ, concentrated deformation is exposed in a ~2 hectare surface of Moab Tongue sandstone within a prism bounded on two sides by fault segments M1 and M2 (Fig. 2.2). Mill Canyon is flanked by an extensional relay zone in segment M2 to the east, and another major fault segment intersection to the west. Detailed structural mapping of exposures at CHJ and Mill Canyon by previous workers identified four classes of deformation structures, including joints, two types of cataclastic deformation bands, and jointed deformation bands (Figs. 2.3 and 2.4; Davatzes et al., 2005; Johansen et al., 2005). The styles of deformation band

are distinguishable in outcrop by their widths, termed “thick” and “thin” by Johansen et al. (2005). Thick deformation bands (DBk) contain limited cataclasis, with crushed grains occupying spaces between undeformed grains. Thin deformation bands (DBn) appear in thin section as discrete, narrow zones with intense comminution. (We use the last letter of “thick” and “thin” in the abbreviations, because the initial letters are the same.) Johansen et al. (2005) observed that DBn cross-cut DBk, interpreting the change in DB style to reflect changes in confining pressures and rock stiffness associated with burial and quartz diagenesis. DBn accommodate subsequent shear along joints formed within and adjacent to the zones of intense grain-size reduction, and the joints were subsequently filled by carbonate cement.

Both quartz and carbonate cements are present within the Moab Tongue sandstone at CHJ and Mill Canyon (Eichhubl et al., 2009) and elsewhere along the Moab fault (Chan et al., 2000; Garden et al., 2001). Eichhubl et al. (2009) noted that some joints are only partially filled by carbonate, concluding that the carbonate fills formed within an open joint network. Stable isotope and fluid inclusion studies from this part of the Moab Fault showed that carbonate cements have a range of isotope compositions, suggesting at least two different fluid sources for the cements, with at least one in conjunction with hydrocarbons (Chan et al., 2000; Garden et al., 2001; Eichhubl et al., 2009; Bergman et al., 2013). Clumped isotope thermometry identified cements that precipitated at warm and cool temperatures, with apparent structural control on the relative distribution of the two fluids (Bergman et al., 2013). We evaluate these relationships by combining clumped isotope measurements with microstructure observations, placing each carbonate into

context with the known burial history and evolving style of structural deformation at CHJ and Mill Canyon.

2.3 - Sample collection and characterization

We collected samples for bulk and clumped stable isotope analyses and thin section analysis. The samples were selected to provide both broad spatial coverage across CHJ and to represent the range of cementation styles associated with the four classes of deformation structures documented at CHJ and Mill Canyon: thick and thin deformation bands, jointed thin deformation bands, and joints not related to deformation bands.

Thin sections were prepared from 59 sandstone samples. Petrographic observations were made using a standard transmitted-light microscope and a Luminoscope ELM-3R cold-cathode catholuminescence stage (operated between 5 and 10 kV, ~0.5 mA, 50-100 millitorr), attached to a polarizing microscope fitted with an Olympus UC50 digital camera. We characterized cements in thin section based on their textural relationships to the four classes of deformation structures and by their luminescence. These observations were used to screen a subset for clumped isotope analysis, targeting samples exclusively containing either non-luminescent or luminescent carbonate.

2.4 - Stable Isotope Methodology

Prior to analysis, hand samples were cut or broken to isolate carbonate associated with particular features of interest identified in thin section and hand sample, and then ground using an agate mortar and pestle. Large carbonate features were separated from

the host rock before grinding. Given the mass of calcite needed for clumped isotope analysis (6-8 mg pure calcite equivalent per replicate), carbonate from thin veins or pore-filling cements was ground and homogenized with host rock with a bulk volume sufficient to yield the necessary mass of carbonate. Samples with paired observations of cathodoluminescence were taken from the same structures characterized in thin section.

All stable isotope analyses were performed at IsoLab at the University of Washington. Bulk carbon and oxygen isotope analyses ($\delta^{13}C$ and $\delta^{18}O$) were made using a Kiel III Device connected to a Thermo Scientific Delta Plus isotope ratio mass spectrometer using the methods of Tobin et al. (2011). Internal laboratory standards calibrated against NBS-18 and NBS-19 (IAEA, Vienna, Austria), and LSVEC (NIST, Gaithersburg, MD, USA) international standards were analyzed along with sample carbonates and used to convert measured isotope ratios to the Vienna Pee Dee Belemnite (VPDB) and Vienna Standard Marine Ocean Water (VSMOW) reference scales.

Samples for clumped isotope analysis (Δ_{47}) were first reacted with phosphoric acid at 90 °C, and the resultant CO_2 was prepared on an automated vacuum line following methods of Burgener et al. (2016). Details are provided in the Appendix. Purified gasses were then transferred to flame sealed glass tubes and stored until analysis on a dedicated Thermo MAT 253 isotope ratio mass spectrometer configured to measure *m/z* 44-49 (inclusive). Values for Δ_{47} were calculated using established methods (Huntington et al., 2009), and are reported in the absolute reference frame (Dennis et al., 2011) without a 25 °C correction for acid fractionation.

Values of Δ_{47} were converted to temperatures ($T\Delta_{47}$) using the calibration of Kluge et al. (2015; their eq. 5). Since the introduction of carbonate clumped isotope

thermometry (Ghosh et al., 2006; Eiler, 2007), a number of calibrations have been proposed linking Δ_{47} measurements to temperature (e.g. Ghosh et al., 2006; Guo et al., 2009; Dennis and Schrag, 2010; Eagle et al., 2010; Zaarur et al., 2013; Kluge et al., 2015). Differences among these calibrations are topics of ongoing research (e.g. Defliese et al., 2015; Kluge et al., 2015; Tripati et al., 2015). The calibration of Kluge et al. (2015) was chosen because it is the most recent version using materials and procedures most similar to our own: inorganic calcite and an elevated acid digestion temperature (90 °C). Differences in the slopes and intercepts of published calibration curves produce differences in $T\Delta_{47}$, and a graphical comparison of the two most used calibrations is provided in the supplementary materials. Because our findings are based principally on textural relationships and relative temperature, the interpretations presented are largely independent of our choice of calibration curve. A range of carbonate species has been observed at CHJ (e.g. calcite, ankerite, malachite), but because calcium carbonate speciation is not believed to significantly affect clumped isotope results (Defliese et al., 2015), we did not screen samples for mineralogy prior to analysis.

Simultaneous measurements of sample $\delta^{13}C$ and $\delta^{18}O$ made for each clumped isotope analysis were converted to VPDB and VSMOW reference scales using three internal laboratory standards calibrated to the NBS-18, NBS-19, and LSVEC international standards. For all but one sample, two to three replicate analyses were performed. Errors in $\delta^{13}C$, $\delta^{18}O$, temperature and derived fluid $\delta^{18}O$ values were determined using either the standard error of replicate sample analyses or the standard error of internal standards measured during the corresponding analysis period, whichever was larger.

2.5 - Results

2.5.1 - Textural Relationships

All four types of structures described by Johansen et al. (2005) were identified in outcrop at Courthouse Junction and Mill Canyon (Fig. 2.3). We observed the same cross-cutting relationships between these structures described by Johansen et al. (2005) and Davatzes et al. (2005), progressing from early thick deformation bands to thin deformation bands, followed by development of joints and thin veins in the cores of DBn, and finally to the formation of joints and veins not associated with deformation bands.

Thick deformation bands (DBk) appear in thin section as zones of porosity reduction associated with pockets of crushed quartz grains and carbonate cement (Fig. 2.4A), analogous to the shear enhanced compaction bands of Eichhubl et al. (2010). As compared to thin deformation bands (DBn) that form discrete ribbons of cataclasis (Fig. 2.4B), DBk are less distinct in thin section. Carbonate cements associated with DBk appear to be concentrated within the zones of grain-size reduction. DBn can contain opening mode I microfractures in and along their cores, with smaller fractures commonly bridging larger through-going fractures (Figs. 2.4B and 2.4C). Carbonate fills these joints to form thin veins (Fig. 2.4C), suggesting cement formation spanned the development of both DBk and DBn. Late stage joints are generally filled by mm to cm wide syntaxial veins composed of blocky crystalline carbonate cement. Joint-filling calcite is commonly twinned, which we interpret to indicate some amount of strain accumulation after cementation (Fig. 2.4D).

Cathodoluminescence (CL) reveals the presence of both luminescent and non-

luminescent carbonate cement, both of which are present as pore-filling cements and within fractures (Fig. 2.5). Non-luminescent carbonate is typically finely crystalline, but also can have a reddish-brown, cloudy appearance in thin section under plane and polarized light (Fig. 2.5C, white arrow). Jointed DBn commonly contain non-luminescent carbonate cement. Non-luminescent carbonate also occurs as pore filling cement surrounding both DBn and DBk. Coarsely crystalline luminescent cement was observed filling late forming joints and infiltrating pore space in the surrounding host rock (Fig. 2.5). Patches of DBn material can be observed along the margins of some luminescent veins, indicating the luminescent cement also filled jointed DBn. Centimeter-scale spherical concretions within the host rock and cement halos along joints consistently contain luminescent cements.

A range of brightness was observed in luminescent cements, from a dim reddish orange to bright orange. Because CL emissions are primarily controlled by the carbonate's trace element composition (Boggs and Krinsley, 2006), these variations in luminescence suggest some variability in source fluid chemistry during the formation of luminescent veins and pore-filling cements. Some veins display clear CL zonation along sharp boundaries that do not correspond to current grain boundaries (Fig. 2.5H), which in conjunction with observed mechanical twinning indicates recrystallization after deposition. Other luminescent veins have irregular boundaries between zones with differing CL brightness (Fig. 2.5D), suggesting that successive phases of cementation partially dissolved and replaced earlier cements.

Quartz grains in the analyzed samples commonly exhibit signs of compaction and pressure solution in the form of interlocking grains and quartz overgrowths (Fig. 2.4).

Both luminescent and non-luminescent carbonate cements can be observed filling areas between previously interpenetrating grains, indicating cements with both CL characteristics formed after compaction (Fig. 2.5J shows a luminescent example). Some veins contain quartz grains suspended within the carbonate fill, such as the clastic dike described by Eichhubl et al. (2009) in the wall of Mill Canyon west of CHJ.

The relative age of luminescent and non-luminescent carbonate cements varies from sample to sample. First, non-luminescent cement that *predates* luminescent cement is observed both (1) as an earlier pore filling cement crosscut by later luminescent cement (Fig. 2.5A and B) and (2) along the margins of veins filled with younger luminescent carbonate (Fig. 2.5C and D). These veins can contain patches of comminuted grains along their margins, in the same style as DBn. The non-luminescent cements in this setting predate the luminescent vein fills, but must post-date the formation of DBn. Second, non-luminescent cement that *postdates* luminescent cement is also observed; non-luminescent cement occurs at the center of luminescent veins, filling fractures that crosscut earlier CL zonation (Fig. 2.5H). It seems that precipitation of non-luminescent cements occurred both before and after precipitation of the luminescent cements. We do not observe carbonate veins with alternating zones of luminescent and non-luminescent carbonate, nor have we found examples of mutual crosscutting in the same sample, suggesting that the phases of cementation did not overlap in time.

2.5.2 - Stable Isotope Geochemistry

2.5.2.1 - Bulk isotope measurements

We measured bulk carbon and oxygen stable isotope compositions on 31

individual samples (Table 1). Measured $\delta^{13}C$ values range from -5.2 to 4.0 ‰ VPDB, and measured $\delta^{18}O$ values range from -23.5 to 2.8 ‰ VPDB. $\delta^{13}C$ and $\delta^{18}O$ are positively correlated (Fig. 2.6A), similar to relationships described in earlier work at CHJ (Chan et al., 2000; Eichhubl et al., 2009; Bergman et al., 2013).

For a subset of samples, we have paired CL observations and isotope measurements. These analyses show that luminescent and non-luminescent carbonate cements have distinct $\delta^{13}C$ and $\delta^{18}O$ values (Fig. 2.6A). Samples containing luminescent carbonate have $\delta^{13}C$ values between -4.5 and -2.3 ‰ VPDB, and $\delta^{18}O$ values between -20.9 and -15.8 ‰ VPDB. Samples containing non-luminescent carbonate have higher $\delta^{13}C$ values between -0.7 and 3.2 ‰ VPDB, and higher $\delta^{18}O$ values between -5.0 and -0.1 ‰ VPDB.

2.5.2.2 - Carbonate clumped isotope thermometry

Out of the pool of samples with bulk isotope measurements, twenty-five samples were analyzed for clumped isotope thermometry (Table 1). For all but one sample (MCC15-KH05), reported values of Δ_{47} represent averages of 2 to 3 repeat measurements from the same sample. Sample average Δ_{47} values range from 0.505 to 0.681 ‰, corresponding to carbonate precipitation temperatures ($T\Delta_{47}$) of 7 °C to 73 °C (calibration of Kluge et al., 2015). Reported errors are the standard error for multiple replicate analyses from each sample or the long term standard deviation of an internal laboratory standard (1SD = 0.025 ‰) divided by the square root of the number of sample replicate analyses, whichever is larger. This produces sample specific uncertainty in $T\Delta_{47}$ between 4 and 14 °C (1SE, average of 6.8 °C)

Clumped isotope temperatures vary systematically with calcite luminescence, with non-luminescent carbonate yielding cool $T\Delta_{47}$ values (<18 °C), and luminescent carbonate showing higher $T\Delta_{47}$ values (>18 °C). Analyzed samples for which CL observations were not made have $T\Delta_{47}$ up to ~73 °C; bulk C and O isotopic compositions of these samples suggest they likely belong to the luminescent group (Fig. 2.6A). Using the temperature dependence of oxygen isotope fractionation between carbonate and water determined by Kim and O'Neil (1997), calculated parent fluid $\delta^{18}O$ values are between -16 and -13 ‰ VSMOW for luminescent carbonate, but higher for non-luminescent carbonate: -6 and 0 ‰ VSMOW (Fig. 2.6C). Errors in these values, based on standard error in measured temperatures, fall between 1 and 3 ‰.

2.6 - Discussion

The observation of strong correlations between carbonate $\delta^{18}O$ and $\delta^{13}C$ values, carbonate luminescence, carbonate precipitation temperature, and source fluid $\delta^{18}O$ values supports the interpretation that chemically and thermally distinct source fluids circulated at CHJ and Mill Canyon. The apparent association of luminescent and non-luminescent carbonate with different styles of structural deformation indicates that different source fluids are associated with different stages of structural deformation and the burial history. In the following discussion, we synthesize our findings with the known geologic history of the Moab Fault and Paradox Basin, providing constraints on the fluid sources for carbonate cement, the relative timing of cementation and structural deformation, and the thermal environments during burial and faulting.

2.6.1 - Fluid Sources

As outlined in section 5.2.1, bulk isotope data delineate two end-member carbonate cement compositions (Fig. 2.6A). Earlier studies identified similar ranges in oxygen and carbon isotope compositions at CHJ (Chan et al., 2000; Eichhubl et al., 2009), and $\delta^{13}C$ values as low as -15 ‰ have been reported from further south along the Moab Fault system (Garden et al., 2001). CL observations support the conclusion of two end-member compositions at CHJ, as luminescencent carbonates have consistently lower $\delta^{13}C$ and $\delta^{18}O$ values than non-luminescent carbonate (Fig. 2.6A). Inclusion of bulk isotope data from Bergman et al. (2013) with our results shows a continuous range of values between known luminescent and non-luminescent samples (Fig. 2.6). Known luminescent samples have relatively low bulk isotopic compositions and known non-luminescent samples have relatively high bulk isotopic compositions. This suggests that most of the observed spread can be attributed to the presence of both end-member carbonates within single samples at scales finer than the sample size.

Source fluid $\delta^{18}O$ values determined using TD_{47} also support the presence of two distinct end-member fluids. For our samples with known luminescence characteristics, there are two distinct source fluid $\delta^{18}O$ values: luminescent carbonate source fluids average approximately -13.5 ‰ and non-luminescent carbonate source fluids average approximately -3.3 ‰. Other source fluid $\delta^{18}O$ values from this study and Bergman et al. (2013, re-calculated using the temperature calibration of Kluge et al., 2015) fall between the end-members (Fig. 2.6), supporting the interpretation that many samples contain a mixture of luminescent and non-luminescent carbonate with these end-member isotopic

compositions. Bergman et al. (2013) report one exception to this pattern: a non-luminescent sample with a source fluid $\delta^{18}O$ value of -13 ‰.

Considering that equilibrium fractionation of carbon between solid and dissolved carbonate is minor (~1 ‰; Mook, 1986), our data highlight approximate isotopic compositions for the source fluids and their dissolved inorganic carbon (DIC) content: a $\delta^{18}O$ value of -13.5 ‰ VSMOW and $\delta^{13}C$ value of -3.2 ‰ VPDB for luminescent carbonate and a $\delta^{18}O$ value of -3.3 ‰ VSMOW and $\delta^{13}C$ value of 1.3 ‰ VPDB for non-luminescent carbonate (Fig. 2.6d). Through the application of clumped carbonate thermometry, we confirm the suggestions of earlier studies at CHJ, identifying fluids with distinct isotopic compositions that produced the observed carbonate cements (Chan et al., 2000; Eichhubl et al., 2009; Bergman et al., 2013). Isotopic evidence for fluid sources has been discussed at length in earlier studies at CHJ and the surrounding region (Shipton et al., 2004; Chan et al., 2000; Eichhubl et al., 2009; Garden et al., 2001; Crossey et al., 2009; Dale et al., 2014), and we use our new data to evaluate the range of possible sources.

2.6.1.1 - Possible carbon sources

Possible carbon sources for carbonate cements include marine waters, organic matter derived from plants, soil CO_2 from plant respiration, reduction of hydrocarbons, and magmatic degassing. Marine carbonates typically have $\delta^{13}C$ values between 0 and 4 ‰ VPDB (Shackleton, 1986), while $\delta^{13}C$ values between -30 and -20 ‰ VPDB are more typical of the latter three sources, although substantial enrichment in ^{13}C can occur due to complex microbial reactions (e.g. Irwin et al., 1977). Magmatic CO_2 typically has $\delta^{13}C$

values between -7 and -1 ‰ VPDB (e.g. Crossey et al., 2009; Hilton et al., 2010; Lucic et al., 2015).

Non-luminescent carbonates have $\delta^{13}C$ values within the range expected for a marine bicarbonate source. This follows the conclusion of Eichhubl et al. (2009) who attribute relatively high $\delta^{13}C$ values to marine DIC. The marine carbon could be derived from infiltrating marine waters as the Paradox Basin became flooded during the mid-Cretaceous (Trudgill, 2011), or could be from deeply circulating waters rich in dissolved limestone from Pennsylvanian, Permian, or Jurassic strata (Fig. 2.6A; Garden et al., 2001). Alternatively, modern CO_2-charged geysers and springs in the nearby Salt Wash Graben produce large surficial carbonate deposits with enriched $\delta^{13}C$ values (~4 to 8 ‰ VPDB; Fig. 2.6A; Shipton et al., 2004), and may be modern analogues for the formation of non-luminescent carbonate. Bacterial fermentation of organic carbon in the methanogenic zone (e.g. Dale et al., 2014; Irwin et al., 1977) is another possibility, predicted to produce $\delta^{13}C$ values between ~0 and 15 ‰.

Luminescent carbonate $\delta^{13}C$ values are below the typical range of marine DIC, but much higher than typical values for organic sources. Carbon sources for luminescent carbonate may have involved anoxic methanogenisis of organic acids, which can produce $\delta^{13}C$ values less than ~ -4 ‰ (Baedecker et al., 1993), as suggested by Eichhubl et al. (2009), or thermocatalytic decarboxylation of organic carbon ($\delta^{13}C$ less than ~ -3 ‰; Irwin et al., 1977), as was suggested by Dale et al. (2014) for concretions with similar $\delta^{13}C$ values in the Piceance basin ~50 km to the northeast of CHJ. Abundant spherical concretions at CHJ hint at microbe-assisted cementation, but $T\Delta_{47}$ shows that only half of the luminescent carbonates fall in the methanogenic temperature range (below ~40°C;

Irwin et al., 1977). The remaining luminescent carbonates have higher temperatures, consistent with thermal decomposition. Magmatic CO_2 associated with the intrusion of Oligocene Colorado Plateau laccoliths (Nelson et al., 1992) was determined by Crossey et al. (2009) to have $\delta^{13}C$ values between -9 to -3 ‰ VPDB, making waters charged with magmatic DIC another possible carbon source.

2.6.1.2 - Possible oxygen sources

Non-luminescent carbonates have $\delta^{18}O$ values similar to, but lower than modern (~0 ‰ VSMOW) and Cretaceous (~1.2 ‰ VSMOW; Shackleton and Kennett, 1975) ocean waters. This may suggest a mixed marine and meteoric oxygen source for non-luminescent carbonate. Carbonate associated with modern CO_2-charged geysers, which have similar $\delta^{13}C$ values to non-luminescent carbonates, have $\delta^{18}O$ values between ~-9 and -12 ‰ VPDB (Shipton et al., 2004), somewhat lower than non-luminescent carbonates, which might be attributable to differences in carbonate precipitation temperature or degassing of CO_2.

The source fluids associated with luminescent, relatively warm carbonates have $\delta^{18}O$ values around -13.5 ‰ VSMOW, within the range of $\delta^{18}O$ values from modern meteoric water (-15 to -12 ‰; Spangler et al., 1996). While we do not necessarily expect modern and Mesozoic meteoric water to be equivalent, the similarity suggests a primarily meteoric source for the oxygen in the luminescent carbonates. A similar conclusion was reached by earlier interpretations of carbonate $\delta^{18}O$ values from CHJ (Chan et al., 2000; Eichhubl et al., 2009).

2.6.1.3 - Source fluids at Courthouse Junction

Our new CL observations, structural observations, and chemical analyses allow us to describe the source fluids associated with the three stages of carbonate cements at CHJ. Measured non-luminescent carbonates have source fluids with $\delta^{18}O$ and $\delta^{13}C$ values similar to marine water and marine DIC. The association of early non-luminescent cements with the earliest deformation structures (DBk), cool $T\Delta_{47}$, and marine fluids suggests that these cements likely precipitated from intraformational marine waters during the earliest stages of diagenesis.

Luminescent carbonates are associated with joints, have warm $T\Delta_{47}$, and $\delta^{18}O$ within the expected range of meteoric water, consistent with deeply circulating basin water upwelling within the fault damage zone. The presence of warm meteoric waters, with associated carbonate temperatures reaching predicted ambient conditions during peak burial (Garden et al., 2001), follows the general framework proposed by Chan et al. (2000) and Eichhubl et al. (2009), where a carbon-rich, reducing fluid derived from hydrocarbons mixed with formation waters to form the (warm) carbonate cements. The presence of hydrocarbon residues within the Moab Fault Zone supports the interpretation that degraded hydrocarbons yielded the observed $\delta^{13}C$ values, but our data cannot rule out magmatic CO_2 as a possible carbon source.

Source fluids for late non-luminescent carbonate remain ambiguous. Because they are difficult to isolate from luminescent cement during sampling, we do not have isotopic analysis from non-luminescent samples with clear a cross-cutting relationship showing late relative age. Bergman et al. (2103) report a single non-luminescent specimen with a meteoric oxygen isotope signature and a cool $T\Delta_{47}$. That specimen and the specimen

shown in Fig. 2.5H (with late non-luminescent carbonate) are both from the intensely deformed damage zone near the fault (e.g. Fig. 2.3D). These observations support the interpretation that the high permeability damage zone served as a conduit for cool meteoric fluids (Bergman et al. 2013) or was active following exhumation to near-surface depths (Fig 2.8, box C).

2.6.2 - Thermal and structural context for carbonate deposition

Cool, non-luminescent cements are observed within DBk and jointed DBn, as well as in fractures cross-cutting warm, luminescent cements. Luminescent cements are found within joints as well as jointed DBn. By combining the established sequence of structural deformation (DBk, DBn, jointing of DBn, and jointing not associated with DBs) with the relative ages and contrasting temperatures of cool, non-luminescent and warm, luminescent cements, we can place the coupled structural and diagenetic history of the Moab sandstone at CHJ into the broader context of basin evolution and deformation on the Moab Fault (Fig 2.8).

Growth of the Moab Salt Wall ended by the late Triassic (Trudgill, 2011). The Moab Tongue sandstone was deposited last in a series of Jurassic eolian sandstones, marking the transition to the deposition of lacustrine and fluvial sediments (Trudgill, 2011). Catacastic DBs have been previously observed in shallowly buried sediments (e.g. Cashman and Cashman, 2000), so shallow burial of a weakly cemented Moab Tongue sandstone could have driven development of early DBk (Fig. 2.8). Preferential carbonate cementation within DBk suggests some structural control on fluid distribution, possibly due to a transient increase in porosity associated with dilation prior to cataclasis (e.g.

Bésuelle, 2001; Fossen et al., 2007). The cool TD_{47} of these cements are consistent with near-surface temperatures, further supporting the shallow formation of associated deformation bands.

Continuing burial during the early Cretaceous (Fig 2.8) increased temperatures and confining pressures, driving quartz pressure solution and overgrowth cementation (Johansen et al., 2005). Associated porosity reduction and stiffening of the rock triggered a change in deformation mechanism to produce the thinner, more intensely cataclastic DBn. Subsequently, joints developed in DBn, due to increased differential stress from either rapid burial during the mid- to late-Cretaceous or early episodes of faulting, and these became filled with additional cool, non-luminescent cement. The cool $T\Delta_{47}$ suggests the formation and fracturing of DBn also occurred at shallow depths.

As the Moab Tongue sandstone reached peak burial depths of ~2 km and temperatures of ~60 to 80°C (Fig. 2.8; also Garden et al., 2001), the main phase of faulting along the Moab Fault generated new pathways for fluid migration along the fault zone. Local fluid overpressure (Garden et al., 2001) and stresses associated with faulting (Davatzes et al., 2005) produced a joint network cross-cutting the jointed DBn, further enhancing permeability around the fault. Warm, reducing fluids migrated up from below (Garden et al. 2001), mixed with meteoric formation waters and precipitated the warm, luminescent carbonate cements in existing joints (Chan et al., 2000; Eichhubl et al., 2009). The range of $T\Delta_{47}$ for luminescent cements suggests these source fluids continued to precipitate carbonate as the Moab Tongue was exhumed to shallower depths and cooler ambient temperatures

Re-fractured luminescent veins filled with non-luminescent carbonate may signal late motion on the Moab Fault (~5 Ma; Olig et al., 1996; Trudgill, 2011) or stresses related to exhumation. The association of these late cool carbonates with the fault damage zone documents its persistent influence on fluid circulation.

2.6.3 - Deformation bands and fluid flow

Cataclastic deformation bands are typically lower-permeability structures compared to surrounding host rock, and are commonly considered barriers to fluid flow (e.g. Antonellini et al., 1994; Eichhubl et al., 2004; Fossen and Bale, 2007; Balsamo and Storti, 2010; Ballas et al., 2015; Philit et al., 2015). Once jointed, however, deformation bands can become relatively high permeability conduits, focusing fluid migration through the host rock. We found close spatial relationships between cementation temperature and the style of structural deformation at the outcrop scale. Detailed mapping by Eichhubl et al. (2009) demonstrated the localization of carbonate cementation around structures at CHJ. Bergman et al. (2013) identified spatial heterogeneity in the distribution of warmer and cooler carbonate, noting limited spatial distribution of the cool cements. Our new sampling expands the spatial coverage of $T\Delta_{47}$ beyond the linear transect reported by Bergman et al. (2013; Fig. 2.7). Our new data show that warm carbonate is found across much of the outcrop over distances of ~100 m, where it fills jointed DBn and other joints that served as conduits for the associated fluid circulation (Davatzes et al, 2005; Johansen et al, 2005; Eichhubl et al., 2009). The association of non-luminescent cements with thick and thin deformation bands suggests that these structures also influenced the distribution of fluid flow along the Moab Fault. Cool, non-luminescent carbonate occurs within and

around jointed deformation bands, suggesting associated source fluids used the fractures as preferred migration routes through the host rock. Jointed deformation bands are concentrated near the main fault strands, but also extend away from the fault zones (Fig. 2.7). Considering that non-luminescent carbonates formed at near-surface temperatures, it appears that deformation bands had an early influence on fault zone permeability, before substantial burial.

The timing of each style of structural deformation is clearly important to the fluid migration and cementation history of the Moab Fault. It is understood that deformation bands can form at shallow depths (e.g. Cashman and Cashman, 2000; Ballas et al., 2015), and evidence presented in this work suggests that band-parallel fractures may also form at this stage. This is interesting, as it suggests that deformation band faults can *enhance* fault zone permeability from an early stage in their development. Indeed, it appears that deformation bands precondition the rock for fracturing. Cataclasis and porosity reduction locally strengthens the rock, resulting in subsequent jointing of the stiff inclusions in a relatively soft matrix (Tindall and Eckert, 2015). Thus, paradoxically, these low-permeability features may ultimately lead to enhanced permeability of the rock, as recorded at CHJ by the distribution of early carbonate cements.

2.7 - Conclusion

We combine clumped isotope paleothermometry with bulk C and O isotopic data and micro- to outcrop-scale structural observations to investigate carbonate cementation at Courthouse Junction along the Moab Fault. We identify carbonate populations with distinct isotopic compositions, precipitation temperatures and luminescence

characteristics, each associated with different source fluid chemistries and different deformation structures. An early phase of cementation produced non-luminescent carbonate with cool precipitation temperatures in close association with the formation of deformation bands. Source fluids for the cements had isotopic compositions similar to marine waters, possibly containing dissolved limestone. Following peak burial, fractures associated with faulting and exhumation provided conduits for the circulation of meteoric waters, mixed with either an organic-carbon rich fluid or magmatic CO_2, resulting in the formation of luminescent carbonate cements at warm temperatures. The range of temperatures for luminescent carbonate suggests that it continued to form until exhumation reached near surface thermal conditions. Late forming non-luminescent carbonate forms at shallow depths during the last stages of exhumation.

The early episode of non-luminescent cementation reveals the enhancement cataclastic deformation bands can have on fluid circulation. Dilatant deformation bands are understood to enhance structure parallel flow (Antonellini et al., 1994), but cataclastic deformation bands are generally viewed as barriers in a porous sandstone (e.g. Antonellini and Aydin, 1994). Changes in these structures from low porosity bands to jointed conduits appear to happen early in the evolution of the fault zone, making them important controls on fluid flow at CHJ. Considering the complex deformation and cementation history observed at CHJ, it is clear deformation band faults do not have a simple effect on fault zone permeability. Predictive modeling of the permeability of these structures, and related fracturing and jointing, thus requires characterization of the stress and diagenetic histories of the host rock. Here, we demonstrate the power of carbonate clumped isotope thermometry for determining environments for cementation and

constraining fluid sources. Integration of these data with outcrop and petrographic observations, as well as the local burial history, allowed us to build a combined time-temperature history for deformation and diagenesis at Courthouse Junction. These data reveal the persistent influence of deformation structures from the very earliest stages of burial to the final stages of exhumation.

2.8 - Figures

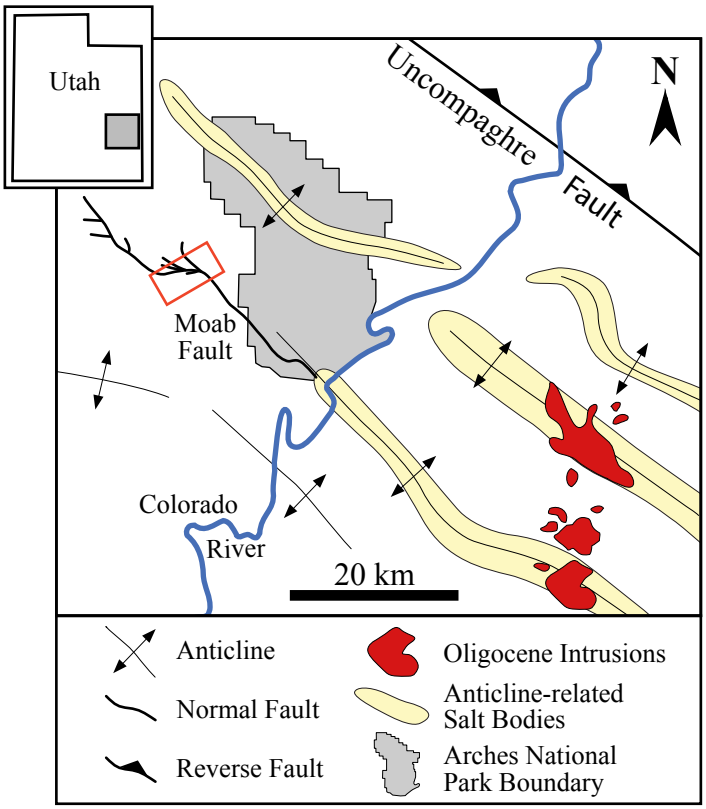

Figure 2.1: Schematic regional map of Paradox Basin showing locations of major geologic features. Red box denotes location of Fig. 2.2. Yellow shapes mark locations of modern salt walls of the Paradox Formation. Red shapes mark locations of Oligocene La Sal laccolith intrusions. Map modified from Doelling (1985).

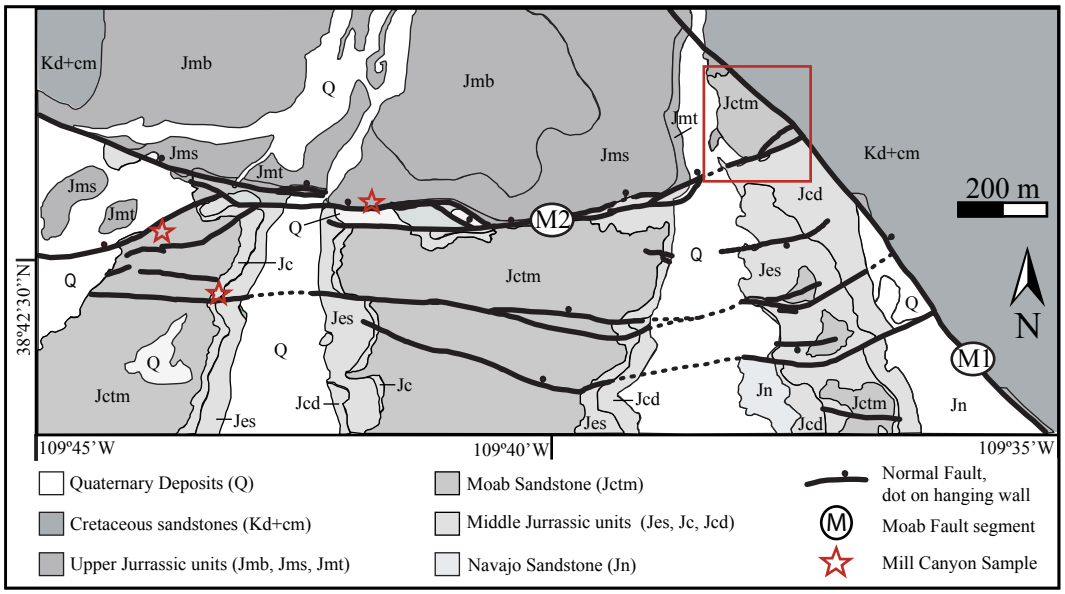

Figure 2.2: Geologic map of Courthouse Junction and Mill Canyon. Red box denotes location of Courthouse Junction sandstone pavement and the majority of discussed samples (Fig 7). Red stars mark locations of samples from Mill Canyon. Map modified from Davatzes et al. (2005).

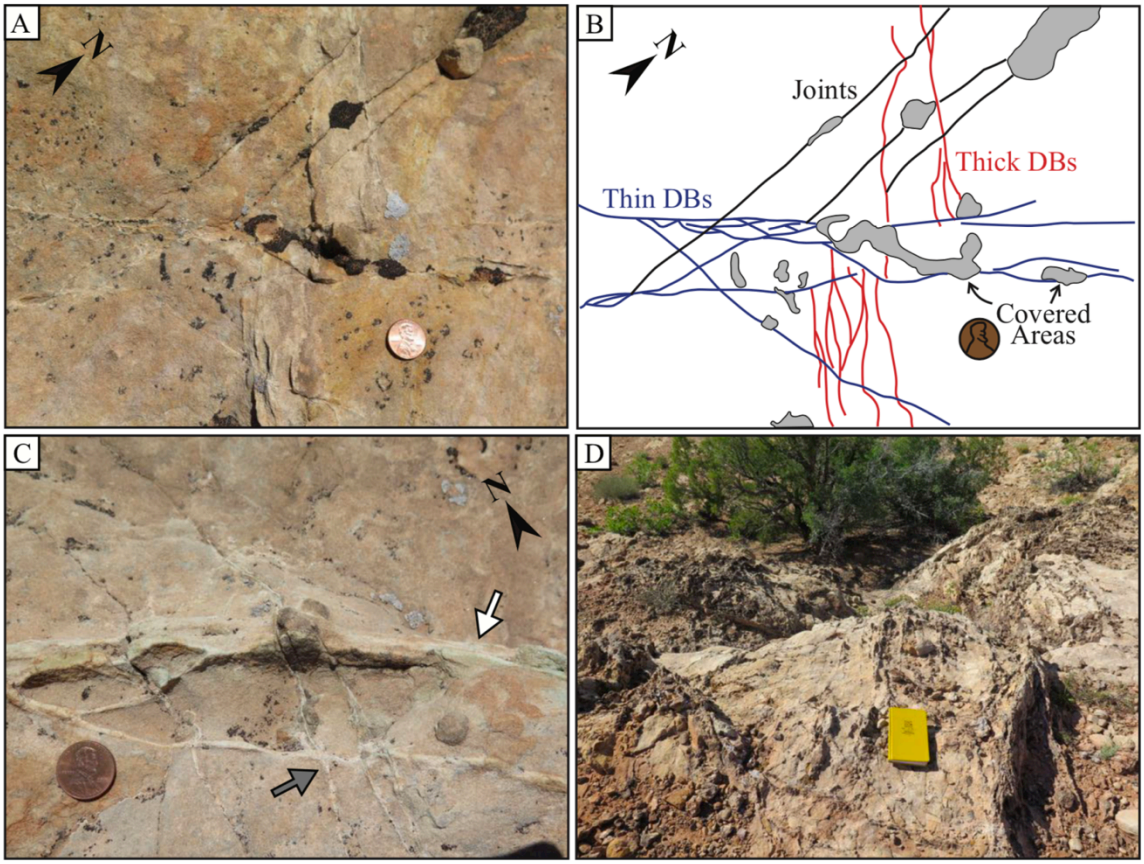

Figure 2.3: Photographs of outcrops at Courthouse Junction. A) Three styles of brittle structures showing relative age. Coin is 19mm in diameter. B) Line drawing of structures shown in A. Early thick deformation bands (red lines) are offset by thin deformation bands (blue lines), and both are cross cut by joints (black lines). C) Thick deformation bands (white arrow) cross cut by later thin deformation bands featuring thin carbonate veins (grey arrow). D) View to north across dense array of veins and concretions close to fault segment M2 (see Fig. 2.7 for location). Field notebook is 24 cm, long dimension.

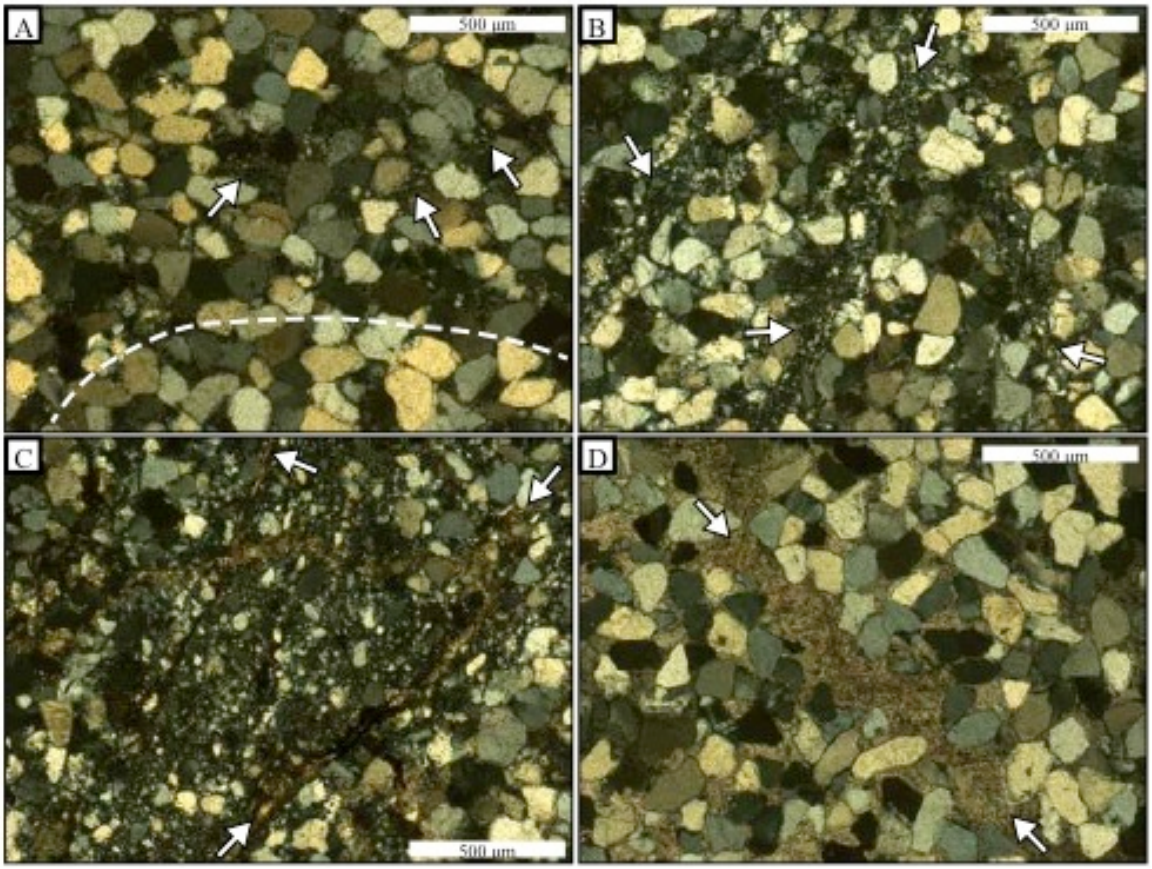

Figure 2.4: Plane light photomicrographs displaying the four main classes of structures at Courthouse Junction. A) Thick deformation band associated with notable quartz pressure solution. White arrows denote locations with localized grain crushing and carbonate cementation. Dashed white line marks approximate edge of deformation band. B) Thin deformation bands (white arrows) in compacted host rock. C) Fractured zone of thin deformation bands filled by carbonate veins (white arrows). D) Vein filling joint not associated with deformation band (arrows).

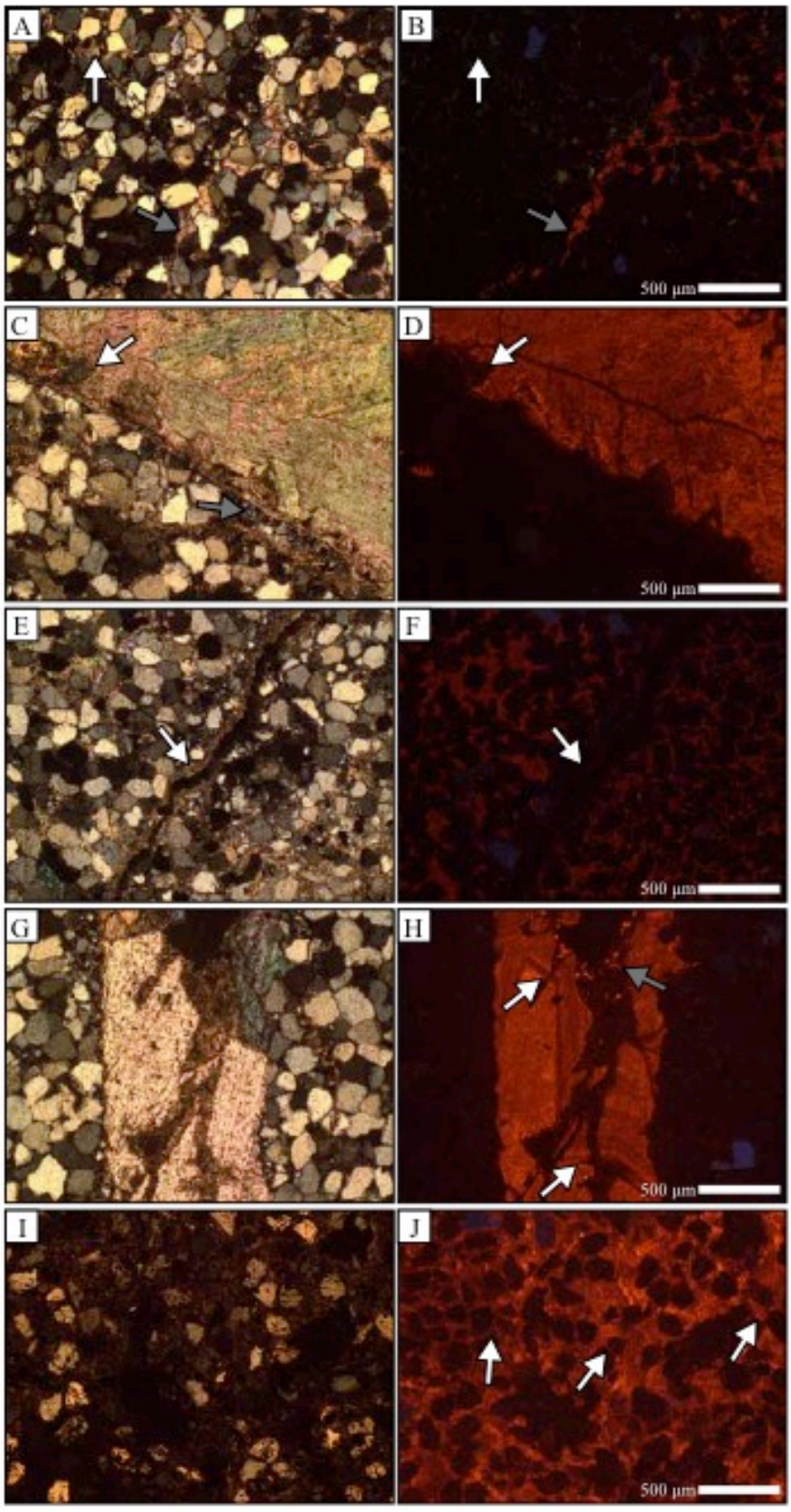
A
B
500 µm
C
D
500 µm
E
F
500 µm
G
H
500 µm
I
J
500 µm

Figure 2.5: Paired plane light and cathodoluminescence (CL) photomicrographs demonstrating styles of carbonate luminescence and relative age. Exposure time for CL images is 1 second. A,B) Early non-luminescent pore-filling cement cross cut by later luminescent vein and pore-filling cement. White arrow points to pocket of non-luminescent cement in both images. Grey arrow marks luminescent vein. C,D) Early non-luminescent cement with later luminescent cement. White arrows point to boundary between luminescent and non-luminescent carbonate in both images. Grey arrow denotes pocket of thin deformation band material that predates both vein fills. E,F) Early luminescent pore-filling cement and later non-luminescent cement forming along margins of fracture. Arrow marks edge of non-luminescent cement in both images. G,H) Fractured luminescent vein filled by later non-luminescent cement. Zonation in CL is crosscut by non-luminescent cement (white arrows). Grey arrow denotes luminescent material entrained in later vein. I,J) Cement-supported quartz grains. Cement runs between previously interlocking grains (white arrows).

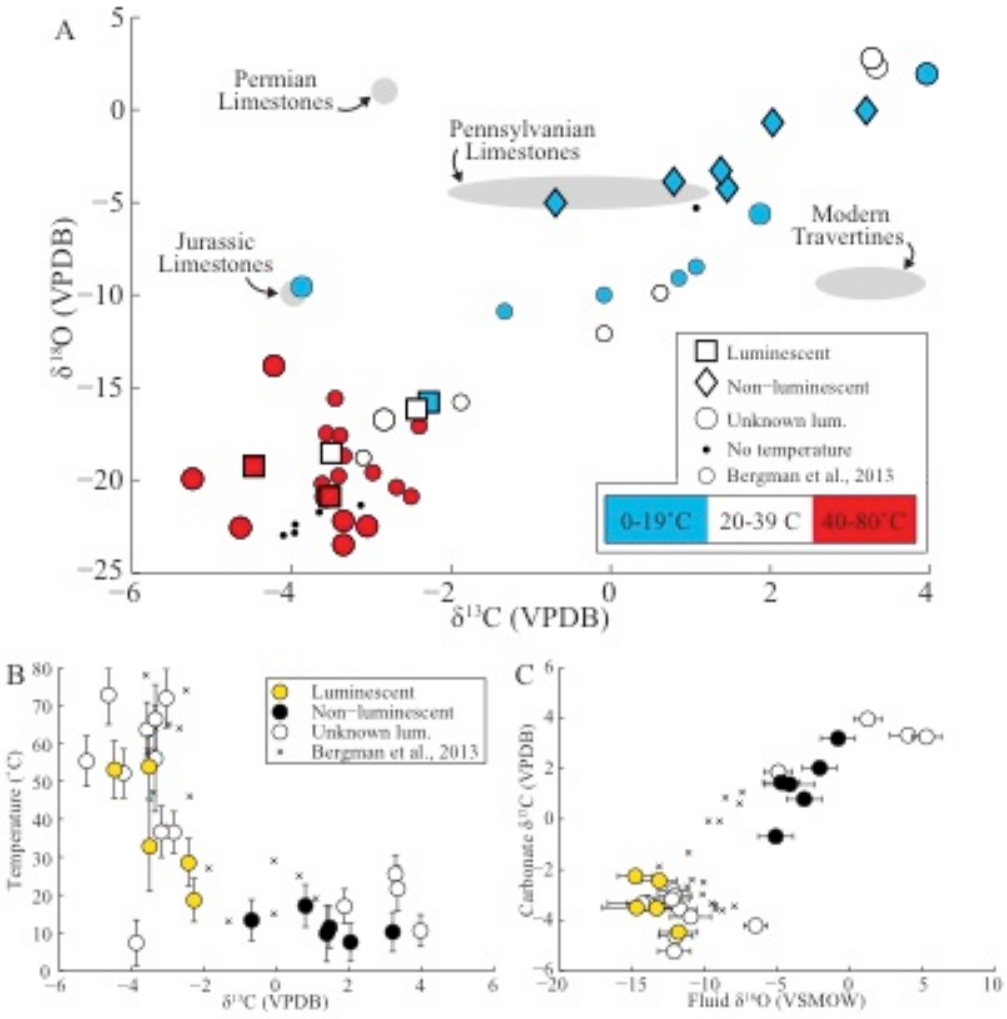

Figure 2.6: Carbonate and source fluid chemistry. A) Carbonate stable isotope compositions colored by relative temperature. Blue to white transition occurs at 20°C, corresponding to the break in temperature between luminescent and non-luminescent cements. White to red transition occurs at 40°C, corresponding to approximate upper boundary for methanogenesis. Squares and diamonds denote samples known to be luminescent and non-luminescent under CL, respectively. Large circles indicate samples with unknown luminescence and small circles denote samples from Bergman et al. (2013), recalculated using the clumped isotope calibration of Kluge et al. (2015). Black dots denote samples without temperature measurements. Shaded fields outline approximate ranges of compositions for possible source fluids (Garden et al., 2001; Shipton et al., 2004). B) Carbonate precipitation temperature and $\delta^{13}C$ composition for samples with known luminescence characteristics (orange and black circles), unknown luminescence (white circles), and data from Bergman et al. (2013; black x's). C)

Carbonate $\delta^{13}C$ and calculated source fluid $\delta^{18}O$ composition. Symbols as in B. Error bars denote standard error of replicate analyses.

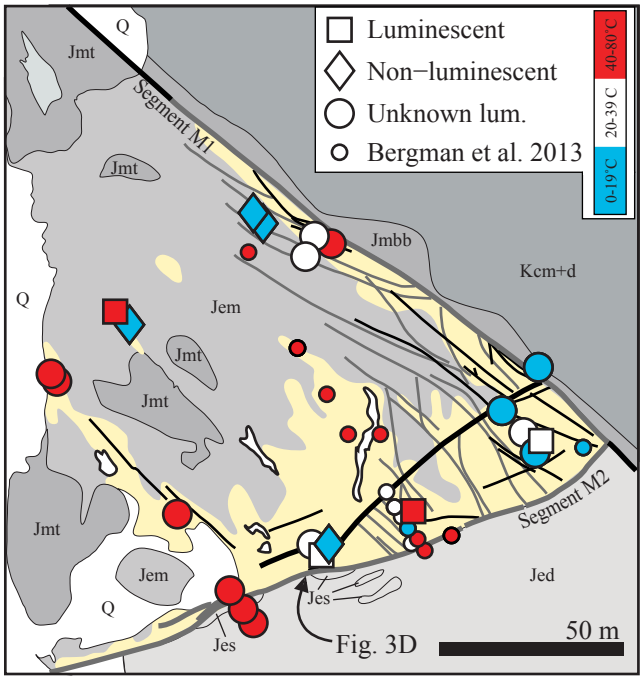

Figure 2.7: Detail map of CHJ outcrop, showing sample locations and distribution of clumped isotope temperatures in relation to major structures. Color scale and symbols as in figure 6A. Thick black and grey lines are major deformation band- and joint-based faults, respectively. Thin black and grey lines are prominent deformation bands and joints, respectively. Yellow shading denotes extent of carbonate cementation after Eichhubl et al. (2009). Structures as mapped by Davatzes et al. (2005), map modified from Eichhubl et al. (2009).

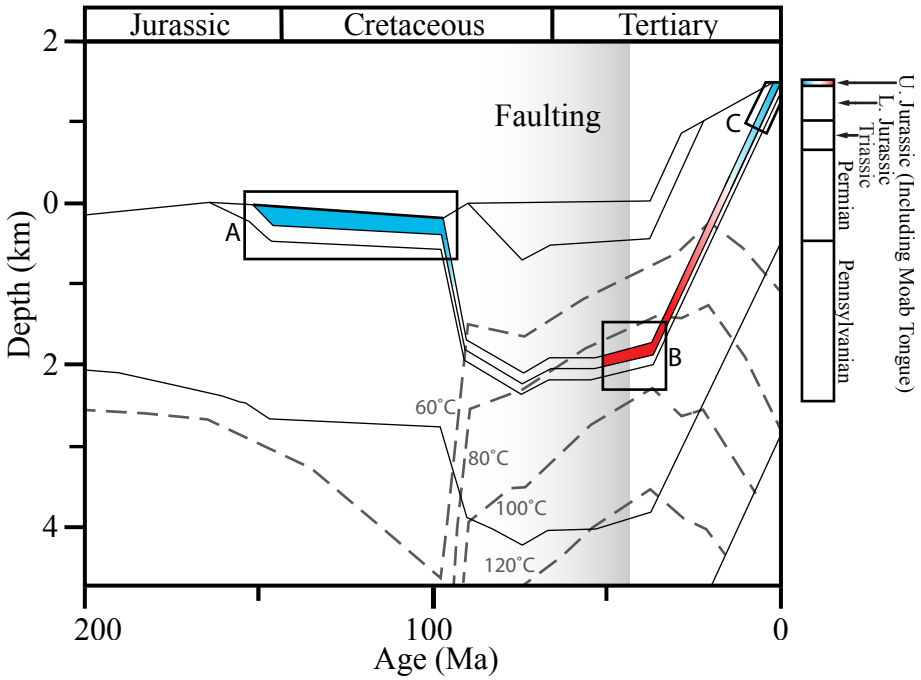

Figure 2.8: Burial curve for the Paradox Basin near the study area (modified from Garden et al., 2001). Colored layer represents the Moab Tongue Sandstone, where color denotes relative temperature during burial and exhumation. Box A show timing of deformation band formation and early non-luminescent cementation. Box B indicates timing and conditions for jointing and the initiation of luminescent cementation. Box C denotes timing and conditions for the re-fracturing of cemented joints and formation of late non-luminescent cements. Grey-shaded box marks possible range of major faulting along the Moab Fault (Pevear et al., 1996; Solum et al., 2005; Trudgill, 2011). The youngest age of fault activity (ca. 43Ma) also corresponds to known episodes of reducing fluid migration (Garden et al., 2001).

2.9 – Tables

Table 2.1 – Sample information and isotopic compositions.

Sample Name	Sample Location[1]		$\delta^{13}C$	$\delta^{18}O$	Δ_{47}			Temperature[5]		$\delta^{18}O$ fluid[6]		
	Latitude	Longitude	(‰, VPDB)	(‰, VPDB)	(‰, ARF)[2]	Stderr (‰)[3]	n[4]	(°C)	Stderr (°C)	(‰, VSMOW)	StdErr (‰)	Luminescent?[7]
CHJ14_JC02	38.71185	-109.73044	-3.1	-21.4	-	-	-	-	-	-	-	-
CHJ14_JC03	38.71176	-109.73006	3.3	2.8	0.62094	0.00429	3	25.5	5.0	5.3	1.0	-
CHJ14_JC04	38.71170	-109.73010	3.3	2.3	0.63298	0.01573	2	21.7	5.9	4.0	1.2	-
CHJ14_JC05	38.71172	-109.73000	-3.6	-20.9	0.52399	0.00932	3	63.7	7.2	-11.7	1.2	-
CHJ14_JC06	38.71135	-109.72953	-3.6	-21.7	-	-	-	-	-	-	-	-
CHJ14_JC07	38.71110	-109.72924	-3.9	-9.6	0.65462	0.00735	2	7.3	6.1	-11.0	1.4	-
CHJ14_JC08	38.71116	-109.72928	-2.8	-16.7	0.58935	0.00896	3	36.5	5.5	-12.2	1.0	-
CHJ14_JC09	38.71121	-109.72938	4.0	1.9	0.67006	0.01058	3	10.6	4.2	1.2	1.0	-
CHJ14_KH01	38.71136	-109.73106	-3.3	-23.5	0.52333	0.00865	2	66.4	9.1	-13.9	1.4	-
CHJ14_KH02	38.71134	-109.73105	-3.1	-22.5	0.50711	0.01528	3	71.9	7.7	-12.1	1.2	-
CHJ14_KH03	38.71113	-109.73080	-4.0	-22.9	-	-	-	-	-	-	-	-
CHJ14_KH04	38.71094	-109.73061	-3.4	-22.2	0.50910	0.00846	2	56.0	14.0	-14.3	2.4	-
CHJ14_KH05	38.71066	-109.73036	-4.2	-13.8	0.54983	0.01114	3	52.1	4.7	-6.5	0.8	-
CHJ14_KH06	38.71072	-109.73036	-3.9	-22.4	-	-	-	-	-	-	-	-
CHJ14_KH07A	38.71074	-109.73031	-4.1	-23.0	-	-	-	-	-	-	-	-
CHJ14_KH08	38.71061	-109.73034	-4.6	-22.6	0.50536	0.00855	3	72.8	7.8	-12.0	1.2	-
CHJ14_KH09	38.71069	-109.73042	-5.2	-19.9	0.54238	0.00886	3	55.3	6.6	-12.1	1.1	-
CHJ14_M2A	38.71134	-109.72923	1.9	-5.6	0.64805	0.00753	3	17.0	4.5	-4.9	1.0	-
CHJ14_M2B	38.71134	-109.72923	1.1	-5.3	-	-	-	-	-	-	-	-
CHJ15-KH02	38.71183	-109.73029	3.2	-0.1	0.67127	0.00394	2	10.2	5.2	-0.8	1.2	N
CHJ15-KH03	38.71180	-109.73026	-0.7	-5.0	0.66042	0.01713	2	13.3	5.4	-5.1	1.2	N
CHJ15-KH07	38.71152	-109.73081	1.5	-4.2	0.66712	0.01926	2	11.4	5.5	-4.7	1.2	N
CHJ15-KH08	38.71154	-109.73081	-3.5	-20.9	0.54579	0.00473	2	53.8	8.1	-13.3	1.4	Y
CHJ15-KH17	38.71113	-109.72922	-2.4	-16.2	0.61203	0.01017	2	28.5	6.3	-13.1	1.3	Y
CHJ15-KH18	38.71093	-109.72971	-4.5	-19.3	0.54756	0.00931	3	53.1	7.6	-11.8	1.3	Y
CHJ15-KH23	38.71083	-109.73007	0.8	-3.9	0.64768	0.01273	2	17.1	5.6	-3.1	1.2	N
CHJ15-KH24	38.71083	-109.73007	-3.2	-16.9	0.58915	0.01114	2	36.6	6.8	-12.3	1.3	-
CHJ15-KH24B	38.71083	-109.73007	-3.5	-18.5	0.56587	0.00794	2	32.9	11.9	-14.7	2.4	Y
MCC15-KH05	38.70916	-109.73871	1.4	-3.3	0.67280	0.00847	1	9.8	7.4	-4.1	1.7	N
MCE15-KH06	38.70742	-109.74565	2.0	-0.7	0.68110	0.00225	2	7.5	5.1	-2.1	1.2	N
MCE15-KH07	38.70743	-109.74580	-2.3	-15.8	0.64288	0.00034	2	18.6	5.7	-14.8	1.2	Y

[1] Sample location recorded with handheld GPS with nominal 5m accuracy.

[2] Δ_{47} values calculated using the standsrd equations (Huntington et al., 2009) without an acid fractionation factor.

[3] Standard errors are from replicate analyses or long term variation of internal standards, whichever is larger.

[4] Number of replicate isotope analyses

[5] Temperatures calculated using equation 5 of Kluge er al. (2015). Errors calculated using propagated Δ_{47} error.

[6] Source fluid $\delta^{18}O$ values calculated following the methods of Kim and O'Niel (1997). Errors propagated from error in calculated temperature.

[7] Observations of CL characteristics were made for a subset of samples prior to isotopic analysis.

Chapter Three

Segment-scale controls and diagenetic conditions associated with protracted post-deformation fluid migration along the Moab Fault, UT

3.0 - Abstract

To better understand the complex relationships between faulting, fluid migration, and diagenesis, we use clumped isotope thermometry and stable isotope geochemistry to characterize the history of carbonate cementation and diagenesis within the Moab Fault Zone in southeast Utah. Here, we present a new dataset characterizing carbonate cements from along the northern Moab Fault system. These data allow us to constrain the timing and conditions for fault-hosted cementation, and explore the spatial relationships between carbonate cement and fault deformation. We identify two generations of cement with distinct stable isotope compositions, precipitation temperatures, and textural characteristics. These include earlier micritic cement with cool, Earth-surface precipitation temperatures (17 to 24°C) and later, post-faulting, crystalline cement with warmer precipitation temperatures (35 to 90°C). Source fluid $\delta^{18}O$ compositions, reconstructed using clumped isotope temperatures, suggest that the earlier cements formed from a predominantly marine source. Source fluids for later crystalline cements have a wide range of $\delta^{18}O$ values. We show that this large range of source-fluid $\delta^{18}O$ values can be attributed to carbonate recrystallization from rock-buffered fluid source during basin exhumation. Cement distributions suggest that interaction between fault segments and secondary structures was the primary control on fault permeability, rather than displacement distribution or lithology of the faulted sequence. We conclude that the Moab Fault hosted protracted fluid migration following the cessation of fault activity,

characterized by the focused migration of rock-buffered diagenetic fluids through zones of structural complexity.

3.1 - Introduction

Fault zones fundamentally alter the permeability structure within sedimentary basins, affecting the fluid migration through the subsurface. Predicting the effects of faulting on fluid migration is of great interest for the recovery and management of energy and groundwater resources. Additionally, the presence of fluids within a fault zone has important implications for fault-related deformation and seismic hazards. Thus, fault zone permeability has direct implications for a number of societally relevant issues, motivating research to constrain and predict the relationships between fault-related deformation, permeability, and fluid flow.

Understanding how faulting controls permeability is complicated by feedbacks between structural deformation, fluid migration and diagenesis. Faulting may increase or decrease permeability relative to the surrounding host rock (e.g. Antonellini et al., 1994; Caine et al., 1996; Evans et al., 1997; Bense et al., 2013), making it difficult to predict the effects of fault zone deformation on fluid migration through sedimentary basins. Indeed, there is increasing recognition that the style of deformation within a fault zone is highly dependent on the presence of fluids and associated cementation and diagenesis (e.g Laubach et al., 2010). Interplay among these processes produces variability in fault zone permeability over space and time. Because fault zone permeability is not a static property, instantaneous evaluations of permeability, measured via permeameters or well-

pressure logs, cannot necessarily be taken to reflect a fault's permeability at other locations or throughout its deformation history (e.g. Bense et al., 2013).

The chemistry of fault-hosted diagenetic minerals and cements provides a valuable window into the cementation history, and associated fluid-migration history, of a fault zone. Fluids can precipitate cements and diagenetically alter the host rock, producing minerals with chemistries that reflect the composition of the source fluids, the host rocks, and the environmental conditions during their formation. If these minerals are preserved, they may be used to interpret the mineral's context and source fluids at the time of formation, which are properties that may vary during the evolution of a fault zone. In this way, cements accumulated throughout deformation can record variability in the fault-fluid system over time. These histories can then be used to understand how source fluid and diagenetic conditions change over the deformation history of a fault zone.

In this study, we analyze samples of carbonate cements and veins from within the Moab Fault in southeast Utah. The Moab Fault has a complex fluid history, evidenced by multiple phases of cementation that correspond to different styles of structural deformation (Davatzes et al., 2005; Johansen et al., 2005; Eichhubl et al., 2009; Bergman et al., 2013; Hodson et al., 2016). Localized studies have constrained the structural deformation and cementation histories at specific locations along the Moab Fault. Using clumped isotope thermometry to determine the precipitation temperature of fault-hosted cements, we address several open questions about the deformation, cementation and diagenetic history of the fault zone, including: Are earlier localized studies representative of fault-scale cementation and deformation? How do variation in displacement, host-rock

lithology, and fault architecture relate to cement composition and distribution? What were temperature and diagenetic conditions associated with cementation? And, how long did fluid circulation and cementation continue after faulting?

To address these questions, we analyzed the textures and stable isotopic compositions of carbonate cements collected from the northern portion of the Moab Fault, from the northern boundary of Arches National Park to the northern fault tip (Fig. 3.1). Using carbonate clumped isotope thermometry (Δ_{47}), bulk isotope ratios of carbon ($\delta^{13}C$) and oxygen ($\delta^{18}O$), and thin section observations, we provide new constraints on cement and source fluid compositions, thermal conditions during mineral growth and their association with deformation structures. Together, these observations and analyses allow us to not only determine the spatial distribution of cements associated with different source fluids and formation temperatures, but also to link the spatial distributions to different deformation structures and processes. We use our findings to outline the evolution of fault-fluid interaction along the Moab Fault, with implications for the timing and duration of cementation. Spatial patterns of cement composition and precipitation temperature allow us to evaluate segment scale variability in fault zone permeability.

3.2 - Regional Geologic History

The Paradox Basin, southeast Utah, comprises a sequence of Pennsylvanian to Cretaceous sedimentary strata deposited in the foreland basin of the Uncompahgre Fault Zone during the uplift of the ancestral and modern Rocky Mountains (Foxford et al., 1996). The basal unit is the Paradox Formation, a ductile salt layer that has been mobile

throughout the deposition and exhumation of the basin (Trudgill, 2011). The growth and collapse of salt walls and diapirs are the primary drivers of deformation within the basin (e.g. Gutiérrez, 2004). Salt-driven deformation of overlying strata produced the characteristic collapsed anticlines and grabens that are observed throughout the basin (Doelling et al., 1988), with perhaps the most extraordinary example at the entrance to Arches National Park.

The Moab Fault Zone is a ~45 km long normal fault system (Fig. 3.1) accommodating the deformation associated with the growth and collapse of the Moab Salt Wall (Gutiérrez, 2004). Maximum displacement is ~1 km along the western margin of the Moab and Spanish Valleys, and decreases northwards to undetectable amounts where the fault intersects with the normal faults of the Ten Mile Graben (Foxford et al., 1996). Sedimentary records indicate that faulting initiated by the late Triassic (Trudgill, 2011; Foxford et al., 1996), although the main phase of deformation is interpreted to have occurred around 63 to 43 m.y.a. based on K/Ar and $^{40}Ar/^{39}Ar$ dating of fault gouge from two locations along the fault zone (Pevear et al., 1997; Solum et al., 2005). This time period coincides with peak burial within the basin, as well as the bleaching of hematite cements in the host rock surrounding the fault zone (Garden et al., 2001).

The exceptional exposure of the Moab Fault within ancient reservoir rocks has made the structure an excellent natural laboratory for investigating the relationships between faulting and fluids in the shallow crust. A number of studies have focused on the Courthouse Junction locality (Fig. 3.1), a particularly well-exposed fault-segment intersection. These studies have characterized the structural and diagenetic histories of the intersection zone, outlining a progression of deformation styles (Davatzes et al., 2005;

Johansen et al., 2005) and fluid-driven cementation and diagenesis (Chan et al., 2000; Eichhubl et al., 2009; Bergman et al., 2013; Hodson et al., 2016). Based on these studies, Courthouse Junction appears to record at least two phases of deformation and cementation (Fig. 3.2; Hodson et al., 2016): An early phase is characterized by deformation band structures and cements formed from marine fluids at cool temperatures (C1). These likely reflect incipient faulting in the early Cretaceous prior to significant burial. Later deformation around the time of peak burial was characterized by fracturing within the fault damage zone, which accommodated the circulation of warm fluids and the formation of crystalline veins within the fractures (C2).

The style of segmentation along the fault zone includes both linear and curved segments, interacting across relay zones in some instances and abutting at high angles in others (Fig. 3.1). Differences in fault geometry, along with displacement gradients and varying permeability of units juxtaposed within the fault zone may influence the deformation and diagenetic history along the fault system. Guided by fault zone geometry and the location of two prominent fault segment intersection zones, Courthouse Junction (CHJ) and Water Tank Junction (WTJ), we subdivide the NMF into three primary fault segments (Fig. 3.1). Segment A is the portion of the fault zone between the northern boundary of Arches National Park and CHJ. Segment B is the portion of the fault zone between CHJ and WTJ. Segment C is the portion of the fault zone north of WTJ. Each of the primary segments contains multiple smaller segments and subsidiary structures (e.g. Foxford et al., 1996; Fossen et al., 2005; Davatzes et al., 2005), but the primary segment boundaries highlight major changes in the orientation of the fault zone. Segments A and C are relatively linear portions of the fault with NNW-SSE trending fault traces. Segment

B has a more E-W trending trace and comprises a series of curved subsidiary fault segments.

Here, we characterize the first-order patterns of carbonate geochemistry along the Northern Moab Fault (NMF). Using the framework developed at Courthouse Junction, we investigate broader scale patterns in cementation conditions and use spatial patterns of cement composition and precipitation temperature to interpret segment-scale controls on the distribution of fault zone permeability.

3.3 - Methods

3.3.1 - Sample Collection, Characterization, and Preparation.

We analyzed 60 samples collected within the NMF, from the northern boundary of Arches National Park to the northern-most mapped extent of the fault zone, including the tips and central portions of major fault segments. All accessible portions of the fault zone were visited over the course of three field seasons between 2014 and 2016. Outcrops and sampling locations were characterized in the field, including descriptions of cement features and their structural context. Carbonate cemented fault rock (Fig. 3.2) was sampled primarily from the footwall damage zone or the fault core in sandstone units including: the Moab Tongue, Salt Wash Member of the Morrison Formation, Navajo Sandstone, Kayenta Sandstone, and Wingate Sandstone. When evidence for multiple styles or episodes of cementation was observed, a representative sample of each cement feature was collected along with any accompanying structural feature.

All samples were analyzed in thin section using standard petrographic and cathodoluminescence (CL) microscopy. These observations, including characterization of

carbonate cement and deformation structures, guided and provided context for subsequent geochemical analyses. Representative portions of each sample were extracted from the hand sample; either by removal of carbonate crystals from crystalline veins, physical separation of pieces of cemented sandstone, or grinding with a tungsten-carbide-tipped laboratory drill. Care was taken to micro-sample single generations of cement when possible, but the relatively large sample mass required for analysis (6 to 8 mg per replicate analysis) precluded this in some cases. Micro-sampled material was then crushed and homogenized by mortar and pestle prior to isotope analysis.

3.3.2 – Carbon, Oxygen and Clumped Isotope Analyses

All stable isotope analyses were performed at IsoLab at the University of Washington. Bulk carbon and oxygen isotope analyses ($\delta^{13}C$ and $\delta^{18}O$) were made following the methods of Tobin et al. (2011) using a Kiel III Device connected to a Thermo Scientific Delta Plus isotope ratio mass spectrometer. For clumped isotope analysis (Δ_{47}), carbonate samples were digested in phosphoric acid at 90°C, and the evolved CO_2 was purified following methods described in Burgener et al. (2016) and Hodson et al. (2016). Purified gasses were then stored in flame sealed borosilicate glass tubes until analysis. An external (ETH1, ETH2, or ETH3) or internal laboratory standard was purified between every four to five samples. Clumped isotope analyses were performed on a Thermo MAT 253 isotope ratio mass spectrometer configured to measure *m/z* 44-49 (inclusive). To convert measured isotope ratios to the Vienna Pee Dee Belemite (VPDB) and Vienna Standard Marine Ocean Water (VSMOW) reference scales, internal laboratory standards calibrated against NBS-18 and NBS-19 (IAEA,

Vienna, Austria), and LSVEC (NIST, Gaithersburg, MD, USA) international standards were analyzed along with sample carbonates.

Values for Δ_{47} were calculated using the methods of Huntington et al. (2009) and the pressure baseline correction of He et al. (2012), and reported in the absolute reference frame (Dennis et al., 2011). Δ_{47} values are reported with no acid fractionation factor (i.e., in the 90°C acid reference frame). Values for $\delta^{13}C$ and $\delta^{18}O$ were calculated using the updated ^{17}O correction values determined by Brand et al. (2010), following the methods of Daëron et al. (2016) and Schauer et al. (2016). Because calcium carbonate speciation is not believed to have a significant effect on Δ_{47} values (Defliese and Lohmann, 2015), mineralogy was assumed to be calcite in all samples. Values of Δ_{47} were converted to temperatures ($T(\Delta_{47})$) using the calibration of Kelson et al. (2017), which was generated in the same laboratory as our analyses using the ^{17}O correction factors of Brand et al. (2010). To ensure consistency between datasets discussed in this manuscript, we recalculated the clumped isotope results of Hodson et al. (2016) using the scripts of Schauer et al. (2017), which include the updated Brand et al. (2010) ^{17}O correction and Kelson et al. (2017) temperature calibration.

3.4 – Results

3.4.1 – Thin Section Observations:

Thin sections observations were used to characterize the deformation mechanisms and cementation patterns in our samples (Fig. 3.3). The sandstones are generally mature, very well sorted and quartz-rich. Calcite was the most common cement observed within the fault zone, but quartz and hematite were also present in varying amounts. Sand grains

typically show signs of compaction and pressure solution along with quartz overgrowth cements. Detailed petrographic descriptions of rock units and cement mineralogy can be found in previous structural and diagenetic studies from the Moab Fault Zone (e.g. Chan et al., 2000; Garden et al., 2001; Eichhubl et al., 2009b; Hodson et al., 2016).

Our new micro-structural observations follow those previously reported for the Moab Fault (Davatzes et al., 2005; Johansen et al., 2005). Fault-zone deformation structures include: 1) early-forming deformation bands characterized by wide tabular zones of reduced porosity with limited cataclasis (Fig. 3.3a and 3.3b), similar to the "shear enhanced compaction bands" described by Eichhubl et al. (2010); 2) later-forming deformation bands characterized by thin zones of intense cataclasis surrounded by undamaged host rock (Fig. 3.3c); and 3) opening-mode fractures that crosscut both sets of deformation bands, typically filled by crystalline carbonate veins (Fig. 3.3d).

Samples contained evidence for multiple stages of cementation, occurring as pore cements and fracture-filling veins (Figs. 3.3 and 3.4). Pore cement textures include both micritic and crystalline carbonate, while veins were predominantly crystalline in texture. Crystalline pore cements commonly display poikilotopic textures surrounding quartz sand grains. The larger crystalline veins, up to ~2 cm in width, are composed of blocky calcite crystals with abundant twinning (Fig. 3.4). Thin veins (<1 mm across) were observed to contain both micritic and crystalline cement, with micritic and finely crystalline veins filling fractures along the margin of deformation bands or following the margins of earlier blocky crystalline veins.

The large, crystalline veins were observed to have signs of diagenetic alteration. Zones of finely crystalline carbonate are present within the veins, featuring irregular

margins with the larger blocky crystals (Fig. 3.4). These finely crystalline zones occur as irregularly shaped patches (Figs. 3.4a and 3.4b) and as bands that overprint and cut the earlier blocky cement (Figs. 3.4c and 3.4d). In some cases, twinning patterns within the large blocky crystals can be seen to continue on the opposite side of the fine-grained zones (Fig. 3.4a). Small remnants of twinned calcite can also be found within the patches of fine-grained cement, with twin plane orientations parallel to nearby blocky crystals. These observations suggest that the blocky, twinned carbonate crystals experienced later alteration by partial dissolution followed by precipitation of a more finely grained calcite cement. The later cement is commonly associated with opaque to blood red coloration in plane light (Fig. 3.4b) suggestive of iron oxides (hematite) being intermixed with the carbonate.

Cathodoluminescence reveals additional chemical zonation in our samples, and helps further characterize cementation and alteration histories. Micritic and fine-grained cements were observed to be both luminescent and non-luminescent in different samples. Micritic carbonate cements associated with the deformation bands, as both pore cement and thin veins, were consistently non-luminescent. Fine-grained cement associated with the irregular alteration zones displayed a similar range of luminescence styles as the primary, coarsely crystalline vein fills that they overprint. All coarsely-crystalline veins, poikilotopic pore cement, and alteration-related finely-crystalline cement displayed a bright orange to deep red luminescence (Fig. 3.4), with luminescence intensities ranging from bright to dim to unobservable in some cases. Luminescence intensities can be highly variable within a single vein. Differences between the luminescence intensity of the primary crystalline vein fills and the zones of alteration further support a later fluid

alteration event associated with the fine-grained cement, indicating a difference in source fluid chemistry or cementation conditions (e.g. Götze, 2012). Within some of the blocky carbonate veins, zones of bright luminescence are localized along crystal boundaries, fractures and twin planes (Figs. 3.4g and 3.4f), suggestive of fluid infiltration along micro-fractures and planes of weakness within the vein.

3.4.2 - Isotopic Results

Carbonate cements from the Northern Moab Fault (NMF) have $\delta^{13}C$ values ranging from -10.4 to 3.6 ‰ VPDB and $\delta^{18}O$ values ranging from -22.4 to 0.4 ‰ VPDB (see supplemental table). Our new measurements display a clear correlation between carbonate $\delta^{13}C$ and $\delta^{18}O$ values (Fig. 3.5a), similar to values previously reported from elsewhere along the fault zone (Chan et al., 2000; Hodson et al., 2016; Bergman et al., 2013; Eichhubl et al., 2009; Garden et al., 2001). The spread of oxygen and carbon isotope compositions was shown by Hodson et al. (2016) to represent two distinct cementation events: earlier, micritic cements (C1) have $\delta^{13}C$ and $\delta^{18}O$ values of -1 to 3 ‰ and -5 to 0 ‰, respectively. Later, more crystalline cements (C2) have lower values of both $\delta^{13}C$ and $\delta^{18}O$: -5 to -2 ‰ and -21 to -16 ‰, respectively. Bulk isotope compositions of our new samples follow a similar pattern, with end-member carbonate cements displaying similar textural characteristics to those from CHJ. Indeed, some samples that were found to contain a mixture of both cements in thin section have bulk isotope compositions that fall between the two end members, indicating a mixture of the two cement compositions in the analyzed sample. Two samples from along the NMF containing only C1 cements have $\delta^{13}C$ values of -0.5 and -0.1 ‰ (VPDB) and $\delta^{18}O$

values of -8.0 and -6.7 ‰ (VPDB), close to the range of similar textured cements from CHJ. The new $\delta^{18}O$ measurements from C2 cements from along the NMF have a wider range of values (-22.4 to -10.9 ‰ VPDB) than was found at the localized CHJ study. Carbon isotope compositions for C2 cements from along the NMF were between -8.3 and -3.7 ‰ (VPDB), generally consistent with values reported at CHJ.

Clumped isotope measurements from the new NMF samples produce Δ_{47} values between 0.455 and 0.690 ‰ (Fig. 3.5), corresponding to temperatures of 2 to 90°C using the calibration of Kelson et al. (2017; Tables 3.1 and supplemental material). Associated standard errors range from 0.009 to 0.03 ‰ (mean: 0.018 ‰), equivalent to 3 to 15°C (mean: 7°C). Higher $T(\Delta_{47})$ (~35 to 90°C) are associated with C2 cements, and cooler $T(\Delta_{47})$ (~17 to 24°C) are associated with C1 cements (Fig. 3.6). A similar relationship between cement generation and $T(\Delta_{47})$ was identified by Hodson et al. (2016), and is preserved in the CHJ values recalculated for this study: C1 cements have $T(\Delta_{47})$ between 11 and 19°C, and C2 cements have $T(\Delta_{47})$ between 19 and 52°C (supplemental material). Fluid inclusion analyses on C2 veins from CHJ have homogenization temperatures of 100° to 125°C (Eichhubl et al., 2009), the lower end of which is within error of our warmest clumped isotope temperature from the NMF.

Using measured carbonate $\delta^{18}O$ and $T(\Delta_{47})$ values, we apply the temperature-dependent O-isotope fractionation relationship of Kim and O'Neil (1997) to calculate the apparent source-fluid $\delta^{18}O$ composition for our samples (Table 3.1; Fig. 3.6). Reconstructed $\delta^{18}O_{fluid}$ values from the NMF range from -16.6 to -1.5 ‰ (VSMOW), with associated standard errors between 0.5 and 2.4 ‰ (mean: 1.3 ‰). Calculated $\delta^{18}O_{fluid}$ values for C1 cements are -7.2 +/- 1.3 ‰ and -4.5 +/- 1.2 ‰ (VSMOW), similar

to recalculated values from CHJ (-5.6 to -0.2 ‰ VSMOW). C2 cements from the NMF have $\delta^{18}O_{fluid}$ values between -16 and -1 ‰ (VSMOW), extending to much higher values than were found for similar cements at CHJ (-14.9 to -12.2 ‰).

3.4.2 – Distribution of Cement Compositions

Both the C1 and C2 cements were found along the length of the NMF, including a large number of samples (n=15) containing both generations of cement. Only two samples were found to contain only C1 cement (NMF15-KH01 and NMF15-KH09), and both were collected from within a few hundred meters of each other along Segment B, which is the segment between CHJ and WTJ. Samples containing only later C2 cement were more abundant and were distributed along the length of the fault.

Late C2 cements do not display any clear systematic variation in $\delta^{18}O$, $\delta^{13}C$, $T(\Delta_{47})$, or $\delta^{18}O_{fluid}$ values along strike (Fig. 3.7). Sample NMF15-KH04, located approximately 2 km south of WTJ, has relatively low $\delta^{13}C$ and $T(\Delta_{47})$ compared to the other C2 samples, but similar $\delta^{18}O$ and $\delta^{18}O_{fluid}$ values. North of WTJ, samples containing mixed cements feature $\delta^{18}O$ and $\delta^{13}C$ values that increase northward, suggesting the isotopically heavier C1 cements become relatively more prevalent towards the northern terminus of the fault zone. Segment B hosts the only samples with only C1 cements, and the highest values of $\delta^{18}O$ and $\delta^{13}C$.

3.5 – Discussion

Our results place new constraints on the cementation history of the Moab Fault and the relationships between cementation and structural deformation. Here, we show

that our new data from the NMF record carbonate crystallization temperatures and can be interpreted in the context of the framework developed at the CHJ locality, extending past interpretations of the timing of cementation and the composition of associated source fluids to the greater Moab Fault system. Relationships between precipitation temperature and source fluid compositions reveal that C2 cementation was long-lived, occurring under rock-buffered conditions. We use spatial patterns of cement composition and precipitation temperature to interpret segment-scale structural controls on the distribution of fault zone permeability. Together, these findings allow us to present an integrated history of faulting, fluid flow, and cementation for the Moab Fault. The implications of this variability in terms of cementation temperature, fluid source, and alteration are discussed below.

3.5.1 – Potential for Diffusive Reordering of Clumped Isotope Values

In the absence of diffusive reordering, clumped isotope thermometry will record the ambient temperature during mineral growth or re-crystallization, which can be combined with $\delta^{18}O$ values of the carbonate to calculate the oxygen isotopic composition of the precipitating fluid. Considering the known burial history for the Paradox Basin, we can assess the potential effects of thermal re-equilibration through diffusive reordering on our measured clumped isotope compositions. At higher temperatures, carbonate molecules within the mineral may undergo relatively rapid isotopic exchange, allowing clumped isotope compositions to be altered through solid-state reordering (Stolper and Eiler, 2015; Passey and Henkes, 2012; Henkes et al., 2014; Lloyd et al., 2017). The effect of reheating on Δ_{47} values is a function of the time-temperature (t-T) history of the rock,

and becomes important only if temperatures are high enough for a long enough period of time (Henkes et al., 2014; Stolper and Eiler, 2015; see also review by Huntington and Lechler, 2015).

Application of the reordering model of Henkes et al. (2014) suggests that the t-T history of the NMF does not reach high enough temperatures for long enough time to significantly alter Δ_{47} values (Fig. 3.A1). Based on new estimates of the timing of basin exhumation (Murray et al., 2016), the maximum burial duration for the earliest cements in this study (C1) is ~100 m.y. Holding a carbonate with an initial, surficial T(Δ_{47}) of 20°C at the peak burial temperature of 90°C (Garden et al., 2001) for 100 m.y. is not predicted to change the measured T(Δ_{47}) by more than 1°C (Fig. 3.A1). Even if we choose a peak burial temperature that is 30°C hotter than the previously reported peak burial temperature (120°C), the effect of reordering on T(Δ_{47}) is still less than 10°C. This indicates that C1 carbonates were not buried long enough for Δ_{47} values to significantly re-equilibrate. Furthermore, even after burial at temperatures ~30 °C higher than the maximum reconstructed temperature, thermally driven reordering cannot explain the observed range of T(Δ_{47}) for C2 and undifferentiated cements. This supports the conlcusion that measured T(Δ_{47}) reflect the mineral formation temperature, either during primary crystal growth or recrystallization during secondary alteration, and we use these temperatures to interpret the timing, fluid to rock ratio, and controls on distribution for C2 cementation.

3.5.2 – Timing of Cementation and Source Fluid $\delta^{18}O$ Compositions Along the Northern Moab Fault

Our geochemical and petrographic observations, interpreted in the context of new constraints on the Paradox Basin thermal history, allow us to examine the timing of carbonate cementation and fluid flow along the NMF. Along the Moab Fault, there is correspondence between temperatures expected from modeled burial depths and the range of measured clumped isotope ($T(\Delta_{47})$) and fluid inclusion temperatures. As discussed by Hodson et al. (2016), the precipitation temperatures for C1 and C2 cements span the range of temperatures associated with the burial and exhumation histories of the sampled stratigraphy. The C1 cements record cementation before substantial burial. Later C2 cements are found filling fractures associated with the main episode of faulting, which occurred during peak burial conditions with ambient temperatures around 90°C (Garden et al., 2001). The range of temperatures associated with C2 cements is compatible with cementation from a thermally equilibrated (or close to equilibrated) fluid, beginning shortly after faulting and continuing during exhumation of the Paradox Basin. We note that the burial history of Garden et al. (2001) assumes relatively constant exhumation of the basin following the end of faulting ca. 45 m.y.a. However, recent work has shown that the central Colorado Plateau and Paradox Basin did not experience major exhumation until after 3 m.y.a. (Murray et al., 2016). This suggests that the observed exhumation-related cementation occurred during the late Cenozoic, and that the units sampled in this study spent much longer at peak burial temperatures than was previously recognized.

Calculated $\delta^{18}O_{fluid}$ values (Fig. 3.6), when interpreted with the carbonate $\delta^{13}C$ values (Fig. 3.5a), suggest a marine fluid source for the C1 carbonate ($\delta^{18}O_{fluid}$ > -10‰ VSMOW and $\delta^{13}C$ ~ 0 ‰ VPDB). During the Cretaceous, an inland seaway inundated the Paradox Basin and the sampled strata were shallowly buried within a few hundred meters of the surface (Garden et al., 2001; Trudgill, 2011). The presence of marine waters and relatively low ambient temperatures is consistent with these reconstructed source-fluid compositions and cementation temperatures for the C1 cements. This suggests that these cements formed from marine fluids circulating through shallow aquifers and flowing along the precursory NMF during the early Cretaceous, prior to or during the early stages of late-Cretaceous rapid burial (Garden et al., 2001; Hodson et al., 2016).

Calculated $\delta^{18}O_{fluid}$ values for C2 carbonates along the NMF have a range of ~15 ‰, spanning values consistent with both marine and meteoric waters. At CHJ segment intersection, $\delta^{18}O_{fluid}$ compositions for C2 cements are limited to values more suggestive of a meteoric fluid source (Hodson et al., 2016). Carbonate $\delta^{13}C$ values for the C2 cements are lower than expected for a marine carbon source (~ 0 ‰ VPDB), but much higher than expected for an organic carbon source (~ -30 ‰ VPDB). At CHJ, Eichhubl et al. (2009) reported similar $\delta^{13}C$ values that were interpreted to reflect reducing aqueous fluids that had interacted with hydrocarbons or magmatic CO_2, either prior to or concurrent with cementation. The similarity in $\delta^{13}C$ values from CHJ and the greater NMF suggest the same carbon source influenced $\delta^{13}C$ compositions along the entire fault zone.

3.5.3 – Diagenetic Conditions During Post-Faulting Cementation

Petrographic and cathodoluminescence observations from these samples show that the C2 veins were altered during a later diagenetic event, resulting in the partial dissolution of earlier cement followed by precipitation of finely crystalline carbonate (Fig. 3.4). We demonstrate that a simple model of closed system, rock-buffered diagenesis can explain the broad patterns of carbonate $\delta^{18}O$ and $\delta^{13}C$, $\delta^{18}O_{fluid}$, and $T(\Delta_{47})$ values observed for C2 cements.

In an open system with high fluid-to-rock ratios, diagenetic recrystallization can produce secondary carbonate in isotopic equilibrium with the diagenetic fluids and temperature during alteration. If secondary carbonate precipitation occurred from a source fluid with a constant $\delta^{18}O_{fluid}$ composition under a range of temperatures, such as during exhumation-related cooling, we would expect variability in the carbonate $\delta^{18}O$ values to reflect temperature-dependent fractionation. This is opposite the pattern we observe from the NMF, where calculated $\delta^{18}O_{fluid}$ values are variable with temperature but carbonate $\delta^{18}O$ values are not.

In a closed system with low fluid-rock ratios, diagenesis becomes rock buffered and the carbonate bulk isotopic composition remains unchanged during alteration (Banner and Hanson, 1990). However, if recrystallization occurs at a different temperature, the Δ_{47} value of the carbonate will change to reflect the temperature at which diagenetic recrystallization occurred (Huntington et al., 2011). In this case, $T(\Delta_{47})$ will reflect the temperature of recrystallization, while the $\delta^{18}O$ and $\delta^{13}C$ of the carbonate cement will remain unchanged relative to the primary mineral. Diagenetic fluids will display variable $\delta^{18}O_{fluid}$ values to accommodate varying temperature-dependent

fractionation from an unchanging carbonate $\delta^{18}O$ composition, similar to the pattern observed from the NMF.

We used the model of Banner and Hanson (1990) to evaluate whether our $T(\Delta_{47})$ and $\delta^{18}O_{fluid}$ values are compatible with expected trends for diagenesis under open and closed systems and different fluid-to-rock ratios. Using the mean C2 carbonate and fluid $\delta^{18}O$ values of 13 ‰ and -10 ‰ (VSMOW), respectively, as initial rock and fluid isotopic compositions, we modeled the equilibrium $\delta^{18}O$ values of carbonate and fluids during cooling from 100 °C to 0 °C under open and closed system conditions and fluid-to-rock ratios of 0.01 to 0.9 (Fig. 3.8). The observed $T(\Delta_{47})$, carbonate $\delta^{18}O$, and $\delta^{18}O_{fluid}$ values for C2 cement are not consistent with an open system or high fluid-to-rock ratios under closed system conditions. The closed-system model with low fluid-to-rock conditions, however, does succeed in reproducing the observed values (Fig. 3.8a). This indicates that the ranges of carbonate $\delta^{18}O$, $\delta^{18}O_{fluid}$, and $T(\Delta_{47})$ may be the result of rock-buffered formation of C2 veins over the range of temperatures experienced during exhumation from peak burial depths to the surface.

Petrographic and cathodoluminescence observations from these samples showed that the C2 veins were altered during a later diagenetic event, resulting in the partial dissolution of earlier cement followed by precipitation of finely crystalline carbonate (Fig. 3.4). This partial recrystallization may contribute to the observed values of carbonate $\delta^{18}O$, $\delta^{18}O_{fluid}$, and $T(\Delta_{47})$ (Figs. 3.5 and 3.6). Together with our modeling results, we take these observations to indicate that the C2 cements reflect closed-system diagenesis under rock-buffered conditions at a range of temperatures during exhumation

of the fault zone. This finding implies that fluid migration associated with the formation of C2 cements was long lived, continuing throughout exhumation of the basin.

Because recrystallization was incomplete, these samples contain varying mixtures of primary and secondary C2 cement. Samples of these cements collected for clumped isotope analysis can also be assumed to contain a mixture of the two phases, which have distinct $T(\Delta_{47})$ reflecting the temperature difference between initial cementation and alteration during exhumation, but similar carbonate $\delta^{18}O$ values. Mixing of carbonate with distinct Δ_{47}, $\delta^{18}O$, and $\delta^{13}C$ compositions can produce measured Δ_{47} values that follow non-linear trends, even returning $T(\Delta_{47})$ that are outside of the range bounded by the mixing carbonates (Defliese and Lohmann, 2015). However, in the case of mixing between carbonates with similar $\delta^{18}O$ and $\delta^{13}C$ values, Δ_{47} measurements mix linearly, and measured Δ_{47} values will be proportional to the relative contributions of each end-member carbonate. As discussed above, we see little to no systematic variability in $\delta^{18}O$ and $\delta^{13}C$ values for the C2 cements from the NMF, suggesting that the primary and secondary carbonates have similar isotopic compositions. This indicates that our range of measured $T(\Delta_{47})$ values can be taken to reflect the combined effects of: 1) the absolute temperatures of primary and secondary C2 cement; and 2) the relative proportions of primary and secondary C2 cement in the sample. While maximum temperatures may be constrained using the burial history curve, we do not have independent constraints on the temperature (or range of temperatures) during diagenesis or the relative proportions of primary and secondary C2 carbonate in each sample. Thin section observations suggest that altered material comprises less than ~10% of vein filling cements (Fig. 3.3), although the proportion in samples extracted for isotopic analysis could be different depending on

the exact location sampled within a given vein. The relatively minor amounts of recrystallized material may contribute to the observed scatter in Figure 3.5, but measured $T(\Delta_{47})$ are likely close to the primary mineralization temperatures for C2 veins.

Despite the uncertainties in relative proportion and precipitation temperature of secondary cements, our results place new constraints on the temperature and conditions associated with the formation and alteration of the C2 cements. The observed patterns of carbonate and $\delta^{18}O_{fluid}$ are compatible with the initial formation of primary C2 cements at peak burial temperatures followed by continued vein growth and partial recrystallization at lower temperatures during exhumation, from a rock-buffered fluid source. Cementation must have continued until ambient temperatures fell below ~35 °C to account for the lowest measured $T(\Delta_{47})$.

3.5.4 - Spatial Patterns of Cement and Source Fluid Composition Along the NMF

The style and intensity of structural deformation along a fault system can be variable in both space and time due to factors such as fault growth, lithologic variability, and diagenetic alteration. Because these same properties and processes are important controls on fault zone permeability, spatial and temporal variability in permeability is expected as well. Our new data from the NMF provide a record of cementation associated with fault-fluid interaction, which we use to explore permeability variations in the context of the well-characterized displacement distributions and detailed lithologic and structural mapping available for the fault system. In the following section, we use these spatial distributions to evaluate three predictive models of fault zone permeability: 1) displacement-controlled development of the fault damage zone; 2) shale-gouge ratio

estimates of fault core composition; and 3) localization of conduits around fault segment intersections and zones of structural complexity.

3.5.4.1 – Evaluating Control of Displacement on Fault Permeability

In many fault zones, a general relationship has been observed between the magnitude of displacement and the width of the fault damage zone, suggesting a relationship between fault displacement and permeability (e.g. Bense et al., 2013 and references therein). Along the studied region of the NMF, displacement decreases northward towards the fault terminus (Foxford et al., 1996). Segment C in our study area has displacements between ~900 and 300 m, segment B has displacements between ~300 and 250 m, and segment A has displacements between ~250 to 0 m. As mentioned before, a slight trend towards higher cement $\delta^{18}O$ and $\delta^{13}C$ values in samples with mixed cement compositions may indicate decreased abundances of C2 cements towards the northern end of Segment C (Figs. 3.7a and 3.7b), perhaps indicating lower effective permeability and fluid circulation near the fault tip during post-faulting cementation. However, we do not see a first-order correlation between fault-segment slip and the abundance or composition of samples with only C2 cement. Thus, while there may be some displacement-related restriction on the relative amount of C2 cementation along strike, it was not enough to restrict circulation of C2 source fluids from the portions of the fault with the lowest displacement. Displacement is also unable to explain the relative lack of C2 cements along Segment B, which has moderate displacements compared to Segment A and C.

3.5.4.2 – Evaluating Control of Lithologic Composition and Shale-Gouge Ratio on Fault Permeability

The stratigraphy of the Paradox Basin contains a mix of marine, aeolian, fluvial, and lacustrine sediments, providing a range of grain sizes that could cause variability in fluid migration and cementation along the NMF. Entrainment of fine-grained material within a fault is believed to reduce fault zone permeability (Antonellini and Aydin, 1994; Caine et al., 1996; Faulkner et al., 2010; Bense et al., 2013). Along the NMF, lithologies comprise fine-grained siltstones and shale, sandstones, and conglomerates. Some units are fairly homogenous in composition, such as the shale of the Brushy Basin Member of the Morrison Formation and the sandstones of the Navajo Formation and Moab Tongue Member of the Curtis Formation. Other units contain a mix of lithologies, such as the mixed siltstone and sandstone of the Salt Wash Member of the Morrison Formation.

One method for quantifying the potential for such lithologic variability to control fault permeability is the shale-gouge-ratio (SGR), which predicts the relative proportion of fine grained material in a fault based on host rock lithology and displacement magnitude (Yielding et al., 1997). Foxford et al. (1998) reported the range of SGR expected for stratigraphy and displacements associated with the NMF. All three segments have high SGR values, with most locations along the fault having a SGR of ~1.0. The fault zone composition seems to be mainly controlled by the thick mudstones and shales of the Brushy Basin and Mancos Shale in the hanging wall, which provide abundant fine grained material to the fault core. Indeed, observations of exposures of the fault core indicate that the fault composition is dominated by clay gouge, except for locations with displacements less than ~100m and where sandstone is juxtaposed against sandstone

(Foxford et al., 1998). Because there is no evidence for substantial lithologically controlled permeability contrast between segment B and the rest of the fault, we conclude that the lithologic composition of host rock and the fault core cannot explain the observed lack of C2 cementation in segment B.

3.5.4.3 – Evaluating Control of Fault Zone Architecture on Fault Permeability

Fault zone architecture, or the geometry and interconnectivity of fault strands and segments, may also play a role in controlling the distribution of permeability along a fault zone. In particular, areas of structural complexity and fault segment interaction have been identified as zones of higher permeability in a number of ancient and active fault systems and geothermal fields (e.g. Curewitz and Karson, 1997; Davatzes et al., 2005). The relatively high concentration of deformation and cementation around CHJ has been previously interpreted to be controlled by the concentration of stress around intersecting fault segments at that locality (Davatzes et al., 2005; Eichhubl et al., 2009).

The three fault segments defined in this study differ in terms of overall orientation, as well as the geometry of subsidiary segments and occurrence of interacting secondary structures. Segments A and C are relatively linear, have more intersecting secondary structures, and differ in the geometry of subsidiary segments, such as en-echelon fault arrays (Segment A) and splay faulting (Segment C). Segment B is a relatively simple segment of the NMF bridging two areas of structural complexity and enhanced cementation (WTJ and CHJ, Fig. 3.7). It is possible that the relative lack of C2 cements along Segment B reflects less permeability generation due to the absence of interacting secondary structures. This would imply that the main control on the

distribution of permeability along the Moab Fault is the localization of enhanced deformation around segment intersections and zones of structural complexity.

3.5.5 - History of Structurally Controlled Cementation and Diagenesis on the Moab Fault

Here, we synthesize the existing data from the NMF and provide a timeline of deformation, cementation, and diagenesis. Motion along the NMF initiated by the Triassic, likely driven by ductile flow of the basal Paradox Salt Formation (Trudgill, 2011; Foxford et al., 1996). Within the basin sediments, compaction and early stages of faulting were accommodated by the formation of cataclastic deformation bands (Davatzes et al., 2005; Foxford et al., 1996; Johansen et al., 2005), which produced relatively small offsets. Sedimentation continued throughout the Mesozoic into the Tertiary, forming the sequence of Jurassic and Cretaceous sediments exposed along the NMF. Inundation of the region during the Cretaceous by an inland seaway resulted in the deposition of the thick Mancos Shale and the rapid burial of Jurassic strata (Garden et al., 2001; Trudgill, 2011). An early phase of cementation along the NMF (C1) is closely associated with deformation bands, and formed from a marine source fluid at Earth-surface temperatures prior to substantial burial (Hodson et al., 2016).

The Moab Fault underwent a major episode of deformation around 60 to 43 m.y.a. (Pevear et al., 1997; Solum et al., 2005), following rapid burial during the Cretaceous and early Tertiary (Garden et al., 2001). Faulting was driven by the collapse of the Moab Salt Wall (Foxford et al., 1996; Gutiérrez, 2004), and was associated with the fracturing and jointing in the fault damage zone, particularly around fault segment intersections and areas of structural complexity (Davatzes et al., 2005). Newly generated fractures

enhanced the permeability of the fault zone, and fluids began circulating concurrent with (or shortly after) fracture formation (Garden et al., 2001; Hodson et al., 2016). Post-faulting fluids were likely sourced from a carbonate-rich unit that had undergone significant alteration by meteoric waters that equilibrated with the host rock. The fluids interacted to varying degrees with mantle-sourced CO_2 or hydrocarbons (Eichhubl et al., 2009), resulting in the reduction and dissolution of hematite cements and associated bleaching observed along the fault zone (Garden et al., 2001; Eichhubl et al., 2009; Chan et al., 2000). Crystalline C2 cements filled fractures and adjacent pore spaces. Following the initial formation of veins and pore cements, the fluids continued to circulate while the basin was exhumed and ambient rock temperatures decreased. The repeated infiltration of fluids along vein-filled fractures resulted in the partial dissolution and re-precipitation of earlier C2 cement, producing multiple generations of cement with similar C and O isotope compositions, but distinct clumped isotope compositions in equilibrium with cooler fluid temperatures. Exhumation of the central Colorado Plateau began after ~3 m.y.a. (Murray et al., 2016), suggesting that cooler cements may be much younger than the age of faulting, and that post-faulting fluid circulation may have been continuous throughout the Cenozoic.

3.6 – Implications and Conclusion

We explored fault-scale variability in cement chemistry, formation conditions, and structural context to constrain the relationships between fault-related deformation and cementation along the Moab Fault, UT. Our field, thin section, and isotopic observations provide new insight into the timing and duration of cementation along the NMF, the

conditions and associated source fluids for cementation and diagenesis, as well as the structural controls on the distribution of fault zone permeability. The main conclusions for our study are:

1 – Findings from CHJ are representative of the greater Moab Fault Zone, including the relationships between deformation mechanisms and distinct cement compositions. While specific interpretations were refined and modified by the greater scope of this study, the consistency between the local and fault-scale studies highlights the ability of localized studies to provide comprehensive information about processes acting across larger scales. Indeed, use of local-scale studies to develop a detailed framework, such as for the structural and diagenetic history of the Moab Fault Zone, is a powerful tool for larger scale studies with lower sampling density.

2 – Post-faulting cement (C2) temperatures span the range expected between peak burial and exhumation to the surface, suggesting that fluid circulation and associated cementation occurred throughout the post-faulting history of the basin, without the addition of new conduits related to continued motion along the fault. This indicates that fault zones may maintain permeability for prolonged periods after a given deformation event.

3 – Carbonate $\delta^{18}O$, $T(\Delta_{47})$ and $\delta^{18}O_{fluid}$ compositions, along with observed alteration patterns, associated with C2 cements are compatible with cement formation from rock-buffered source fluids. Fluid continued to circulate after initial formation of large crystalline veins and pore cements, partially dissolving and recrystallizing existing C2 cement as the basin was exhumed. This provides a possible mechanism for the maintenance of permeability along the NMF: dissolution of preexisting fracture-filling

cement and veins. Our findings also highlight that diagenetic alteration can obscure geochemical interpretations for primary cements while providing additional information about subsequent diagenetic processes and conditions. Clumped isotope thermometry provides an important constraint for identifying these complex relationships.

4 – A segment of the NMF between two major intersections has a reduced occurrence of C2 cement, suggesting lower relative permeability compared to the rest of the fault zone. Predictive models relating fault zone permeability to displacement-related deformation and fault zone composition fail to adequately explain the observed distribution of C2 cement. This segment is characterized by a relative lack of structural complexity compared to adjacent fault segments, suggesting that focused deformation associated with interacting segments or secondary structures is the primary control on permeability distribution along the NMF.

Our new findings illustrate the potential for long-lived fluid circulation along a fault zone, even in the absence of active structural deformation. Our use of clumped isotope thermometry to measure the precipitation temperatures of fault-hosted cements allows us to more precisely identify the relationships between formation temperature, carbonate composition, and source fluids, and yields insight into the diagenetic conditions that would not be possible with traditional petrographic or bulk isotope analyses alone.

3.8 - Figures

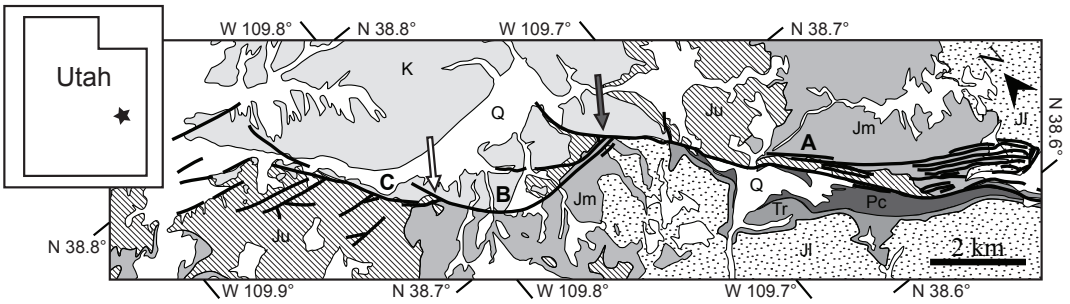

Figure 3.1: Simplified geologic map of the Moab Fault Zone, after Doelling et al. (2001). Fault trace shown by black line. A, B, and C refer to primary fault segments delimited by the locations of prominent fault segment intersections denoted by grey arrow (Courthouse Junction) and white arrow (Water Tank Junction). Unit labels refer to: Pc – Permean Cutler Fm.; Tr – Triassic Chinle Fm. and Moenkopi Fm.; Jl – Lower Jurassic Glen Canyon Group (Navajo Fm., Wingate Fm., and Kayenta Fm.); Jm – Middle Jurassic San Rafael Group (Entrada Fm., Summerville Fm., and Curtis Fm. including Moab Tongue sandstone); Ju – Upper Jurassic Morrison Fm; K – Cretaceous Cedar Mountain Formation and Mancos Shale; Q – Quaternary deposits, undifferentiated.

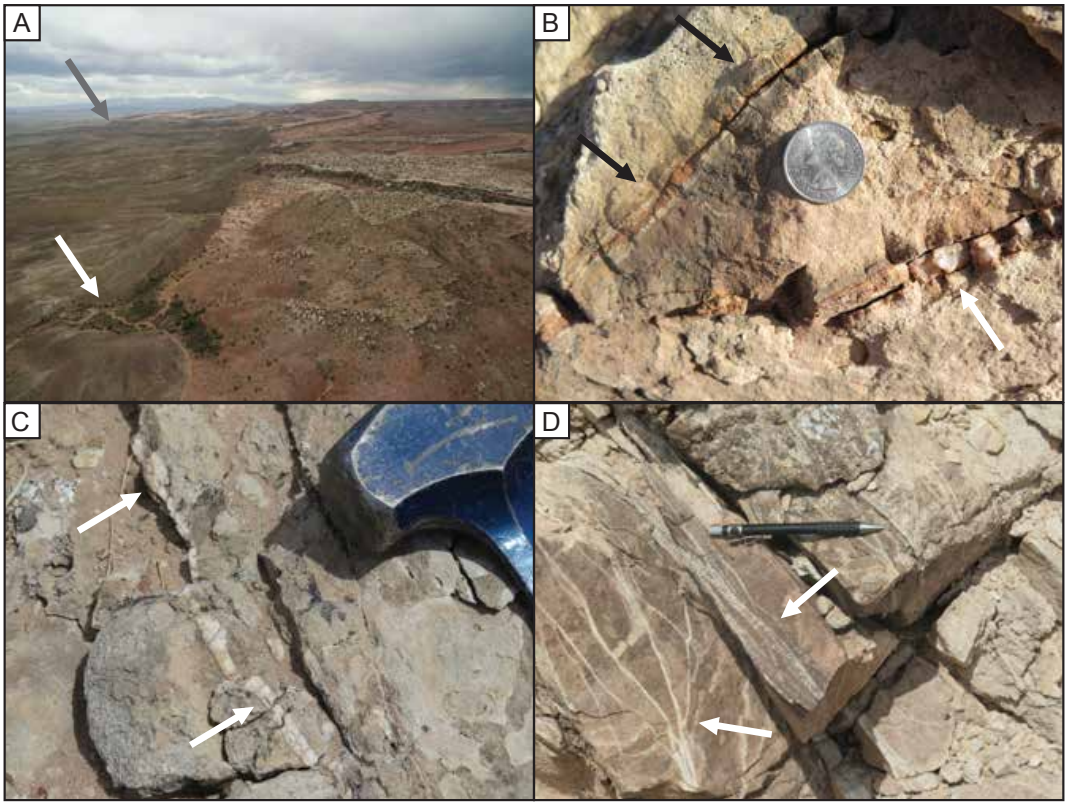

Figure 3.2: Selected field photographs from the Moab Fault Zone. A) Aerial view of the Moab Fault Zone looking to the SW from the Water Tank Junction fault-segment intersection (white arrow). Black arrow marks location of the Courthouse Junction fault-segment intersection. B) Fractures and veins in the damage zone of the Moab Fault. The ~1 cm wide vein filling the lower fracture (white arrow) is characteristic of crystalline veins associated with post-faulting (C2) cementation. Alteration halos with hematite cement can be observed along the fractures (black arrows). Coin is ~2.5 cm (US 25-cent piece). C) Thin C2 vein. Hammer is ~3.5 cm across. D) Deformation bands with white coloration (arrows), displaying anastomosing and branching geometries. Pencil is ~15 cm.

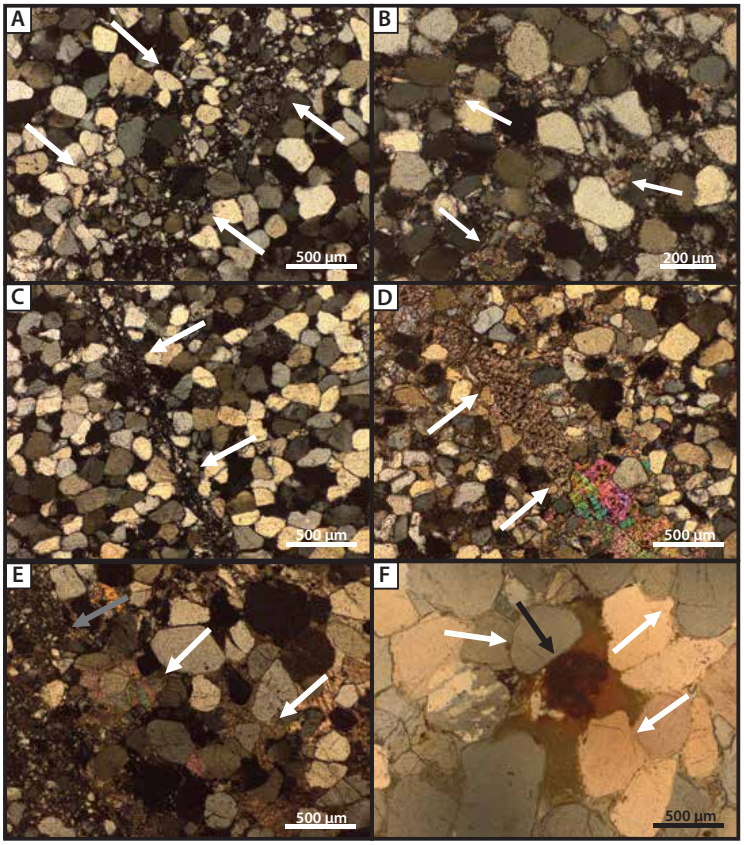

Figure 3.3: Thin section photomicrographs depicting deformation structures and mineral cements observed in this study. A) Deformation band displaying localized, distributed cataclasis. Margins of the structure are marked by white arrows. B) Deformation band with localized cataclastic material intermixed with fine-grained calcite cement (white arrows). C) Deformation band displaying intense, continuous cataclasis. Margins noted by white arrows. D) Fracture filled by crystalline carbonate vein. Margin marked by white arrows. E) Deformation band (grey arrow) adjacent to pore filling C2 cements displaying poikilotopic crystal textures (white arrows). F) Cross-polarized photomicrograph of hematite cement (black arrows). The presence of quartz pressure solution and overgrowth cement is evident in surrounding grains (white arrows).

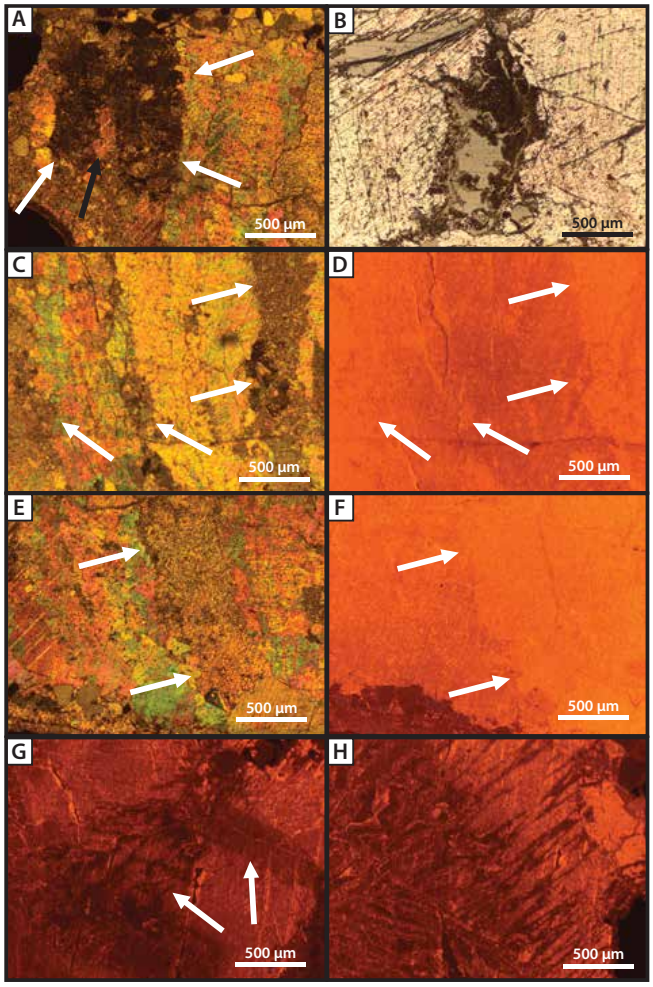

Figure 3.4: Thin section photomicrographs of crystalline carbonate cements and alteration textures. A) Cross-polarized image of blocky calcite crystals with zone of darker fine-grained calcite with irregular borders (white arrows). Note patch of crystalline cement (black arrow) displaying twin planes with similar orientation to carbonate on right side of image. B) Plane light photomicrograph of partially-filled zone of dark, fine grained cement with irregular borders with adjacent crystalline cement. C and D) Paired cross-polarized and cathodoluminescence (CL) images of crystalline carbonate crosscut by bands of finer-grained cement (white arrows). Note that luminescence tends to be brighter within finer-grained bands. E and F) Paired cross-polarized and CL images of crystalline cement with zone of altered material with irregular boundaries (white arrows) and brighter luminescence. G) CL image of crystalline cement with variable luminescence. Darker areas have irregular branching patterns and form halos around fractures and grain boundaries (white arrows). H) CL image of crystalline cement with variable, irregular luminescence patterns.

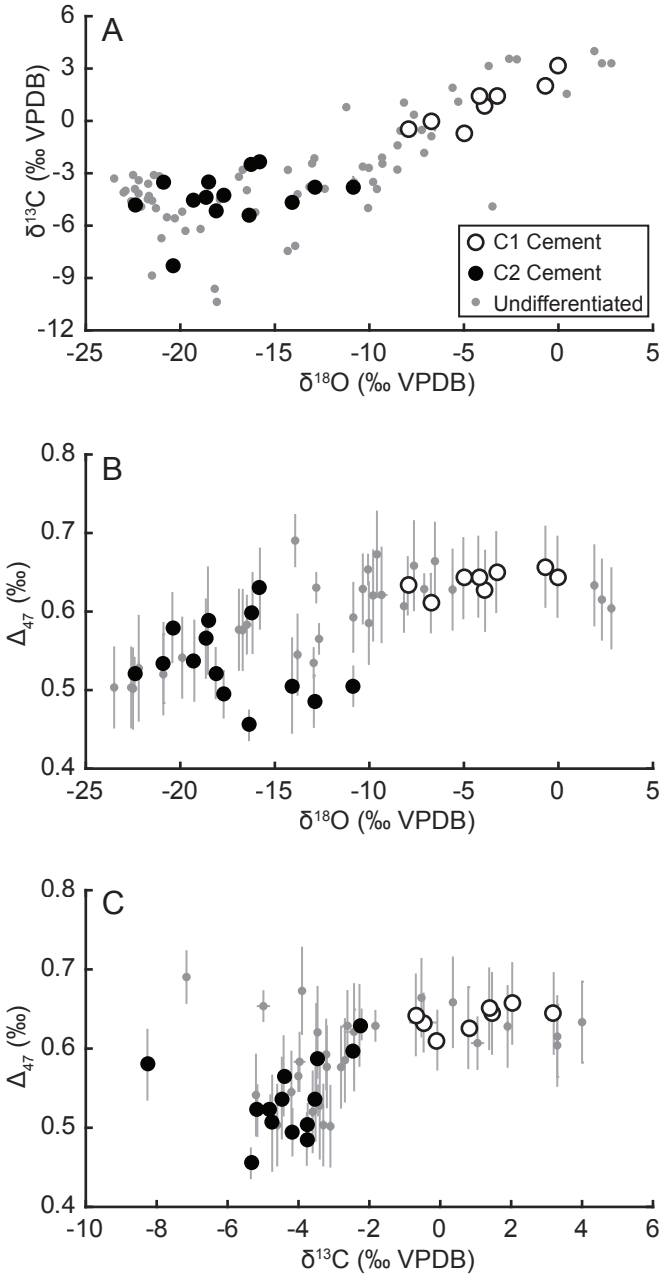

Figure 3.5: Stable isotope compositions of carbonate samples from this study and Hodson et al. (2016). Symbology is the same for all panels. A) $\delta^{13}C$ and $\delta^{18}O$ values from 100 samples from the NMF. B) Clumped isotope composition and carbonate $\delta^{18}O$. C) Clumped isotope composition and carbonate $\delta^{13}C$. Includes recalculated data from Hodson et al. (2016). Error bars denote two standard errors.

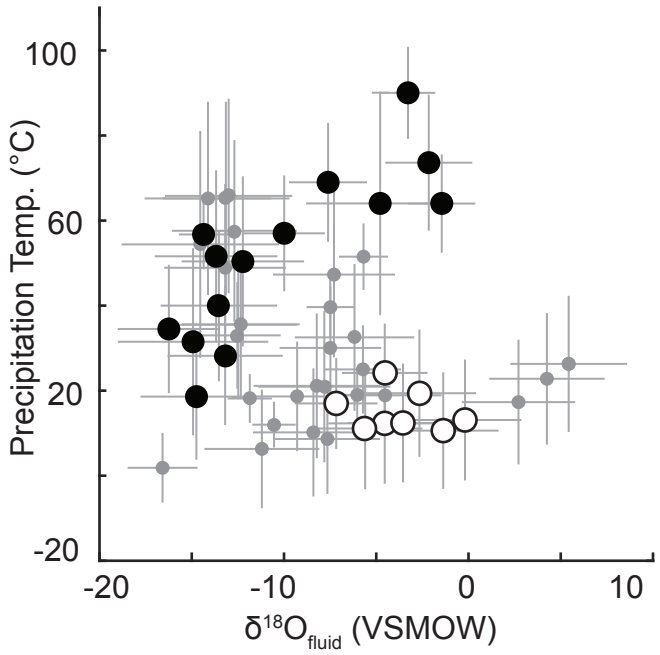

Figure 3.6: Clumped isotope precipitation temperatures and calculated $\delta^{18}O_{fluid}$ compositions for samples from this study and Hodson et al. (2016). Symbology as in Figure 5. Includes recalculated data from Hodson et al. (2016). Error bars denote two standard error.

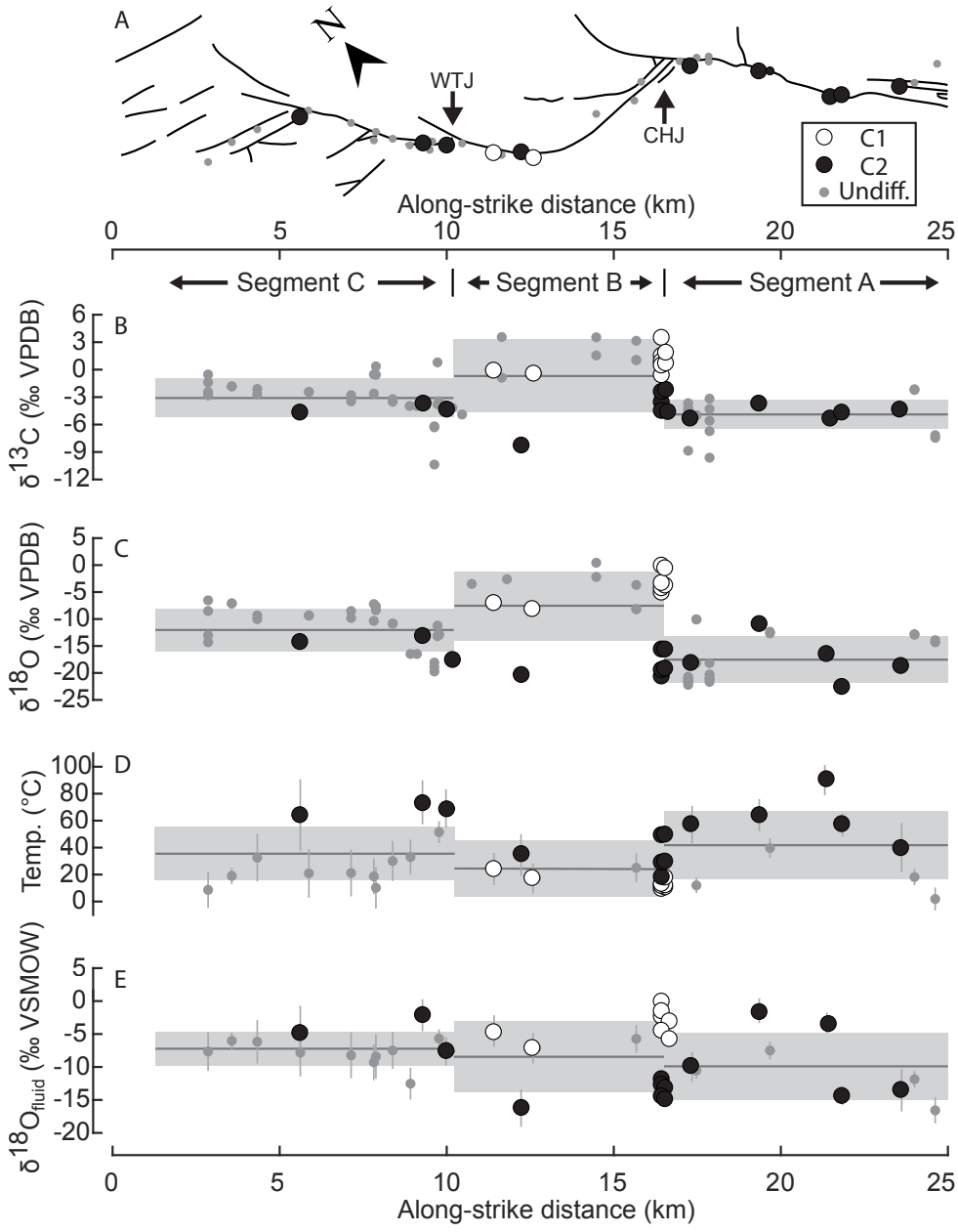

Figure 3.7: Along-strike variation in C and O isotopic composition, precipitation temperature, and $\delta^{18}O_{fluid}$ for samples along the NMF. A) Line-map of the NMF showing fault geometry and location of samples collected for this study. B) Cement $\delta^{13}C$ compositions. C) Cement $\delta^{18}O$ compositions. D) Clumped-isotope precipitation temperatures. E) Reconstructed $\delta^{18}O_{fluid}$ compositions. Horizontal lines and grey boxes denote mean compositions and 1 standard deviation for each of the three fault segments discussed in text.

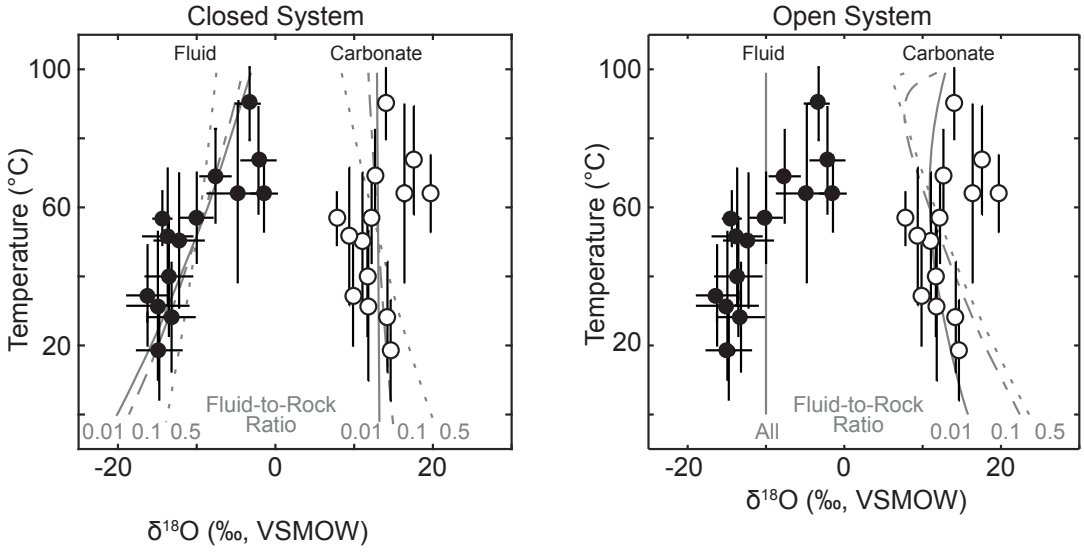

Figure 3.8: Comparison of C2 sample data from this study and Hodson et al. (2016) with predicted trends from the recrystallization model of Banner and Hanson (1990). Sample carbonates are denoted by white dots and associated fluid compositions by black dots. Data shown with two standard errors. Model results plotted as grey lines representing trends for varying fluid-to-rock ratios as labeled on graph. Left panel shows results for closed-system equilibration and right panel shows results for open-system equilibration.

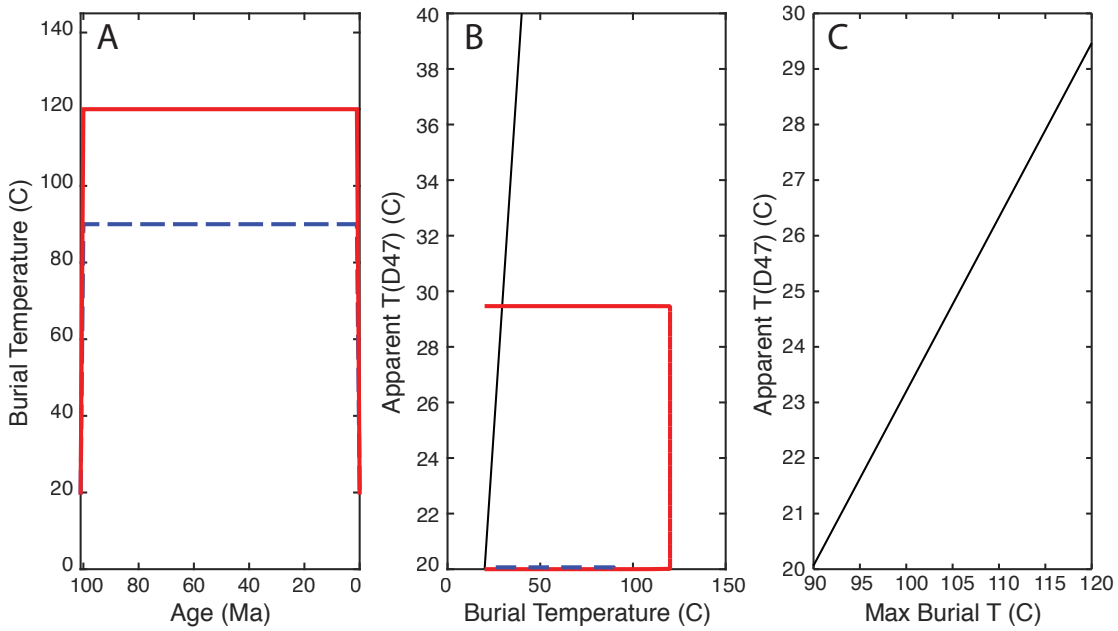

Figure 3.A1 (Supplemental): Results of the clumped isotope thermal reordering model of Henkes et al. (2014) for maximum burial conditions of the Moab Fault. Maximum burial temperatures of 90°C and 120°C were held for 100 Ma. The maximum temperature of 90°C reflects the peak burial temperature from Garden et al. (2001). A) modeled T-t histories used in the model, featuring maximum burial temperatures of 90°C (dashed blue line) and 120°C (solid red line). B) Predicted effect of modeled burial histories on measured T(Δ_{47}). Dashed blue and solid red lines represent 90°C and 120°C maximum burial temperatures, respectively. Solid black line represents one-to-one relationship between burial temperature and apparent T(Δ_{47}). C) Relationship between maximum burial temperatures of 90°C to 120°C and apparent T(Δ_{47}).

Table 1. Clumped isotope compositions

Sample number	$\delta^{13}C$ (‰ VPDB)	$\delta^{18}O$ (‰ VPDB)	Δ_{47} (‰ ARF)	Δ_{47} StdErr (‰ ARF)*	Temp. (°C)	Temp. StdErr (°C)†	$\delta^{18}O_{Fluid}$ (‰ VSMOW)	$\delta^{18}O_{Fluid}$ StdErr (‰)*	Number of replicates	Location§ Lat (°N)	Location§ Long (°W)	Cement Generation**
NMF15-KH01	-0.5	-8.0	0.6329	0.0183	17	6	-7.2	1.3	3	38.71446	-109.78593	C1
NMF15-KH04	-8.3	-20.4	0.5796	0.0221	35	8	-16.2	1.5	3	38.71563	-109.78669	C2
NMF15-KH09	-0.1	-6.7	0.6107	0.0186	24	6	-4.5	1.2	3	38.72060	-109.79341	C1
NMF15-KH14	-1.8	-7.1	0.6287	0.0094	19	3	-6.0	0.5	3	38.77095	-109.86251	-
NMF15-KH17A	-0.5	-6.5	0.6642	0.0245	9	7	-7.6	1.6	4	38.77110	-109.87298	-
NMF15-KH21	-2.7	-10.0	0.5853	0.0260	33	9	-6.2	1.8	3	38.76877	-109.85328	-
NMF15-KH22A	-3.8	-12.9	0.4858	0.0163	74	8	-2.2	1.3	1	38.73399	-109.80984	C2
NMF15-KH24	-4.2	-17.7	0.4944	0.0147	69	7	-7.6	1.2	3	38.73125	-109.80592	C2
NMF15-KH26	-3.5	-12.9	0.5346	0.0094	52	4	-5.7	0.7	3	38.73314	-109.80990	-
NMF15-KH28	-4.0	-16.5	0.5833	0.0184	33	7	-12.5	1.3	3	38.73747	-109.81507	-
NMF15-KH30	-3.5	-9.8	0.6205	0.0287	21	9	-8.2	2.0	3	38.75365	-109.82742	-
NMF15-KH32	-2.6	-10.3	0.6288	0.0219	19	7	-9.3	1.5	3	38.74630	-109.82519	-
NMF15-KH33	-3.2	-10.9	0.5926	0.0220	30	8	-7.5	1.5	3	38.74306	-109.82021	-
NMF15-KH35	0.4	-7.6	0.6584	0.0283	10	8	-8.4	1.8	2	38.74670	-109.82380	-
NMF15-KH41	1.1	-8.2	0.6069	0.0163	25	5	-5.7	1.2	3	38.70833	-109.74779	-
NMF15-KH49A	-4.7	-14.1	0.5058	0.0301	64	15	-4.8	2.4	3	38.76202	-109.83458	C2
NMF15-KH49B	-2.4	-9.4	0.6212	0.0301	21	10	-7.8	2.1	3	38.76202	-109.83458	-
NMF15-KH53A	-5.2	-18.1	0.5216	0.0160	57	7	-10.0	1.2	3	38.70572	-109.72331	C2
NMF15-KH53B	-5.0	-10.1	0.6536	0.0094	12	3	-10.5	0.5	3	38.70572	-109.72331	-
NMF15-KH57A	-4.0	-12.7	0.5652	0.0094	40	4	-7.5	0.6	3	38.70369	-109.71935	-
NMF15-KH58	-3.7	-10.9	0.5049	0.0126	64	6	-1.5	1.0	3	38.69120	-109.70583	C2
NMF15-KH59B	-7.2	-13.9	0.6904	0.0163	2	4	-16.6	1.0	1	38.66268	-109.66191	-
NMF15-KH60A	-2.2	-12.8	0.6304	0.0094	18	3	-11.9	0.6	4	38.66365	-109.67113	-
NMF15-KH60B	-4.4	-18.7	0.5655	0.0250	40	10	-13.5	1.7	3	38.66365	-109.67113	C2
NMF16-01	-5.3	-16.4	0.4551	0.0094	90	6	-3.3	0.8	3	38.67304	-109.69156	C2
NMF16-02	-4.8	-22.4	0.5222	0.0094	57	4	-14.4	0.7	3	38.67169	-109.68872	C2

*Standard error calculated using the standard deviation of replicate analyses or internal standard C64 (0.01630).

†Temperatures calculated using the 90°C temperature calibrtion of Kelson et al. (2017), without a 25°C acid fractionation correction.

§Location accuracy is approximately 5 m.

**C1 and C2 denote the relative timing of cementation events as discussed in text. Samples with mixtures of both generations or undifferentiated timing are denoted with "-".

Chapter Four

Pressures of formation and mineral preservation in fault-hosted carbonate veins: insight from clumped isotope thermometry and fluid inclusions

4.0 - Abstract

Since its introduction a little over a decade ago, carbonate clumped isotope thermometry has established itself as an important stable isotope technique for measuring the formation temperature of carbonate minerals. Recent work applying clumped isotopes to fault-hosted carbonate veins and cements have provided valuable new insight into fault-fluid interactions, particularly with regard to: 1) relationships between fault-zone deformation and fluid migration; and 2) thermal and diagenetic conditions associated with cementation. In this paper, I combine clumped isotopes with fluid inclusion microthermometry, a complementary method for estimating mineral growth temperatures. Expected relationships between these two methods allow for the identification of samples that retain information about primary growth conditions or have experienced secondary alteration. In addition to aiding in the interpretation of temperature estimates, combination of the methods allows for the estimation of ambient pressure during crustal growth. Fluid pressure within a fault zone has been proposed as an important component of the state of stress within the fault, possibly exerting strong controls over the seismic cycle. Additionally, pressure estimates may help identify elevated geothermal gradients associated with focused fluid flow along a fault zone.

Here, I apply clumped isotopes and fluid inclusions to a suite of natural carbonate samples collected from three fault zones and a geothermal exploration well. Poor analytical reproducibility during the analytical period resulted in large analytical

uncertainties in clumped isotope measurements. Using carbonate standards and equilibrated CO_2 gasses, I propose a correction to my temperature measurements. Corrected clumped isotope temperatures follow predicted relationships with fluid inclusions much more consistently, and I use these temperatures to estimate fluid pressure during vein formation. Pressures and temperatures are interpreted in the context of fault-fluid processes, including the possibility of elevated geothermal gradients or sub-hydrostatic pressure associated with fault slip.

4.1 - Introduction

Determining the formation temperature of carbonate minerals is an important component of many geological studies focusing on paleoclimate, reconstruction of past landscapes, burial diagenetic processes, fault-fluid interaction, and the composition and source of associated source fluids. Since being introduced by Ghosh et al. (2006), clumped isotope paleothermometry has emerged as a prominent stable isotope technique for measuring the formation temperature of carbonate minerals. While more traditional isotope thermometry techniques, such as $\delta^{18}O$, are influenced by both the formation temperature and source fluid for a mineral, clumped isotope compositions, or Δ_{47} values, are sensitive to temperature alone. This difference allows the direct estimation of the mineral growth temperature, without requiring assumptions about source fluid compositions. In fact, when combined with a $\delta^{18}O$ measurement from the same sample, the Δ_{47} value allows for the source fluid $\delta^{18}O$ value to be estimated via well-understood fractionation relationships between a carbonate and its source fluid (Kim and O'Neil, 1997). This ability to directly address formation temperature and source fluid

composition has led to the adoption of clumped isotope thermometry across a range of geologic applications.

To date, the primary application of this method has been to surface-related geologic problems, such as paleoclimatology and paleoaltimetry (e.g. Snell et al., 2014; Lechler et al., 2013; Garzione et al., 2014; Huntington et al., 2007, 2010), which track changes in the formation temperatures of surface-forming carbonate to interpret changes in earth's climate or cooling associated with surface uplift. However, clumped isotopes are being increasingly applied to a broader range of geologic problems associated with higher-temperature carbonate-forming processes occurring throughout the upper crust. Such applications have included carbonate diagenesis (e.g. Budd et al., 2013; Huntington et al., 2011), dolomitization (e.g. Ferry et al., 2011; Honlet et al., 2018), fault zone cementation and fluid flow (e.g. Hodson et al., 2016; Bergman et al., 2013; Swanson et al., 2012; Luetkemeyer et al., 2016; Hodson et al., *in review*), and the burial conditions and source fluids associated with concretion growth (Dale et al., 2014). Because many carbonate stable isotope studies are primarily interested in temperature, clumped isotopes are expected to advance a host of additional geologic questions that were previously limited by the assumptions associated with interpreting $\delta^{18}O$ values.

In order to provide additional insight into the behavior of clumped isotope thermometry, we combine clumped isotope thermometry with fluid inclusion microthermometry: a long-standing technique that uses phase changes within small pockets of fluid trapped during crystal growth to estimate the temperature of the fluid at the time of trapping. As with clumped isotopes, fluid inclusion microthermometry is also sensitive to secondary alteration, primarily through the loss of integrity of the fluid

inclusion, such as volume changes or decrepitation and fluid loss (Goldstein, 2001). Because fluid inclusion measurements characterize a physical property of the crystal, while clumped isotopes characterize a chemical property, these two methods represent complementary approaches to estimating carbonate growth temperatures. Combining them not only provides a second line of support for an interpreted growth temperature, but also creates opportunities to explore additional properties of the system and identify the presence of formation or alteration processes acting during and after formation of the mineral.

In addition to temperature, fluid inclusions can provide information about the pressure conditions during entrapment and source fluid compositions (Zhang and Frantz, 1987). Samples are heated on a temperature-controlled microscope stage, and temperatures for phase-homogenization (the homogenization temperature) are used to infer a minimum trapping temperature for the inclusion. Interpretation of the true trapping temperature generally requires assumptions about the pressure conditions during mineral growth (e.g. hydrostatic, lithostatic), but the P-T relationship may be inverted to infer a trapping pressure if an external temperature is available, such as from clumped isotope thermometry (e.g. Luetkemeyer, 2014; Honlet et al., 2018). Because fluid inclusions estimate a minimum temperature, while clumped isotopes estimate the true temperature, we may not expect clumped isotopes and fluid inclusions to provide the same result. However, expected relationships between the two systems may be used to evaluate whether the measured temperatures reflect primary mineral growth or diagenetic alteration.

In this study, I present a combined clumped isotope and fluid inclusion dataset from fault-hosted carbonate veins. I use these data to identify samples that do and do not follow the expected relationships for primary growth temperature, and provide estimates for P-T conditions during mineral growth or diagenesis. In addition, I leverage the large number of carbonate standard replicate analyses measured in IsoLab at the University of Washington to characterize the uncertainty in Δ_{47} measurements for carbonates with formation temperatures between 18 and 600°C. Skewed distributions for carbonate standards indicate that Δ_{47} measurements are biased towards room temperature values, systematically underestimating temperature estimates. I characterize the effect of this bias on interpreted clumped isotope temperatures and propose a new standards-based correction for Δ_{47} values measured from sample unknowns. Using my clumped isotope and fluid inclusion dataset, I demonstrate that our new corrected temperatures produce more reasonable estimates of carbonate growth conditions for my samples.

4.2 - Sample Descriptions and Geologic Context

For this study, 13 samples were collected for isotopic and fluid inclusion analysis from locations across the western USA, including: 1) the Moab Fault in southeast Utah; 2) the Hurricane Fault in southern Utah and Northern Arizona; 3) fault zones in the Rocky Mountain thrust belt; and 4) the Mountain Home geothermal exploration borehole in the western Idaho. Twelve samples come from fault zones, with eight from normal fault systems and four from reverse fault systems. One sample was collected from a basalt layer near the base of the Mountain Home borehole. Samples from the Hurricane Fault and Mountain Home borehole were provided by Dennis Newell from the University

of Utah and Rocky Mountain Thrust samples were provided by David Brink-Roby from the University of Rochester. Examples of samples used in this study are shown in Figure 4.1.

4.2.1 - Moab Fault, UT

The Moab Fault zone in southeast Utah is an exhumed, inactive normal fault system cutting a sequence of late Paleozoic to early Tertiary sedimentary rocks within the Paradox Basin on the Colorado Plateau. The northeast-dipping, ~45 km long fault is well exposed in multiple canyons, and features a well developed fault core and asymmetrical damage zones. The footwall damage zone contains abundant deformation bands, which extend some 5 or 10 meters into the host rock. The hanging wall damage zone forms a broad monocline, with geometry suggestive of drag folding (Berg and Skar, 2005). Displacement reaches up to one kilometer along the fault (Foxford et al., 1996), which was driven by the growth and collapse of ductile salt underlying the basin (Gutiérrez, 2004). Faulting had begun by the Triassic and continued into the early Tertiary (Trudgill, 2011). The large crystalline veins sampled in this study fill fractures formed during the final stages of faulting (Davatzes et al., 2005; Eichhubl et al., 2009). Following fracturing, veins continued to form over the next 60 Ma while the basin was exhumed to its present level (Hodson et al., 2016; Hodson et al. *submitted*).

Five samples from the Moab Fault were collected from veins within the fault core and footwall damage zone. Samples were impregnated in epoxy and halved. One side was used to prepare thin and thick sections for petrographic and fluid inclusion measurements. The other side was subsampled for isotopic analysis by extracting

multiple crystals from a single vein and homogenizing in a mortar and pestle. One sample, MCE15-KH02, was subsampled using a hand-held dental drill. Minor amounts of host rock (less than 1%) were incorporated during subsampling of some veins. Sample NMF15-KH58 is an approximately 1 cm wide carbonate vein from the fault damage zone within the Permian Cutler Formation comprising blocky crystals 0.5 to 1 cm across. Sample TMG15-KH03 is a blocky, 0.5 to 1 cm wide carbonate vein collected from the fault damage zone within the Jurassic Salt Wash Member of the Morrison Formation. The sampled vein contains thin, elongate crystals approximately 0.5 mm wide and 1 mm long. Sample NMF14-KH05 is a large calcite vein composed of 1 to 3 mm blocky crystals collected from the fault core in the Lower Jurassic Tidwell Member of the Morrison Formation. Sample NMF14-KH06 is an irregular vein in red siltstone of the Lower Jurassic Tidwell Member of the Morrison Formation featuring a wide range of crystal sizes with blocky morphologies ranging from 0.05 to 5 mm. Sample MCE15-KH02 is a ~0.75 cm wide calcite vein from within a fault-segment relay zone in the Moab Tongue Member of the Curtis Formation. Calcite crystals are elongate, ~1 mm wide and 1.5 to 2.5 mm long.

4.2.2 - Hurricane Fault, UT and AZ

The Hurricane Fault is a ~250-km long west-dipping normal fault that forms the boundary between the Colorado Plateau and Basin and Range province in southern UT and northern AZ (Anderson and Mehnert, 1979). This extensional system is actively deforming with slip rates of 0.2 to 0.6 mm/yr, and approximately 850 m of vertical offset since the mid Miocene or early Pliocene (Lund et al., 2007). The fault displaces

Paleozoic and Mesozoic strata in surface outcrops that form a prominent escarpment (the Hurricane escarpment), and the footwall of the fault zone is well exposed in E-W trending canyons. Fluids from two distinct sources formed carbonate veins within the fault zone, including meteoric fluids and basin brines (Koger, 2017).

The three samples from this fault are from the footwall damage zone, within tens of meters of the Quaternary trace of the fault. Samples "3-5 to PT-1/s-7" and "3-4/S-4" are sandstone-hosted sparry calcite veins from the Timpoweap Member of the Triassic Moenkopi Formation and the Permian Queantoweap Sandstone, respectively, featuring blocky crystals between 0.1 and 5 mm in diameter. Sample "1-4/s-4 (A)" is a sparry calcite-cemented breccia adjacent to laminated calcite veins in sandstone host rock of the Permian Hermit Formation, with blocky 0.5 to 1 mm crystals. All three samples from the Hurricane Fault were micro-sampled for clumped isotope analysis using a tungsten carbide dental drill.

4.2.3 - Rocky Mountain Thrusts

The Rocky Mountains are a continental-scale topographic feature formed during the Cretaceous to Early Tertiary along a convergent margin between the North American and Farallon tectonic plates. Two distinct, but temporally coincident, orogenic episodes acted along the margin, with the Sevier Orogeny producing a thin-skinned fold and thrust belt and the Laramide Orogeny generating block uplifts along steeply dipping reverse faults. The progressive advance of thrust faulting into the foreland resulted in the expulsion of formation waters and the formation of carbonate veins along the fault zones.

The four samples from the Rocky Mountain Thrust Belt come from one or more faults somewhere in Idaho, Montana, Wyoming, Colorado, Utah, or New Mexico. Host rock is a grey, fine-grained limestone. Samples WS14-29, WS15-GCS, and WS15-70 are wide veins, ~0.5 to 2 cm across, and contain blocky calcite crystals between 0.1 and 5 mm across. Sample WS14-49 is a thin, 2 mm wide vein containing elongate calcite crystals ~0.5 mm wide and ~1 mm long. Carbonate material was extracted from thin section blanks using a tungsten carbide dental drill.

4.2.4 - Mountain Home Borehole, ID

Sample MH-C-1799 was recovered from the Mountain Home–2 exploration borehole, which was drilled in 2011 as part of a DOE funded geothermal exploration project. The borehole was located on the northwest corner of Mountain Home Air Force Base, in the Western Snake River Plain, Idaho. The borehole was advanced through approximately 1820 meters of interbedded lacustrine deposits from paleo-Lake Idaho and basalt flows dated between ~5 and 9 Ma. The sample is a sparry calcite vein collected from a hydrothermally altered basalt layer located 1799 meters below the ground surface. Carbonate material for clumped isotope analysis was extracted from the hand sample with a tungsten carbide dental drill.

4.3 - Methods

To identify evidence for secondary alteration or multiple generations of carbonate, all samples were characterized in thin or thick section using petrographic and cathodoluminescence microscopy prior to analysis. Areas within samples were targeted

for subsampling based on the presence and quality of fluid inclusions. Care was taken to extract material for clumped isotope analysis from the same portions of the sample containing measured fluid inclusions, although in some cases exact correspondence could not be precisely determined due to irregular vein geometry or additional material being needed to meet analytical needs (greater than ~20 mg calcite). Carbonate was extracted either by grinding using a tungsten-carbide dental drill or chipping off pieces of individual crystals and homogenizing with an agate mortar and pestle. Small amounts of host rock (<1%) were incorporated into some samples with especially fine features.

Fluid inclusion analyses were performed by Dennis Newell at Utah State University (Hurricane Fault and Mountain Home borehole samples) and by David Brink-Roby and Mark Evans at Central Connecticut University (Moab Fault and Rocky Mountain Thrust samples). Doubly-polished thick sections (~100um thick) were prepared for all samples. A Linkam MDS-600 heating and cooling stage was used to measure homogenization temperatures (Th) in both laboratories. For samples with freezing data, salinities were calculated using the freezing temperature relationship of Gasparrini et al. (2006). The equations of state of Zhang and Frantz (1987) were used to construct isochores and calculate trapping pressures for fluid inclusions. Because multiple fluid inclusions within a single sample may have formed during multiple distinct trapping events, we cannot necessarily assume that the range of Th measurements represents natural variability about a single mean. Because of this, we choose to represent the observed variability as the standard deviation of measured Th, not the standard error as is more commonly used for clumped isotopes and geochemical analyses.

Clumped isotope analyses were performed at IsoLab at the University of Washington. Carbonate samples were digested in phosphoric acid at 90°C, and the evolved CO_2 was purified under vacuum following methods described by Burgener et al. (2016) and Hodson et al. (2016). Purified gasses were then stored in flame sealed borosilicate glass tubes until analysis. An external (ETH1, ETH2, ETH3, or ETH4) or internal (C2, C64, or Coral) laboratory standard was purified between every four to five samples. Clumped isotope analyses were performed on a Thermo MAT 253 isotope ratio mass spectrometer configured to measure *m/z* 44-49 (inclusive). The pressure baseline correction, first introduced by He et al. (2012), was applied using the approach of Schauer et al. (2016). Values for Δ_{47} were calculated using the methods of Huntington et al. (2009), except that values for $\delta^{13}C$ and $\delta^{18}O$ were calculated using the updated ^{17}O correction values determined by Brand et al. (2010), following the methods of Daëron et al. (2016) and Schauer et al. (2016), and Δ_{47} is reported in the absolute reference frame (Dennis et al., 2011) with no acid fractionation factor. Outlier measurements of reference frame gasses and carbonate standards were identified statistically using the Pierce outlier test and excluded from reference frame construction and standard-based calculations of analytical reproducibility. Values of Δ_{47} were converted to temperatures using the calibration of Kelson et al. (2017), which was generated in the same laboratory as my analyses using the ^{17}O correction factors of Brand et al. (2010). Reported uncertainties for mean Δ_{47} values are reported as 95% confidence intervals based on the standard error and number of replicate analyses using Student's critical t-value (e.g. Huntington et al., 2009). In cases where the standard deviation of replicates was lower than the long-term standard deviation of the best characterized internal standard (C64, 1SD = 0.033 ‰), the

standard deviation of the internal standard was used in its place and used to calculate standard errors and 95% confidence intervals.

4.4 - Results

4.4.1 – Fluid Inclusions

Between two and thirteen two-phase fluid inclusions were analyzed for each of the thirteen samples in this study. Average homogenization temperatures for the inclusions range from 55 to 171°C, with standard deviations between 1 and 41°C (Table 1). Samples from the Moab fault were generally inclusion poor. For each of the five samples from this region, between two and five inclusions were measured. Mean fluid homogenization temperatures for these samples range from 60 to 123°C, with standard deviations between 2 and 41°C. Fluid inclusions were measured in three samples from the Hurricane Fault zone. Measured inclusions range in size from 5 to 40 microns in diameter. These are interpreted as primary inclusions, and evidence for secondary inclusions is minimal. Between two and 13 inclusions were measured from each sample, yielding a narrow range of mean temperatures between 72 and 76°C. Associated standard deviations are between 2 and 10°C. Inclusions were primarily single phase in sample 1-4/s-4, and only two two-phase inclusions were found.

For the four samples from the Rocky Mountain Thrust Belt, homogenization temperatures were measured for two to six inclusions per sample. Average homogenization temperatures range from 55 to 171°C, with standard deviations between 1 and 17°C. For one sample, WS14-29, six measured inclusions have a bimodal distribution, with three inclusions over 200°C and three below 125°C. The hotter

temperatures were all measured from the same location within the sample, and I interpret these temperatures to record two distinct generations of carbonate growth. Because the lower range of homogenization temperatures overlaps with the clumped isotope temperature estimates from this sample (mean T(Δ_{47}) of 92 ± 34°C), we use the mean and standard deviation of the cooler set of homogenization temperatures for comparison below.

Three inclusions were measured from the Mountain Home borehole sample, returning homogenization temperatures from 135 to 147°C (mean = 141 +/- 6°C). Inclusions were two-phase and averaged ~15 microns in diameter. A melting temperature of -0.1 °C was measured for this sample, equating to 0.18 wt % NaCl (Gasparrini et al., 2006).

4.4.2 - Clumped Isotopes

Clumped isotope compositions were measured for the 13 samples in analyzed for this study (Table 4.1). Five replicate analyses were performed for all samples, with the exception of sample WS14-49 from the Rocky Mountain Thrust Belt, which was analyzed only twice due to limitations on sample material (Fig. 4.2). Mean Δ_{47} values for these samples range from 0.411 to 0.566 ‰, with standard errors between 0.015 and 0.036 ‰ and 95% confidence intervals ranging from 0.041 to 0.408 ‰. These Δ_{47} values correspond to apparent temperatures of 39 to 118°C with 95% confidence intervals between 17 and 95°C. The highest uncertainty is associated with the sample with the lowest number of replicates (WS14-49, n=2), which was sample-limited due to the size of the sampled vein.

For the five samples collected from the Moab Fault, mean Δ_{47} values range from 0.448 to 0.553 ‰, with 95% confidence intervals between 0.041 and 0.075 ‰. Corresponding apparent temperatures range from 44 to 94°C, with 95% confidence intervals between 16 and 29°C. The three samples collected from the Hurricane Fault have mean Δ_{47} values ranging from 0.480 to 0.539 ‰, with 95% confidence intervals ranging from 0.056 to 0.097 ‰. Apparent temperatures range from 50 to 77°C, with 95% confidence intervals between 23 and 33°C. Four samples from the Rocky Mountain thrust belt have mean Δ_{47} values ranging from 0.452 to 0.566 ‰, with 95% confidence intervals between 0.050 to 0.408 ‰. Corresponding apparent temperatures for these samples range from 39 to 92°C, with uncertainties between 17 and 95°C. The highest uncertainty is due to the small number of replicates for sample WS14-49 (n=2), and the sample actually has a modest standard error of 0.032 ‰, similar to the standard deviation of the carbonate standards (~0.03 ‰). The sample from the Mountain Home Borehole has an average Δ_{47} value of 0.411 ± 0.098 ‰ (95% confidence interval). These values correspond to an apparent temperature and uncertainty of 118 ± 56°C.

Over the analytical period in which samples for this study were analyzed (December 2016 to March 2018), the seven carbonate standards were analyzed a total of 740 times. Total numbers of replicates for each individual standard are given in Table 2. The long-term stability of equipment in IsoLab at the University of Washington has allowed for the accumulation of many replicates for each standard, yielding well-constrained distributions. For this study, internally accepted values for these standards are taken to be the modal Δ_{47} value for all replicates (Table 4.2).

4.5 - Discussion

Our new clumped isotope and fluid inclusion data allow us to compare temperature estimates from two independent methods. Replicate clumped isotope measurements for the new dataset have poor reproducibility relative to internal carbonate standards, resulting in large uncertainties that hinder the comparison of the two thermometry methods. In the following section, I provide a discussion of the major sources of error and uncertainty when measuring and interpreting clumped isotope compositions. I then present a new approach for characterizing and correcting for analytical error using carbonate standards, and combine these preferred clumped isotope temperatures with fluid inclusion temperatures to demonstrate improved correspondence between the methods. Finally, I use the combined temperature data to interpret the formation temperatures and pressures, as well as the diagenetic histories, for the samples.

4.5.1 - Uncertainty in Clumped Isotope Analysis

4.5.1.1 - Analytical Uncertainty

Clumped isotope thermometry is a stable isotope technique requiring high-precision measurements, pushing the analytical limits of modern gas-source ion-ratio mass spectrometers. Because of the requirements of the measurement, analytical precision is fundamentally restricted by the analytical limits of the instrument, or "shot-noise", during data acquisition (Huntington et al., 2009). To achieve higher precision, samples are routinely analyzed in replicate, which allows estimation of the standard error and calculation of a 95% confidence interval by multiplying the standard error by Student's t-factor (Huntington et al., 2009). Student's t-factor is dependent on the number

of replicate analyses, decreasing from 12.7 for two replicates to 2.8 for five replicates. For this reason, Fernandez et al. (2017) recommended ten replicate analyses for a single sample, although this is often not practical due to the amount of sample material required (~8 mg per replicate) as well as increased analytical time and expense. For unknown samples with smaller numbers of replicate analyses ($n < \sim5$), it is not uncommon for internal reproducibility to be less than that of the carbonate standards during the same analytical period. In these cases, particularly when there are multiple standards with similar reproducibility, it is likely fortuitous circumstance that led to the high sample reproducibility, and it has been recommended that the long-term standard deviation from standards be used in place of the low value taken from sample replicates (Fernandez et al., 2017).

4.5.1.2 - Calibration Selection and Uncertainty

To date, a large number of calibration studies relating Δ_{47} to growth temperature have been published, varying in laboratory methods, temperatures of carbonates used, and the number of replicate analyses for each sample (Kelson et al., 2017; Fernandez et al., 2017; Schauer et al., 2016; Daëron et al., 2016). Differences in the Δ_{47}-temperature relationships between different studies are likely controlled to some degree by all of these variables, but Kelson et al. (2017) and Fernandez et al. (2017) showed that much of the variability could be explained by expected analytical uncertainty associated with measurement accuracy, numbers of replicate analyses, and the range of temperatures used in the calibration. For this study, we use the Δ_{47}-temperature calibration of Kelson et al. (2017), which incorporates a relatively large number of replicates and wide range of

temperatures. Additionally, this calibration dataset was generated in the same laboratory as the data for this study, reducing the potential for error due to inter-laboratory differences in analytical procedure.

4.5.1.3 – Equilibration of Sample CO_2 with Water During Purification of CO_2

Prior to analysis on a mass spectrometer, carbonate samples must be converted to CO_2 by acid dissolution in phosphoric acid. The resultant CO_2 is then purified of water via vacuum cryogenic methods (Ghosh et al., 2006). During this step, gases are typically passed through gas chromatography (GC) resin, such as Poropak-Q, to separate non-CO_2 gases with the potential for interference with the mass-47 signal for clumped CO_2 molecules (e.g. Huntington et al., 2009). While the CO_2 purification step is designed to separate water and limit the presence of contaminant molecules, this process can provide opportunities for isotope fractionation during acid dissolution and reaction with the GC resin, as well as re-equilibration between CO_2 and water vapor before cryogenic separation or if the separation is incomplete. Fractionation constants have been measured for acid dissolution (Defliese et al., 2015). Fractionation behavior between sample CO_2 and GC resin has not been characterized, but the effects are assumed to be negligible. The primary goal of the cryogenic purification step is to separate water vapor from CO_2, but there are opportunities for re-equilibration between the two gasses during transfer into the cryogenic traps and within the Poropak-Q GC resin. Indeed, patterns in the carbonate standards measured in IsoLab indicate re-equilibration of CO_2 Δ_{47} values towards room temperature values. These patterns are described in detail below.

4.5.1.4 - Other Non-Analytical Sources of Error

In addition to re-equilibration of Δ_{47} values during purification of CO_2 prior to analysis on a mass spectrometer, additional error can be introduced to a sample at multiple stages during sample preparation as well as the interpretation of results. Methods for extracting small carbonate features from hand samples often include a rotary drill or micromill, which may heat samples to the point of altering their original Δ_{47} composition. Small particle sizes generated using drilling methods may also allow carbonate to re-equilibrate with room air, as has been shown for $\delta^{18}O$ values from samples collected using a micromill (Tobin et al., 2011). Slow grinding with low force, such as the approach used in this study, can minimize these effects, along with long-term storage in a low-humidity desiccator.

Sample heterogeneity, possibly from the combination of carbonate features with distinct Δ_{47}, $\delta^{13}C$, or $\delta^{18}O$ values, may not only decrease the reproducibility of replicate analyses, but yield final Δ_{47} values that are outside the temperature range of the combined carbonate features (Defliese and Lohmann, 2015). Careful homogenization of extracted sample powders, along with the relatively large mass of sample used per replicate (~8 mg), should minimize the effect of reproducibility issues stemming from sample heterogeneity. However, the effects of mixing on measured Δ_{47} values may lead to incorrect interpretations of the mineral formation temperature, particularly in the case of coexisting carbonates with distinct $\delta^{13}C$ and $\delta^{18}O$ values. To minimize the chance of incorporating multiple generations of calcite into a single sample, care should be taken to characterize a sample prior to Δ_{47} analysis, such as through thin section petrography and cathodoluminescence microscopy, or through preliminary measurements of $\delta^{18}O$ and

$\delta^{13}C$ values to characterize the internal variability in the sample prior to extracting the larger amounts of sample needed for clumped isotope measurements.

In addition to uncertainties from sample preparation and heterogeneity, the formation conditions and alteration history of a carbonate may modify or completely reset its clumped isotope composition. Rapid mineral growth may violate the assumption of thermodynamic equilibrium controlling Δ_{47} values, instead incorporating kinetic fractionation from rapid dissolution or inheriting the Δ_{47} composition of unexpected carbonate speciation in fluids with high or low pH values (Hill et al., 2014; Tripati et al., 2015; Watkins and Hunt, 2015). Chemical alteration due to secondary diagenetic processes can modify a carbonate's primary Δ_{47} composition, typically through the replacement or recrystallization of earlier carbonate mineral. Sustained periods at elevated temperatures, such as during burial or when exposed to a nearby intrusion, can drive thermal re-equilibration through solid-state reordering of C-O bonds within the crystal lattice (Henkes et al., 2014; Passey and Henkes, 2012). All of these processes may produce a Δ_{47} value that is not representative of the primary growth temperature for the sampled carbonate. Consideration of the formation conditions and burial and alteration history of a sample is critical for the interpretation of Δ_{47} values, particularly for samples from new or relatively unconstrained applications of clumped isotope thermometry. Some of these effects can be mitigated through careful sample characterization in thin section. The effects of a sample's thermal history on measured Δ_{47} values may be modeled if external constraints on the thermal history of the system are known (Passey and Henkes, 2012; Henkes et al., 2014).

4.5.2 - Evidence for Temperature Bias from Carbonate Standards

As is standard practice for carbonate stable isotope analyses, carbonate standards are analyzed alongside sample unknowns during each analytical period. In the IsoLab analytical facility at the University of Washington, at least one of seven standards are included with sample powders during each daily session of cryogenic sample cleaning and analysis on the mass spectrometer (Table 2). Four of these are international standards used by clumped isotope facilities around the world (ETH1, ETH2, ETH3, and ETH4), and three are internal standards used only at the University of Washington (Coral, C2, and C64). The four international standards have preliminary published Δ_{47} values (Meckler et al., 2014; Schauer et al., 2016). While some methods have been proposed for using carbonate standards to correct sample data, such as the secondary reference frame of (Dennis et al., 2011) and the "LIDI" method of (Meckler et al., 2014), the clumped isotope community has yet to embrace a method for inter-laboratory corrections. Here, we present a new method for using carbonate standards measured in IsoLab to identify and correct for errors induced by the CO_2 purification process used at the University of Washington.

By using the entire dataset of carbonate standards and reference gasses, including the outlier replicates that are statistically culled during routine analysis, I can gain additional insight into the effects that IsoLab analytical procedures may have on sample Δ_{47} values along with any systematic biases that may be induced during this process. Kernel density estimations of the distribution of replicates (Fig. 4.3) reveal that the standards feature skewed distributions towards higher Δ_{47} values, and in some cases contain bimodal distributions. For the carbonate standards, the amount of skew appears to

be Δ_{47} dependent, with lower Δ_{47} standards displaying larger amounts of skew as compared to lower temperature standards. Because all standard materials were selected to be relatively homogenous in composition, I can reject sample heterogeneity as the cause of observed variability. Heated and equilibrated CO_2 gas standards, used to construct the absolute reference frame for correcting mass-dependent measurement biases (Dennis et al., 2011), also display skewed distributions when purified prior to analysis. Heated gasses that have not been purified do not have skewed distributions, and instead display a normal distribution with a standard deviation approaching the shot-noise limit for the mass spectrometer. Indeed, "blank" mass spectrometer analyses comparing the reference gas to itself have a similar normal distribution and uncertainty to the un-purified CO_2 standard (1SD = 0.027 ‰). These observations suggest that the CO_2 purification process is inducing analytical errors, biasing resulting measurements towards higher Δ_{47} values, or cooler temperatures. The one exception is the coldest equilibrated gas (t_4, equilibrated at 4°C), which displays a negative bias in Δ_{47} (higher temperature). Thus, it seems that some amount of purified sample replicates purified have reset, or partially reset, Δ_{47} values, biasing them towards a Δ_{47} value corresponding to room temperature CO_2 (0.94 ‰ at 23°C). We interpret this resetting to be driven by water vapor coming into contact with sample CO_2 during the purification process, allowing Δ_{47} values to re-equilibrate between the two gasses at the ambient temperature in the laboratory. While cryogenic CO_2 purification is designed to separate water vapor from sample CO_2, the two gasses may come into contact during sample dissolution, if the vacuum line is insufficiently evacuated between samples, or perhaps within the Poropak-Q GC resin. Pressures within the vacuum purification system are monitored throughout the

purification process, allowing excessive vapor pressures to be identified and samples to be flagged for potential resetting. Unexpected reactions within the Poropak-Q GC resin do not produce an observable signal during the CO_2 purification process, and presumably go unnoticed. IsoLab researchers suspect that reactions within the Poropak-Q GC resin are driving the observed resetting in the carbonate standards. Regardless of the driving cause of resetting, I can use our replicate standard measurements to characterize the effect of resetting and provide a correction for Δ_{47} values.

4.5.3 - Characterization of the Effects of Resetting During Purification of CO_2

Using the large number of replicate carbonate standard analyses measured in IsoLab, resampling methods can be used to simulate the behavior of unknown samples with smaller numbers of replicate analyses. For each of the seven carbonate standards used in IsoLab at the University of Washington, I resampled 10,000 synthetic samples containing five replicates each, which is the same number of replicates collected for most sample unknowns in this study. By comparing the population of synthetic samples to the accepted values for our standards, I can characterize the effect of partial resetting of Δ_{47} values during CO_2 purification and how it affects the interpreted Δ_{47} value. For a set of replicates from a given sample, it is standard practice to use the mean Δ_{47} value to calculate the growth temperature of the mineral. Taking the mean for each of the 5-replicate synthetic samples from our standards, I can compare the distribution of means for each standard to their accepted values (Fig. 4.4a). For all carbonate standards, the distributions of replicate means have normal distributions with mean values that overestimate the accepted Δ_{47} value. The magnitudes of the overestimation, as well as the

variances for the distributions, are inversely correlated with the accepted Δ_{47} value, consistent with greater effects of resetting in standards that are further from room temperature.

Using the standard deviation of "blank" analyses on the mass spectrometer to estimate the analytical reproducibility without the added error from the prepline), I can test how often the replicate mean falls within an expected range of the accepted value. Results are given in Table 4.3. For standards with formation temperatures below ~25°C (Coral, ETH3) the effect of resetting is relatively minor, with replicate means falling within one SD of the accepted value over 80% of the time and within two SD over 98% of the time. Both of these exceed the expected 68% and 95% occurrences for one and two SD, respectively, around the accepted value. Standards with accepted formation temperatures between 50°C and 100°C (C64, C2, ETH4) did not perform as well. Only C64 exceeded the expected accuracies, but by much smaller margins as compared to the lower temperature standards: 69% within one SD and 96% within two SD. For the two standards with the hottest accepted formation temperatures (ETH1 and ETH2), less than 35% of replicate means fell within one SD of the accepted value, and less than 65% fell within two SD. These results indicate that using the mean of five replicates provides a good estimate of the true temperature for carbonate formed around earth surface temperatures. At temperatures above ~50°C, however, the effect of resetting can generate significant errors in the replicate mean, even becoming statistically *unlikely* to reproduce the true value.

Because resetting of Δ_{47} values during CO_2 purification biases measurements towards room temperature and higher Δ_{47} values, I can assume the lowest Δ_{47} values from

each set of replicates are the least affected. If I take the lowest Δ_{47} value from each of the five-replicate synthetic samples taken from our population of standards, the distributions for each standard have the opposite effect as the replicate mean, biasing the estimated Δ_{47} value towards lower values (Fig. 4.4b). However, in contrast to the replicate mean, the magnitude of the underestimation and associated variance is not temperature dependent. For low-temperature standards, the minimum Δ_{47} value tends to underperform the replicate mean at both one and two SD levels (Table 4.3). However, for standards with formation temperatures above 50°C, using the minimum Δ_{47} value outperforms the replicate mean in estimating the accepted Δ_{47} value. When comparing to the expected reproducibility for one and two SD, only the hottest temperature standards (ETH1 and ETH2) underperform relative to the expected analytical error.

The magnitude of offset between the minimum Δ_{47} value and the accepted value for all seven carbonate standards is highly consistent (mean = 0.019 +/- 0.004 ‰). Considering this consistency, I explored the effect of using this mismatch to correct for bias in minimum Δ_{47} values. For each of the synthetic five-replicate samples, I added the mean offset value to the minimum Δ_{47} value. The distributions of these corrected values for each standard are shown in Figure 4.4c. For all seven standards, the corrected Δ_{47} value exceeds the expected reproducibility at both the one and two SD levels (Table 4.3). Thus, it appears that the effect of resetting during the CO_2 purification stage can be corrected by applying a small scalar correction factor to the lowest Δ_{47} value from a set of replicates. This approach should be applicable to any laboratory experiencing similar resetting during the CO_2 purification stage of analysis with sufficient instrument stability to generate large numbers of replicate analyses of carbonate standards, although the

magnitude of the correction factor will be related to the number of sample replicate analyses and will likely be laboratory dependent. I apply this new "offset minimum" correction to the samples analyzed in this study and discuss its effects on interpreted temperature below.

4.5.4 - Comparison of Clumped Isotope and Fluid Inclusion Temperatures

Combining clumped isotope temperatures with fluid inclusion temperatures provides an additional line of support for the interpreted formation temperature of a carbonate mineral. Because the fluid inclusion homogenization temperature (Th) can be interpreted as the minimum trapping temperature for the fluid (Goldstein, 2001), a clumped isotope temperature ($T(\Delta_{47})$) can be expected to be of equal or higher magnitude. The difference between Th and $T(\Delta_{47})$ is related to the fluid pressure during mineral growth. In most settings, pressure within the Earth is not expected to exceed lithostatic conditions, placing an upper limit on the expected difference between Th and $T(\Delta_{47})$. If either of these expected relationships is violated, the temperatures (and pressures) cannot be taken to represent the conditions during primary mineral growth. One, or both, of the temperature proxies must have experienced alteration since formation of the mineral.

A comparison of the clumped isotope and fluid inclusion temperatures for our samples is provided in Figure 4.5. These data demonstrate how the interpretation of replicate analyses can affect the accuracy and interpretation of clumped isotope measurements. Using the mean Δ_{47} value to estimate an apparent clumped isotope temperature, only three samples have temperatures within the expected range for the two

methods (see three points below the 1:1 line in Fig. 4.5a). All other samples have apparent clumped isotope temperatures that are less than the homogenization temperature. Six of these samples have clumped isotope temperatures that are within the 95% CI of the homogenization temperature, but most are at the upper limit of uncertainty and uncertainties are large. Clumped isotope temperatures calculated using our method for correcting the minimum Δ_{47} value from a set of replicate analyses provide results that are much more consistent with fluid inclusion homogenization temperatures (Fig. 4.5b). Only four out of thirteen samples have corrected clumped isotope temperatures that are lower than their homogenization temperatures (four points below the 1:1 line in Fig. 4.5b), one of which is within analytical uncertainty. Considering the increased consistency in expected temperature relationships, I take the corrected clumped isotope values as the preferred temperatures for this study.

For the nine samples with expected clumped isotope and fluid inclusion temperature relationships (Fig. 4.4b), these temperatures can be combined to estimate the fluid pressure during mineral growth (e.g. Luetkemeyer, 2014; Honlet et al., 2018). Using the equations of state of Zhang and Frantz (1987), I calculated the apparent trapping pressures for these samples (Fig. 4.6). Errors in clumped isotope temperature were calculated using the standard deviation of internal carbonate standard c64 (1SD = 0.0332), representing the minimum uncertainty expected for carbonate samples. Assuming a crustal density of 2700 kg/m^3 and a geothermal gradient of 20°C/km, none of the samples have pressure estimates that exceed lithostatic conditions. All samples have 95% CI that include hydrostatic conditions, as would be expected for carbonate formed within an open hydrologic system. Depending on the geologic setting, different regions

may be expected to have different geothermal gradients, which would cause pressure estimates to deviate from the hydrostatic pressure line in Figure 4.6. However, it should be noted that the minimum uncertainties for these samples are too large to explicitly distinguish between surface and hydrostatic pressures.

Despite the uncertainties in our measurements, our central pressure and temperature estimates can begin to highlight potential implications for the fault-fluid system. Three samples (MCE15-KH02, TMG15-KH03, and "3-5 to PT-1/S-7") have estimated pressures that are slightly above hydrostatic conditions for a 20°C geothermal gradient, and may be interpreted to have formed in an open hydrologic system in thermal equilibrium with a typical geothermal gradient. The remaining six samples have pressure estimates that are below the 20°C hydrostatic line, approaching surficial pressure conditions. Increasing the geothermal gradient results in a shallower slope for hydrostatic conditions, which may explain some samples, such as sample MH-C-1799 from the Mountain Home geothermal borehole (Fig. 4.6). For samples with pressure and temperature estimates that fall well below expected regional hydrothermal conditions, the data may be interpreted as reflecting a fault-specific process. Two possible examples include:

1) *Locally elevated geothermal gradients*. Fault zones are known to channel fluid flow in some settings (e.g. Caine et al., 1996; Bense et al., 2013; Faulkner et al., 2010b), which may result in locally elevated geothermal gradients if fluid flow is rapid enough to prevent thermal equilibration with the surrounding host rock. Low pressures and elevated temperatures

would be expected in the case travertine formed from warm water emanating from a spring along a fault zone.

2) *Syn-faulting pressure conditions.* Fluid pressure directly affects the state of stress within a fault. The cyclic build up of fluid pressure during interseismic periods followed by rapid drops in fluid pressure during fault motion, or the "fault-valve" mechanism, is thought to be an important control on the seismic cycle, particularly for faults cutting mixed permeability sequences (e.g. Sibson, 1990; Williams et al., 2017; Sibson, 1992; Shelly et al., 2015; Petit et al., 1999). It has been suggested that rapid pressure drops during fault slip can cause coexisting fluids to boil, driving rapid mineralization within fractures (e.g. Sibson, 1987; Robert et al., 1995). Samples featuring low estimated formation pressures and elevated temperatures may also be interpreted as syn-tectonic in their formation history.

Differentiation between these processes may be achieved through external constraints on the fault fluid system, such as burial conditions at the time of vein formation or evidence of syn-tectonic crystal growth. To overcome the large analytical uncertainties associated with the temperature and pressure measurements, researchers could perform additional clumped isotope replicate analyses or collect suites of contextually-related samples.

For the three samples with temperature estimates that violate the expected relationships between clumped isotope and fluid inclusion measurements, the data may still provide information regarding the sample history following primary mineral growth.

Indeed, for studies looking at alteration or diagenetic processes this information may be of great interest. In the case of a clumped isotope temperature that is cooler than the homogenization temperature, these values might be interpreted to reflect:

1) *Diagenetic alteration of the clumped isotope signal at lower temperature.* In the case of diagenetic alteration of the Δ_{47} value, some textural evidence of alteration may be visible in thin section under polarized light or cathodoluminescence. Complete recrystallization is not expected in this case, as it would also destroy the primary fluid inclusions.

2) *Higher-temperature re-equilibration or loss of integrity of the fluid inclusions.* Physical alteration of the fluid inclusions may occur in the absence of chemical alteration, allowing the inclusions to change size or communicate fluid with their surroundings (Goldstein, 2001; Bodnar, 2003). If the integrity of the inclusions is lost through leaking or communicating fluid, the damaged inclusions can often be identified during fluid inclusion analysis (Bodnar, 2003). The addition of clumped isotope analyses to samples with poorly preserved fluid inclusions would provide a way to test whether the analyzed inclusions were altered as well.

3) *Sampling inconsistency between methods.* Many carbonate features, particularly veins, can contain evidence for multiple stages of growth. In these cases, it is possible that different stages formed at different temperatures and pressures. The large amounts of sample required for

clumped isotope analysis may require homogenization of multiple stages of growth, while fluid inclusions may only be preserved in specific portions of a sample not representative of all growth stages. In this way, the different sampling approaches for the two methods may produce different temperature results.

Of the four samples with temperatures that do not follow the expected relationship, two are from the Moab Fault and two are from the Rocky Mountain Thrust Belt. Cementation along the Moab Fault was interpreted to have occurred over a range of temperatures during basin exhumation, resulting in the partial dissolution and re-precipitation of carbonate veins under progressively cooler temperatures (Hodson et al., *in review*). It is possible that the cooler than expected $T(\Delta_{47})$ values are a homogenization of carbonates with multiple temperatures, while the fluid inclusion measurements were made on the preserved primary material formed at higher temperature. In this case, fluid inclusion temperatures would reflect minimum primary growth temperatures and $T(\Delta_{47})$ reflects a combined primary and alteration temperature. The two samples from the Rocky Mountain Thrust Belt do not have a well-constrained alteration history. One sample, WS14-49, is poorly characterized for Δ_{47} with only two replicates. This sample also has an apparent bi-modal distribution of Th, suggesting there are multiple episodes of cementation within the sampled feature. The second sample, WS15-GCS, has a very small distribution of Th, suggesting that multiple generations of carbonate is not the cause of the temperature mismatch, and that at least one of the temperatures reflects alteration of the primary carbonate mineral.

4.6 - Conclusion

Through the combination of clumped isotope thermometry and fluid inclusion microthermometry, additional insight can be gained into the formation conditions and diagenetic histories of carbonate minerals. The use of carbonate standards to correct Δ_{47} measurements results in much higher accuracies when interpreting replicate Δ_{47} analyses, particularly in datasets with poor reproducibility. Corrected clumped isotope temperatures follow expected relationships with fluid inclusion temperatures much more faithfully than clumped isotope temperatures estimated by averaging replicate analyses, and produce pressure estimates that are within the expected range for fluids circulating within the upper crust.

Minimum uncertainties for clumped isotopes may be characterized by the long-term reproducibility of internal standards, even in the case of multiple sample replicates with smaller standard deviations. Sample uncertainties significantly greater than internal standards may be induced by analytical procedures such as purification of CO_2. Partial re-equilibration during CO_2 purification produces a systematic bias in measured Δ_{47} values at the University of Washington. Means of replicate analyses are most strongly affected in samples with lower Δ_{47} (higher temperature) compositions. Resampling from carbonate standards demonstrates that the true Δ_{47} value may be estimated by applying a scalar correction to the minimum Δ_{47} value in a set of replicate analyses.

Comparison of clumped isotope and fluid inclusion temperature estimates demonstrates the importance of how replicate clumped isotope analyses are interpreted. Using the replicate mean, most temperature estimates cannot be interpreted as primary growth conditions. In contrast, use of the corrected minimum Δ_{47} value yields

temperatures that predominantly follow expected temperature relationships with fluid inclusion microthermometry. Combination of fluid inclusion homogenization temperatures and clumped isotope temperatures allows estimation of pressure conditions during mineral growth. Calculated pressure estimates using our corrected minimum Δ_{47} values fall within the expected range for crustal fluids, falling around or below hydrostatic pressure conditions.

Our new method for using carbonate standards to correct for systematic biases is the first standards-based correction for clumped isotope analyses. While the clumped isotope community will likely adopt values for international standards in the near future, methods for correcting sample data using these standards are still being developed. Statistical analysis of large populations of replicate standard analyses is a powerful way to characterize the long-term behavior of our analytical procedures. By comparing our clumped isotope and fluid inclusion temperatures I demonstrate the importance of standards-based corrections on interpreted clumped isotope temperatures, which could be employed by any laboratory with sufficient numbers of replicate standard analyses.

4.7 - Figures

Figure 4.1: Examples of hand samples and thin section blanks containing carbonate veins and features used in this study. A) Sample NMF15-KH58 from the Moab Fault, featuring large, irregular carbonate veins in a silty host rock. B) Sample TMG15-KH03 from the Moab Fault, featuring a large crystalline carbonate vein in sandstone host rock. C) Sample 1-4/S-4 from the Hurricane Fault, featuring a wide, laminated vein and smaller irregular veins, which were used in this study. Pits in smaller veins are sampling locations for clumped isotopes. D) Sample 3-5 to PT-1/S-7 from the Hurricane Fault. Pits on upper side of thin section blank are sampling locations for clumped isotope analyses. E) Sample WS15-GCS from the Rocky Mountain Fold and Thrust Belt. F) Sample WS15-70 from the Rocky Mountain Fold and Thrust Belt.

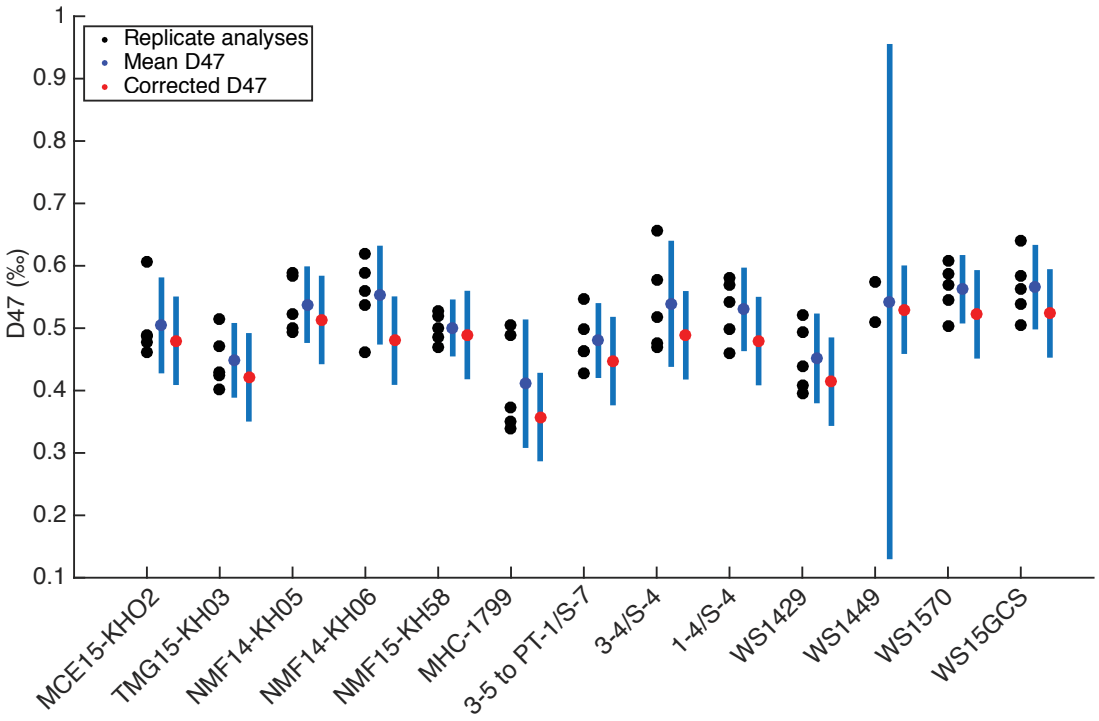

Figure 4.2: Replicate measurements for each sample analyzed in this study, along with means and corrected minimum Δ_{47} values. Errors for mean Δ_{47} values are 95% CI calculated using the standard error of replicate analyses. For samples with standard deviations less than that of internal standard C64 (1SD = 0.033), the standard deviation of the standard was used in its place. Errors for corrected minimum Δ_{47} values are 95% CI estimated using the standard deviation of the c64 internal standard.

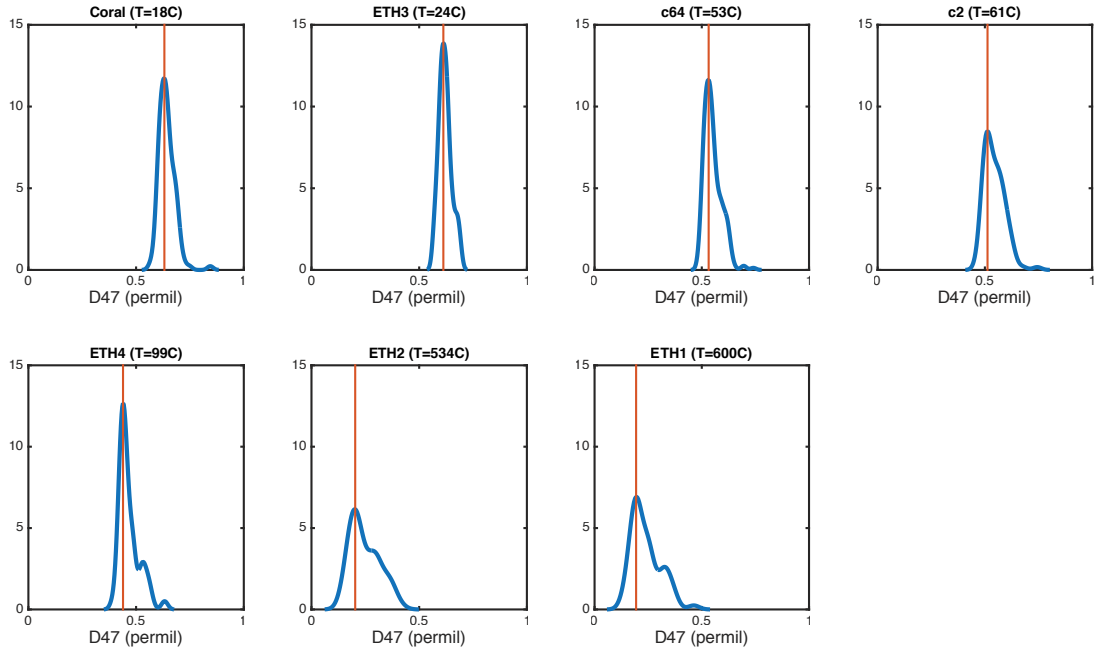

Figure 4.3: Distributions of replicate analyses for the seven carbonate standards routinely analyzed in IsoLab at the University of Washington. Blue lines are kernel density functions and orange lines represent position of modal value used as internally accepted value for each standard.

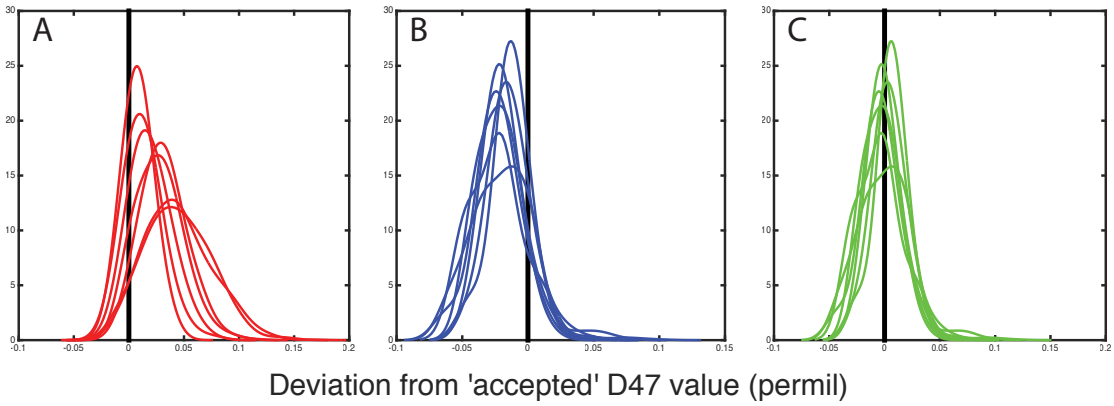

Figure 4.4: Results of resampling experiments from the seven carbonate standards. For each standard, 10,000 five-replicate samples were randomly extracted from the population shown in figure 2. A) Distributions of the deviations from the accepted value for the mean of each five-replicate sample. Each line represents a different standard. B) Distributions of the deviations from the accepted value for the minimum Δ_{47} value from each five-replicate sample. Each line represents a different standard. C) Distributions of the deviations from the accepted value for the corrected minimum Δ_{47} value from each five-replicate sample. Each line represents a different standard.

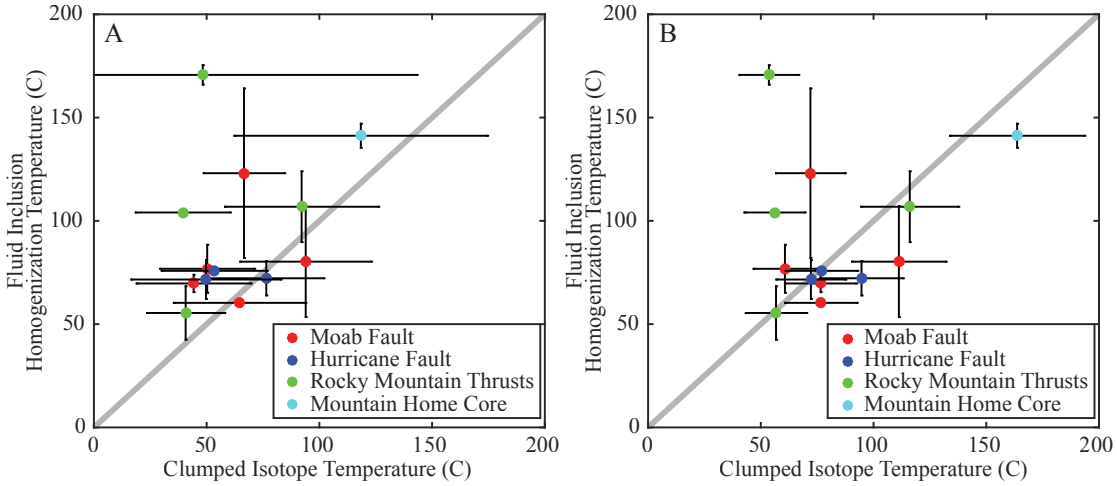

Figure 4.5: Comparison of fluid inclusion homogenization temperatures and clumped isotope temperatures. A) Comparison to clumped isotope temperatures calculated using the mean Δ_{47} value. Clumped isotope uncertainties are 95% CI based on the standard error of replicate analyses. B) Comparison clumped isotope temperatures that were corrected for error induced during purification of CO_2. Clumped isotope uncertainties are approximated using two SD from the internal standard C64 (1SD = 0.033 ‰). All fluid inclusion errors are represented as one standard deviation of measured homogenization temperatures.

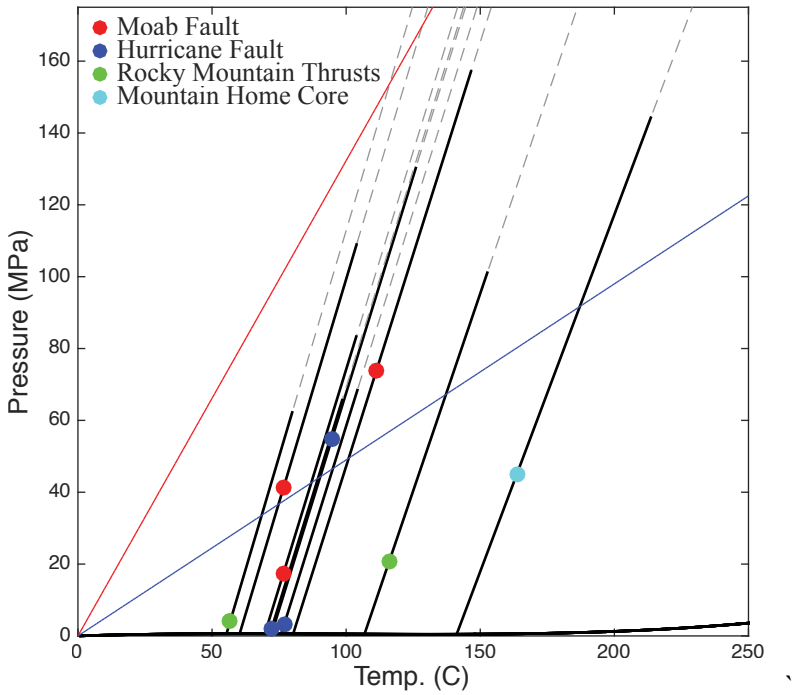

Figure 4.6: Isochore plot combining fluid inclusion and clumped isotope measurements to estimate ambient pressure during mineral growth. Thick black line is the liquid-vapor curve for aqueous solutions. Dashed grey lines are individual isochores for each sample. Red dots represent clumped isotope temperatures calculated using the corrected minimum Δ_{47} value. Black bars along isochores are estimated 95% CI for clumped isotope measurements using the standard deviation of internal standard C64 (1SD = 0.033 ‰). Red and blue lines represent lithostatic and hydrostatic conditions, respectively, calculated assuming a rock density of 2700 kg/m^3 and geothermal gradient of 20°C/km.

4.8 - Tables

Table 4.1 – Summary of temperature data:

Sample	n D47	Mean D47 (permil, ARF)	D47 SE	95% CI	Corrected D47 (permil, ARF)	T(D47)	T(D47) StdErr	T(D47) 95% CI	Corrected T(D47) (C)	n FI	Mean Th	Th SD
MCE15-KH02	5	0.504	0.026	0.072	0.480	65	11	29	77	3	60	2
TMG15-KH03	5	0.448	0.020	0.055	0.421	94	11	29	111	2	80	27
NMF14-KH05	5	0.538	0.020	0.057	0.513	50	8	21	61	2	77	12
NMF14-KH06	5	0.553	0.027	0.075	0.480	44	10	25	77	4	70	4
NMF15-KH58	5	0.500	0.015	0.041	0.489	67	5	18	72	4	123	41
MHC-1799	5	0.411	0.035	0.098	0.358	118	23	56	164	3	141	6
3-5 to PT-1/S-7	5	0.480	0.020	0.056	0.447	76	10	25	95	12	72	8
3-4/S-4	5	0.539	0.035	0.097	0.489	50	13	33	72	13	72	9
1-4/S-4	5	0.530	0.022	0.062	0.479	53	9	23	77	2	76	2
WS14-29	5	0.452	0.024	0.067	0.414	92	13	34	116	6	107	17
WS14-49	2	0.543	0.032	0.408	0.530	48	12	95	54	4	171	5
WS15-70	5	0.562	0.018	0.050	0.522	41	7	17	57	3	55	13
WS15-GCS	5	0.566	0.023	0.063	0.524	39	8	21	56	2	104	1

Table 4.2 – Replicate information and accepted values for carbonate standards.

Carbonate Standard	n (total)	Modal value (permil, ARF)[1]	n (cleaned)[2]	Standard Deviation (permil)[3]	Accepted (Meckler, permil)[4]	Accepted (Schauer, permil)[5]
c2	117	0.512	28	0.0397	-	-
c64	250	0.532	65	0.0332	-	-
coral	128	0.631	34	0.0325	-	-
ETH1	64	0.194	22	0.0519	0.267	0.205
ETH2	69	0.203	25	0.0527	0.269	0.199
ETH3	59	0.612	23	0.0295	0.705	0.612
ETH4	53	0.439	24	0.0289	0.524	0.453

1 modal value from all replicate analyses.
2 number of replicates passing Pierce Outlier test.
3 Standard deviation of cleaned replicate analyses.
4 Accepted values for international standards as reported in Meckler et al. (2014).
5 Accepted values for international standards as reported in Schauer et al. (2017).

Table 4.3 – Accuracies of interpreted D47 values from resampling analysis.

Carbonate Standard	Mean[1]		Minimum[2]		Corrected[3]	
	1 SD[4]	2 SD[4]	1 SD[4]	2 SD[4]	1 SD[4]	2 SD[4]
c2	0.43	0.85	0.79	1.00	0.92	0.98
c64	0.69	0.96	0.73	1.00	0.96	1.00
coral	0.84	0.98	0.57	0.93	0.90	1.00
ETH1	0.28	0.63	0.57	0.91	0.78	0.97
ETH2	0.29	0.63	0.56	0.99	0.77	0.98
ETH3	0.91	1.00	0.54	1.00	0.98	1.00
ETH4	0.54	0.89	0.90	1.00	0.95	1.00

1 Proportion of subsample means within 1 and 2 SD of accepted value
2 Proportion of subsample minimum D47 values within 1 and 2 SD of accepted value
3 Proportion of corrected subsample minimum D47 values within 1 and 2 SD of accepted values.
4 Reference standard deviation value taken from c64 carbonate standard.

Chapter Five

Conclusion

As demonstrated in the preceding three chapters, clumped isotope thermometry is a powerful tool for investigating the formation and diagenetic conditions associated with carbonate minerals. By application of this method to fault-hosted carbonates along the Moab Fault, I am able to characterize new aspects of the interrelated fault-fluid system that would not have been possible using more standard stable isotope techniques. At Courthouse Junction along the Moab fault, successive deformation mechanisms were associated with fluid flow at distinct temperature ranges and from distinct sources. My findings suggest that fluids circulated through the fault zone beginning at the earliest stages of deformation band formation and continued following the formation of fracture networks during the main episode of faulting.

Using this framework to provide context for more widely spaced samples in a fault-wide study, I found that the same deformation and cementation history was generally applicable to the whole fault system. These data suggested that fluid flow and cementation associated with the main stage of faulting continued throughout subsequent exhumation of the fault zone, over a period of ~60 Ma. Associated fluids were rock-buffered, suggesting low fluid-to-rock ratios. The distribution of cement compositions can not be explained by gradients in displacement-related deformation or lithologic composition of the fault zone, but appear to be localized near areas of high structural

complexity and fault segment interaction. This pattern indicates that fault zone geometry controlled the distribution of permeability along the Moab Fault.

In my final chapter, I address come of the potential complications associated with the application of clumped isotopes to high temperature systems, such as fault zone cementation. Expected relationships between clumped isotope temperatures and temperatures measured with the complementary fluid inclusion microthermometry technique allow diagenetically altered samples to be identified and their temperatures interpreted accordingly. In addition, I use carbonate standards to develop a new correction for biased measurements induced during clumped isotope analysis. Together, my findings have provided insight into new aspects of fault-fluid interaction along the Moab Fault, particularly with regard to the timing and conditions for cementation, and have provided new approaches to interpreting clumped isotope measurements from samples formed under high temperature conditions. Clumped isotope thermometry is clearly a powerful tool for studying fault-fluid interaction, and I expect future applications to fault-hosted carbonate cements will help to better understand the complex relationships between fault zone deformation, permeability, and fluid flow across a wide range of structural settings.

Appendix 1

Investigating fluid sources using strontium isotope analysis

Prior isotopic analyses from the Moab Fault, UT have identified multiple episodes of cementation corresponding to two apparent source fluid chemistries and temperatures of formation (Hodson et al., 2016; Bergman et al., 2013; Eichhubl et al., 2009): 1) cool temperatures and a marine fluid source; and 2) warm temperatures and meteoric fluids that mixed with a carbon source with an enigmatic $\delta^{13}C$ value (See chapter two for further detail). Earlier workers attributed the unusual $\delta^{13}C$ values to complex reduction of hydrocarbons (Eichhubl et al., 2009), but similar values have also been ascribed to magmatic CO_2 in other areas in the Colorado Plateau (Shipton et al., 2004). Intrusion of a nearby, Oligocene-age laccolith (Nelson et al., 1992; Murray et al., 2016) overlaps with the inferred formation age of carbonate cements along the Moab Fault (Hodson et al., 2016), underscoring the potential importance of magmatic CO_2. Emplacement of a shallow laccolith within the Paradox Basin would be highly disruptive to basin hydrology, beyond the addition of a new CO_2 source. Heat from emplacement would decompose local limestones, providing additional CO_2, and alteration of topography and stratigraphy geometry during the intrusion process (Johnson and Pollard, 1973) may alter fluid pathways through the basin. In this sense, laccolith intrusion in the Paradox Basin could have major, yet unrecognized, effects on basin hydrology.

When paired with oxygen and carbon, Strontium stable isotope ratios are a powerful tool for characterizing carbonate source fluids (Banner, 1995). These isotopes do not fractionate significantly, making them particularly useful for identifying fluid

sources. Oligocene intrusions have distinctive Strontium isotope ratios relative to other source rock in the basins (Friedman and Huffman, 1998; Chan et al., 2000), allowing any contribution to be readily identified. Additionally, the limestone units in the Paradox Basin have differing Strontium isotope ratios (Chan et al., 2000). Cements formed from fluid that flowed through and dissolved different limestone units are expected to have Strontium isotope compositions that reflect the dissolved limestone. In this way, Strontium isotopes from carbonate cements could reveal which limestones fluids interacted with and the presence of a magmatic CO_2 source, providing insight into the depth of fluid circulation within the basin.

To try to differentiate different fluid sources within the Paradox Basin, I performed strontium isotope analyses on a suite of samples collected from the Moab Fault Zone (n=9), and one sample each from: 1) the Ten Mile Graben; 2) a travertine deposit associated with Crystal Geyser along the Green River; and 3) the Lisbon Valley Fault Zone. All sample preparation and analysis were performed in the Isotope Geochemistry Laboratory at the University of Washington. Between 25 and 500 mg of crushed sample material was reacted with dilute hydrochloric acid to extract carbonates from their siliciclastic host rock. Strontium was then isolated using a liquid chromatography column, and the isotope ratios were measured on a multi-collector mass-specrometer. Internal standard 08UW BCR-1 and a replicate of sample TMG15-KH03 were prepared during each session of column chemistry. Five replicates of TMG15-KH03 are given in Table A2, and have a standard deviation of $2.2*10^{-5}$. The mean value is presented in Table A1.

Strontium isotope results, along with associated oxygen, carbon, and clumped isotope data, are given in Table A1. Samples were found to have a wide range of Strontium isotope ratios from 0.70930 to 0.71276. Moab Fault samples have a similarly wide range of values from 0.70930 to 0.71131. No clear distinctions were found between samples from different locations or different generations of cement. Additionally, no clear relationships were found between Strontium isotope ratios, $\delta^{13}C$ values, $\delta^{18}O$ values, clumped isotope temperatures or source fluid $\delta^{18}O$ values.

In the Paradox Basin, possible sources of Strontium include Cretaceous seawater ($^{87}Sr/^{86}Sr \approx 0.7077$ to 0.7084; Veizer, 1989), Phanerozoic sediments ($^{87}Sr/^{86}Sr \approx 0.716$; Breit and Meunier, 1990), La Sal igneous rocks ($^{87}Sr/^{86}Sr \approx 0.7043$ to 0.7056; Breit and Meunier, 1990), and Pennsylvanian evaporates ($^{87}Sr/^{86}Sr \approx 0.70845$; Breit and Meunier, 1990). Measured isotope ratios from the Moab Fault have intermediate values, falling between the lower-valued seawater, evaporates, and igneous rocks and the higher valued Phanerozoic sediments. A similar range of values from hematite cements in the region were presented by Chan et al. (2000), who interpreted the wide range of values to reflect different proportions of Strontium mixing from different sedimentary sources. A possible igneous source of Strontium from the La Sal Mountains is still compatible with the data measured from the Moab Fault, but I can not explicitly differentiate between the range of potential sources with Strontium compositions below the measured values. Future work using Strontium isotopes my help differentiate between these source materials, but will likely require additional sampling designed to characterize spatial patterns in Strontium composition around potential Strontium sources.

Tables

Table A1 - Strontium, carbon, oxygen, and clumped isotope data

Sample Name	87/86	$\delta^{13}C$ (‰)	$\delta^{18}O$ (‰)	Δ_{47} (‰)	T(°C)	T Err	Fluid $\delta^{18}O$ (‰)	$\delta^{18}O$ Err	Lat.	Long
NMF14-KH04	0.71065	-5.54	-16.64	-	-	-	-	-	38.731676	-109.807196
CHJ15-KH08B	0.71008	-3.5	-20.9	0.534	51.60	8.08	-13.68	1.38	38.711539	-109.730813
NMF15-KH24	0.71111	-4.17	-17.71	0.4944	69.4	14.4	-7.61	2.29	38.731249	-109.805918
NMF15-KH58	0.70930	-3.74	-10.85	0.5049	64.4	11.5	-1.45	1.87	38.691198	-109.705828
NMF15-KH22A	0.71107	-3.8	-12.9	0.4858	74	8	-2.2	1.3	38.733989	-109.809839
NMF15-KH28	0.71131	-4.0	-16.5	0.5833	33	7	-12.5	1.3	38.737475	-109.815069
NMF15-KH41	0.70991	1.1	-8.2	0.6069	25	5	-5.7	1.2	38.708326	-109.747788
NMF15-KH53A	0.70945	-5.2	-18.1	0.5216	57	7	-10.0	1.2	38.705722	-109.723311
NMF15-KH53B	0.70948	-5.0	-10.1	0.6536	12	3	-10.5	0.5	38.705722	-109.723311
TMG15-KH03 (Average)	0.70997	-2.84	-15.03	0.4606	86.9	22.7	-2.36	3.36	38.830783	-109.979986
CG16-02	0.71276	-	-	-	-	-	-	-	38.934882	-110.139914
NLV14-JC04B	0.71001	-	-	-	-	-	-	-	38.244474	-109.278454

Table A2 - Replicate TMG15-KH03 strontium isotope analyses

Replicate number	87/86
1	0.70997
2	0.70995
3	0.71001
4	0.70996
5	0.70997

References Cited

Anderson, R.E., and Mehnert, H.H., 1979, Reinterpretation of the History of the Hurricane Fault in Utah: Rocky Mountain Association of Geologists Basin and Range Symposium, p. 145–165.

Antonellini, M., and Aydin, A., 1994, Effect of faulting on fluid flow in porous sandstones: Petrophysical Properties: American Association of Petroleum Geologists Bulletin, v. 78, p. 355–377, doi: 10.1306/8D2B1B60-171E-11D7-8645000102C1865D.

Antonellini, M.A., Aydin, A., and Pollard, D.D., 1994, Microstructure of deformation bands in porous sandstones at Arches National Park, Utah: Journal of Structural Geology, v. 16, p. 941–959, doi: 10.1016/0191-8141(94)90077-9.

Aydin, A., Borja, R.I., and Eichhubl, P., 2006, Geological and mathematical framework for failure modes in granular rock: Journal of Structural Geology, v. 28, p. 83–98, doi: 10.1016/j.jsg.2005.07.008.

Aydin, A., and Johnson, A.M., 1978, Development of Faults as Zones of Deformation Bands and as Slip Surfaces in Sandstone, *in* Rock Friction and Earthquake Prediction, p. 931–942.

Baedecker, M.J., Cozzarelli, I.M., Eganhouse, R.P., Siegel, D.I., and Bennett, P.C., 1993, Crude oil in a shallow sand and gravel aquifer: III. Biogeochemical reactions and mass balance modeling in anoxic groundwater: Applied Geochemistry, v. 8, p. 569–586.

Ballas, G., Fossen, H., and Soliva, R., 2015, Factors controlling permeability of cataclastic deformation bands and faults in porous sandstone reservoirs: Journal of Structural Geology, v. 76, p. 1–21, doi: 10.1016/j.jsg.2015.03.013.

Balsamo, F., Bezerra, F.H.R., Vieira, M.M., and Storti, F., 2013, Structural control on the formation of iron-oxide concretions and liesegang bands in faulted, poorly lithified cenozoic sandstones of the para??ba basin, Brazil: Bulletin of the Geological Society of America, v. 125, p. 913–931, doi: 10.1130/B30686.1.

Balsamo, F., and Storti, F., 2010, Grain size and permeability evolution of soft-sediment extensional sub-seismic and seismic fault zones in high-porosity sediments from the Crotone basin, southern Apennines, Italy: Marine and Petroleum Geology, v. 27, p. 822–837, doi: 10.1016/j.marpetgeo.2009.10.016.

Balsamo, F., Storti, F., and Gröcke, D., 2012, Fault-related fluid flow history in shallow marine sediments from carbonate concretions, Crotone basin, south Italy: Journal of the Geological Society, v. 169, p. 613–626, doi: 10.1144/0016-76492011-109.Fault-related.

Banner, J.L., 1995, Application of the trace element and isotope geochemistry of strontium to studies of carbonate diagenesis: Sedimentology, v. 42, p. 805–824.

Banner, J.L., and Hanson, G.N., 1990, Calculation of simulaneous isotopic and trace element variations during water-biomineral interaction with application to carbonate diagenesis: Geochimica et Cosmochimica Acta, v. 54, p. 3123–3137.

Bense, V.F., Gleeson, T., Loveless, S.E., Bour, O., and Scibek, J., 2013, Fault zone hydrogeology: Earth-Science Reviews, v. 127, p. 171–192, doi: 10.1016/j.earscirev.2013.09.008.

Berg, S.S., and Skar, T., 2005, Controls on damage zone asymmetry of a normal fault zone: Outcrop analyses of a segment of the Moab fault, SE Utah: Journal of Structural Geology, v. 27, p. 1803–1822, doi: 10.1016/j.jsg.2005.04.012.
Bergman, S.C., Huntington, K.W., and Crider, J.G., 2013, Tracing paleofluid sources using clumped isotope thermometry of diagenetic cements along the Moab Fault, Utah: American Journal of Science, v. 313, p. 490–515, doi: 10.2475/05.2013.03.
Bésuelle, P., 2001, Evolution of strain localisation with stress in a sandstone: Brittle and semi-brittle regimes: Physics and Chemistry of the Earth, Part A: Solid Earth and Geodesy, v. 26, p. 101–106, doi: 10.1016/S1464-1895(01)00032-1.
Bodnar, R.J., 2003, Reequilibration of fluid inclusions: Fluid inclusions: Analysis and Interpretation, p. 213–230.
Boggs, S., and Krinsley, D., 2006, Application of Cathodoluminescence Imaging to the Study of Sedimentary Rocks: New York, Cambridge University Press, 165 p.
Brand, W.A., Assonov, S.S., and Coplen, T.B., 2010, Correction for the 17O interference in δ(13C) measurements when analyzing CO2 with stable isotope mass spectrometry (IUPAC Technical Report): Pure and Applied Chemistry, v. 82, p. 1719–1733, doi: 10.1351/PAC-REP-09-01-05.
Breit, G.N., and Meunier, J.-D., 1990, Fluid inclusion, d18O, and 87Sr/86Sr evidence for the origin of fault-controlled copper mineralization, Lisbon Valley, Utah, and Slick Rock District, Colorado: Economic Geology, v. 85, p. 884–891.
Budd, D.A., Frost, E.L., Huntington, K.W., and Allwardt, P.F., 2013, Syndepositional Deformation Features In High-Relief Carbonate Platforms: Long-Lived Conduits for Diagenetic Fluids: Journal of Sedimentary Research, v. 83, p. 12–36, doi: 10.2110/jsr.2013.3.
Burgener, L., Huntington, K., Hoke, G., Schauer, A., Ringham, M., Latorre, C., and Díaz, F., 2016, Variations in soil carbonate formation and seasonal bias over >4 km of relief in the western Andes (30 °S) revealed by clumped isotope thermometry: Earth and Planetary Science Letters, v. 441, p. 188–199.
Caine, J.S., Evans, J.P., and Forster, C.B., 1996, Fault zone architechture and permeability structure: Geology, v. 24, p. 1025–1028, doi: 10.1130/0091-7613(1996)024<1025.
Cashman, S., and Cashman, K., 2000, Cataclasis and deformation-band formation in unconsolidated marine terrace sand, Humboldt County, California: Geology, v. 28, p. 111–114, doi: 10.1130/0091-7613(2000)28<111:CADFIU>2.0.CO;2.
Chan, M.A., Parry, W.T., and Bowman, J.R., 2000, Diagenetic Hematite and Manganese Oxides and Fault-Related Fluid Flow in Jurassic Sandstones, Southeastern Utah: AAPG Bulletin, v. 84, p. 1281–1310.
Chan, M.A., Parry, W.T., Petersen, E.U., and Hall, C.M., 2001, 40Ar/39Ar age and chemistry of manganese mineralization in the Moab and Lisbon fault systems, southeastern Utah: Geology, v. 29, p. 331–334, doi: 10.1130/0091-7613(2001)029<0331.
Crossey, L.J., Karlstrom, K.E., Springer, A.E., Newell, D., Hilton, D.R., and Fischer, T., 2009, Degassing of mantle-derived CO2 and He from springs in the southern Colorado Plateau region - Neotectonic connections and implications for groundwater systems: Bulletin of the Geological Society of America, v. 121, p.

1034–1053, doi: 10.1130/B26394.1.
Curewitz, D., and Karson, J. a, 1997, Structural settings of hydrothermal outflow: Fracture permeability maintained by fault propagation and interaction: Journal of Volcanology and Geothermal Research, v. 79, p. 149–168, doi: 10.1016/S0377-0273(97)00027-9.
Daëron, M., Blamart, D., Peral, M., and Affek, H.P., 2016, Absolute isotopic abundance ratios and the accuracy of Δ47 measurements: Chemical Geology, v. 442, p. 83–96, doi: 10.1016/j.chemgeo.2016.08.014.
Dale, A., John, C.M., Mozley, P.S., Smalley, P.C., and Muggeridge, A.H., 2014, Time-capsule concretions: Unlocking burial diagenetic processes in the Mancos Shale using carbonate clumped isotopes: Earth and Planetary Science Letters, v. 394, p. 30–37, doi: 10.1016/j.epsl.2014.03.004.
Davatzes, N.C., Eichhubl, P., and Aydin, A., 2005, Structural evolution of fault zones in sandstone by multiple deformation mechanisms: Moab fault, southeast Utah: Geological Society of America Bulletin, v. 117, p. 135–148, doi: 10.1130/B25473.1.
Defliese, W.F., Hren, M.T., and Lohmann, K.C., 2015, Compositional and Temperature Effects of Phosphoric Acid Fractionation on Δ47 Analysis and Implications for Discrepant Calibrations: Chemical Geology, doi: 10.1016/j.chemgeo.2014.12.018.
Defliese, W., and Lohmann, K., 2015, Non-linear mixing effects on mass-47 CO2 clumped isotope thermometry: Patterns and implications: Rapid Communications in Mass Spectrometry, v. 29, p. 901–909, doi: 10.1002/rcm.7175.
Dennis, K.J., Affek, H.P., Passey, B.H., Schrag, D.P., and Eiler, J.M., 2011, Defining an absolute reference frame for ‘ clumped ’ isotope studies of CO 2: Geochimica et Cosmochimica Acta, v. 75, p. 7117–7131, doi: 10.1016/j.gca.2011.09.025.
Dennis, K.J., and Schrag, D.P., 2010, Clumped isotope thermometry of carbonatites as an indicator of diagenetic alteration: Geochimica et Cosmochimica Acta, v. 74, p. 4110–4122, doi: 10.1016/j.gca.2010.04.005.
Doelling, H.H., 1985, Geology of Arches National Park: Salt Lake City, UT, Utah Geological and Mineral Survey.
Eagle, R.A., Schauble, E.A., Tripati, A.K., Tütken, T., Hulbert, R.C., and Eiler, J.M., 2010, Body temperatures of modern and extinct vertebrates from (13)C-(18)O bond abundances in bioapatite.: Proceedings of the National Academy of Sciences of the United States of America, v. 107, p. 10377–10382, doi: 10.1073/pnas.0911115107.
Eichhubl, P., Davatzes, N.C., and Becker, S.P., 2009, Structural and diagenetic control of fluid migration and cementation along the Moab fault, Utah: AAPG Bulletin, v. 93, p. 653–681, doi: 10.1306/02180908080.
Eichhubl, P., Hooker, J.N., and Laubach, S.E., 2010a, Pure and shear-enhanced compaction bands in Aztec Sandstone: Journal of Structural Geology, v. 32, p. 1873–1886, doi: 10.1016/j.jsg.2010.02.004.
Eichhubl, P., Hooker, J.N., and Laubach, S.E., 2010b, Pure and shear-enhanced compaction bands in Aztec Sandstone: Journal of Structural Geology, v. 32, p. 1873–1886, doi: 10.1016/j.jsg.2010.02.004.
Eichhubl, P., Taylor, W.L., Pollard, D.D., and Aydin, A., 2004, Paleo-fluid flow and deformation in the Aztec Sandstone at the Valley of Fire, Nevada—Evidence for the coupling of hydrogeologic, diagenetic, and tectonic processes: Geological Society of

America Bulletin, v. 116, p. 1120, doi: 10.1130/B25446.1.
Eiler, J.M., 2007, “Clumped-isotope” geochemistry—The study of naturally-occurring, multiply-substituted isotopologues: Earth and Planetary Science Letters, v. 262, p. 309–327, doi: 10.1016/j.epsl.2007.08.020.
Eiler, J.M., 2011, Paleoclimate reconstruction using carbonate clumped isotope thermometry: Quaternary Science Reviews, v. 30, p. 3575–3588, doi: 10.1016/j.quascirev.2011.09.001.
Evans, J.P., Forster, C.B., and Goddard, J. V., 1997, Permeability of fault-related rocks, and implications for hydraulic structure of fault zones: Journal of Structural Geology, v. 19, p. 1393–1404, doi: 10.1016/S0191-8141(97)00057-6.
Faulkner, D.R., Jackson, C. a. L., Lunn, R.J., Schlische, R.W., Shipton, Z.K., Wibberley, C. a. J., and Withjack, M.O., 2010a, A review of recent developments concerning the structure, mechanics and fluid flow properties of fault zones: Journal of Structural Geology, v. 32, p. 1557–1575, doi: 10.1016/j.jsg.2010.06.009.
Faulkner, D.R., Jackson, C. a. L., Lunn, R.J., Schlische, R.W., Shipton, Z.K., Wibberley, C. a. J., and Withjack, M.O., 2010b, A review of recent developments concerning the structure, mechanics and fluid flow properties of fault zones: Journal of Structural Geology, v. 32, p. 1557–1575, doi: 10.1016/j.jsg.2010.06.009.
Fernandez, A., Müller, I.A., Rodríguez-Sanz, L., van Dijk, J., Looser, N., and Bernasconi, S.M., 2017, A Reassessment of the Precision of Carbonate Clumped Isotope Measurements: Implications for Calibrations and Paleoclimate Reconstructions: Geochemistry, Geophysics, Geosystems, p. 1–12, doi: 10.1002/2017GC007106.
Ferry, J.M., Passey, B.H., Vasconcelos, C., and Eiler, J.M., 2011, Formation of dolomite at 40-80 C in the Latemar carbonate buildup, Dolomites, Italy, from clumped isotope thermometry: Geology, v. 39, p. 571–574, doi: 10.1130/G31845.1.
Fossen, H., and Bale, A., 2007, Deformation bands and their influence on fluid flow: AAPG Bulletin, v. 91, p. 1685–1700, doi: 10.1306/07300706146.
Fossen, H., Schultz, R.A., Shipton, Z.K., and Mair, K., 2007, Deformation bands in sandstone: a review: Journal of the Geological Society, v. 164, p. 755–769, doi: 10.1144/0016-76492006-036.
Foxford, K.A., Garden, I.R., Guscott, S.C., Burley, S.D., Lewis, J.J.M., Walsh, J.J., and Watterson, J., 1996, The field geology of the Moab Fault, *in* Geology and resources of the Paradox Basin: Utah Geological Association Guidebook 25, p. 265–283.
Foxford, K.A., Walsh, J.J., Watterson, J., Garden, I.R., Guscott, S.C., and Burley, S.D., 1998, Structure and content of the Moab Fault Zone, Utah, USA, and its implications for fault seal prediction, *in* Faulting, Fault Sealing and Fluid Flow in Hydrocarbon Reservoirs, Geological Society, London, Special Publications, 147, p. 87–103.
Friedman, J.D., and Huffman, A.C., 1998, Laccolith Complexes of Southeastern Utah: Time of Emplacement and Tectonic Setting - Workshop Proceedings: v. 2158.
Garden, I.R., Guscott, S.C., Burley, S.D., Foxford, K.A., Walsh, J.J., and Marshall, J., 2001, An exhumed palaeo-hydrocarbon migration fairway in a faulted carrier system, Entrada Sandstone of SE Utah, USA: Geofluids, v. 1, p. 195–213, doi: 10.1046/j.1468-8123.2001.00018.x.

Garzione, C.N., Auerbach, D.J., Jin-Sook Smith, J., Rosario, J.J., Passey, B.H., Jordan, T.E., and Eiler, J.M., 2014, Clumped isotope evidence for diachronous surface cooling of the Altiplano and pulsed surface uplift of the Central Andes: Earth and Planetary Science Letters, v. 393, p. 173–181, doi: 10.1016/j.epsl.2014.02.029.

Gasparrini, M., Bakker, R.J., and Bechstadt, T., 2006, Characterization of Dolomitizing Fluids in the Carboniferous of the Cantabrian Zone (NW Spain): A Fluid-Inclusion Study with Cryo-Raman Spectroscopy: Journal of Sedimentary Research, v. 76, p. 1304–1322, doi: 10.2110/jsr.2006.106.

Ghisetti, F., Kirschner, D.L., Vezzani, L., and Agosta, F., 2001, Stable isotope evidence for contrasting paleoflud circulation in thrust faults and normal faults of the central Apennines, Italy: J. Geophys. Res., v. 106, p. 8811–8825, doi: 10.1029/2000jb900377.

Ghosh, P., Adkins, J., Affek, H., Balta, B., Guo, W., Schauble, E.A., Schrag, D., and Eiler, J.M., 2006, 13C–18O bonds in carbonate minerals: A new kind of paleothermometer: Geochimica et Cosmochimica Acta, v. 70, p. 1439–1456, doi: 10.1016/j.gca.2005.11.014.

Gibson, R.G., 1998, Physical character and fluid-flow properties of sandstone-derived fault gouge, *in* Coward, M.P., Johnson, H., and Daltaban, T.S. eds., Structural geology in reservoir characterization, Geological Society of London Special Publication, v. 127, p. 83–97.

Goldstein, R.H., 2001, Fluid inclusions in sedimentary and diagenetic systems: Lithos, v. 55, p. 159–193, doi: 10.1016/S0024-4937(00)00044-X.

Götze, J., 2012, Application of Cathodoluminescence Microscopy and Spectroscopy in Geosciences: Microscopy and Microanalysis, v. 18, p. 1270–1284, doi: doi:10.1017/S1431927612001122.

Graham Wall, B.R., Girbacea, R., Mesonjesi, A., and Aydin, A., 2006, Evolution of fracture and fault-controlled fluid pathways in carbonates of the Albanides fold-thrust belt: AAPG Bulletin, v. 90, p. 1227–1249, doi: 10.1306/03280604014.

Guo, W., Mosenfelder, J.L., Goddard, W.A., and Eiler, J.M., 2009, Isotopic fractionations associated with phosphoric acid digestion of carbonate minerals: Insights from first-principles theoretical modeling and clumped isotope measurements: Geochimica et Cosmochimica Acta, v. 73, p. 7203–7225, doi: 10.1016/j.gca.2009.05.071.

Gutiérrez, F., 2004, Origin of the salt valleys in the Canyonlands section of the Colorado Plateau Evaporite-dissolution collapse versus tectonic subsidence: Geomorphology, v. 57, p. 423–435, doi: 10.1016/S0169-555X(03)00186-7.

He, B., Olack, G.A., and Colman, A.S., 2012, Pressure baseline correction and high-precision CO 2 clumped-isotope (δ 47) measurements in bellows and micro-volume modes: Rapid Communications in Mass Spectrometry, v. 26, p. 2837–2853, doi: 10.1002/rcm.6436.

Henkes, G.A., Passey, B.H., Grossman, E.L., Shenton, B.J., Perez-Huerta, A., and Yancey, T.E., 2014, Temperature limits for preservation of primary calcite clumped isotope paleotemperatures: Geochimica et Cosmochimica Acta, v. 139, p. 362–382, doi: 10.1016/j.gca.2014.04.040.

Hill, P.S., Tripati, A.K., and Schauble, E.A., 2014, Theoretical constraints on the effects

of pH, salinity, and temperature on clumped isotope signatures of dissolved inorganic carbon species and precipitating carbonate minerals: Geochimica et Cosmochimica Acta, v. 125, p. 610–652, doi: 10.1016/j.gca.2013.06.018.
Hilton, D.R., Ramírez, C.J., Mora-Amador, R., Fischer, T.P., Füri, E., Barry, P.H., and Shaw, a. M., 2010, Monitoring of temporal and spatial variations in fumarole helium and carbon dioxide characteristics at Poás and Turrialba Volcanoes, Costa Rica (2001-2009): Geochemical Journal, v. 44, p. 431–440.
Hodson, K.R., Crider, J.G., and Huntington, K.W. Segment-scale controls and diagenetic conditions associated with protracted post-deformation fluid migration along the Moab Fault, UT: Geological Society of America Bulletin,.
Hodson, K.R., Crider, J.G., and Huntington, K.W., 2016, Temperature and composition of carbonate cements record early structural control on cementation in a nascent deformation band fault zone: Moab Fault, Utah, USA: Tectonophysics, v. 690, Part, p. 240–252, doi: 10.1016/j.tecto.2016.04.032.
Honlet, R., Gasparrini, M., Muchez, P., Swennen, R., and John, C.M., 2018, A new approach to geobarometry by combining fluid inclusion and clumped isotope thermometry in hydrothermal carbonates: Terra Nova, p. 1–8, doi: 10.1111/ter.12326.
Huntington, K.W., Budd, D.A., Wernicke, B.P., and Eiler, J.M., 2011, Use of Clumped-Isotope Thermometry To Constrain the Crystallization Temperature of Diagenetic Calcite: Journal of Sedimentary Research, v. 81, p. 656–669, doi: 10.2110/jsr.2011.51.
Huntington, K.W., Ehlers, T.A., Hodges, K. V., and Whipp, D.M., 2007, Topography, exhumation pathway, age uncertainties, and the interpretation of thermochronometer data: Tectonics, v. 26, doi: 10.1029/2007TC002108.
Huntington, K.W., Eiler, J.M., Affek, H.P., Guo, W., Bonifacie, M., Yeung, L.Y., Thiagarajan, N., Passey, B., Tripati, A., Daëron, M., and Came, R., 2009, Methods and limitations of "clumped" CO2 isotope (Delta47) analysis by gas-source isotope ratio mass spectrometry.: Journal of mass spectrometry : JMS, v. 44, p. 1318–29, doi: 10.1002/jms.1614.
Huntington, K.W., and Lechler, A.R., 2015, Carbonate clumped isotope thermometry in continental tectonics: Tectonophysics, v. 647–648, p. 1–20, doi: 10.1016/j.tecto.2015.02.019.
Huntington, K.W., Wernicke, B.P., and Eiler, J.M., 2010, Influence of climate change and uplift on Colorado Plateau paleotemperatures from carbonate clumped isotope thermometry: Tectonics, v. 29, p. n/a-n/a, doi: 10.1029/2009TC002449.
Irwin, H., Curtis, C., and Coleman, M., 1977, Isotopic evidence for source of diagenetic carbonates formed during burial of organic-rich sediments: Nature, v. 269, p. 209–213, http://www.nature.com/nature/journal/v269/n5625/abs/269209a0.html (accessed June 2014).
Johansen, T.E.S., Fossen, H., and Kluge, R., 2005, The impact of syn-faulting porosity reduction on damage zone architecture in porous sandstone: an outcrop example from the Moab Fault, Utah: Journal of Structural Geology, v. 27, p. 1469–1485, doi: 10.1016/j.jsg.2005.01.014.
Johnson, A.M., and Pollard, D.D., 1973, Mechanics of Growth of Some Laccolithic Field

Observations, Gilbert's Model, Physical Properties and Flow of the Magma: Tectonophysics, v. 18, p. 261–309.
Kelson, J.R., Huntington, K.W., Schauer, A.J., Saenger, C., and Lechler, A.R., 2017, Toward a universal carbonate clumped isotope calibration: Diverse synthesis and preparatory methods suggest a single temperature relationship: Geochimica et Cosmochimica Acta, v. 197, p. 104–131, doi: 10.1016/j.gca.2016.10.010.
Kim, S., and O'Neil, J.R., 1997, Equilibrium and nonequilibrium oxygen isotope effects in synthetic carbonates: Geochimica et Cosmochimica Acta, v. 61, p. 3461–3475.
Kirschner, D.L., and Kennedy, L.A., 2001, Limited syntectonic fluid flow in carbonate-hosted thrust faults of the Front Ranges, Canadian Rockies, inferred from stable isotope data and structures: Journal of Geophysical Research, v. 106, p. 8827, doi: 10.1029/2000JB900414.
Kluge, T., John, C.M., Jourdan, A.-L., Davis, S., and Crawshaw, J., 2015, Laboratory calibration of the calcium carbonate clumped isotope thermometer in the 25-250°C temperature range: Geochimica et Cosmochimica Acta, v. 157, p. 213–227, doi: 10.1016/j.gca.2015.02.028.
Knipe, R.J., Fisher, Q.J., Clennell, M.R., Farmer, A.B., Harrison, A., Kidd, B., McAllister, E., Porter, J.R., and White, E.A., 1997, Fault seal analysis: Successful methodologies, application and future directions, *in* Hydrocarbon seals: Importance for exploration and production: Norwegian Petroleum Society Special Publication, v. 7, p. 15–40.
Koger, J., 2017, Spatio-temporal History of Fluid-rock Interaction in the Hurricane Fault Zone.
Laubach, S.E., Eichhubl, P., Hilgers, C., and Lander, R.H., 2010, Structural diagenesis: Journal of Structural Geology, v. 32, p. 1866–1872, doi: 10.1016/j.jsg.2010.10.001.
Lechler, A.R., Niemi, N.A., Hren, M.T., and Lohmann, K.C., 2013, Paleoelevation estimates for the northern and central proto-Basin and Range from carbonate clumped isotope thermometry: Tectonics, v. 32, p. 295–316, doi: 10.1002/tect.20016.
Lloyd, M.K., Eiler, J.M., and Nabelek, P.I., 2017, Clumped isotope thermometry of calcite and dolomite in a contact metamorphic environment: Geochimica et Cosmochimica Acta, v. 197, p. 323–344, doi: 10.1016/j.gca.2016.10.037.
Loyd, S.J., Corsetti, F.A., Eiler, J.M., and Tripati, A.K., 2012, Determining the Diagenetic Conditions of Concretion Formation: Assessing Temperatures and Pore Waters Using Clumped Isotopes: Journal of Sedimentary Research, v. 82, p. 1006–1016, doi: 10.2110/jsr.2012.85.
Lucic, G., Stix, J., and Wing, B., 2015, Structural controls on the emission of magmatic carbon dioxide gas, Long Valley Caldera, USA: Journal of Geophysical Research: Solid Earth, v. 120, p. 2262–2278, doi: 10.1002/2014JB011760.
Luetkemeyer, P.B., 2014, Combined Clumped Carbonate Thermometry - Fluid Inclusion Study: Investigating Pressure-Temperatrue Cconditions During Calcite Precipitation, Farnham Dome, East-Central Utah: Geological Society of America Conference Abstracts,.
Luetkemeyer, P.B., Kirschner, D.L., Huntington, K.W., Chester, J.S., Chester, F.M., and Evans, J.P., 2016, Constraints on paleofluid sources using the clumped-isotope

thermometry of carbonate veins from the SAFOD (San Andreas Fault Observatory at Depth) borehole: Tectonophysics, doi: 10.1016/j.tecto.2016.05.024.
Lund, W.R., Hozik, M.J., and Hatfield, S.C., 2007, Paleoseismic Investigation and Long-Term Slip History of the Hurricane Fault in Southwestern Utah: Paleoseismology of Utah, v. 14, p. 1–87.
McCaig, A.M., Wayne, D.M., Marshall, J.D., Banks, D., and Henderson, I., 1995, Isotopic and fluid inclusion studies of fluid movement along the Gavarnie Thrust, Cenral Pyrenees: reaction fronts in carbonate mylonites: American Journal of Science, v. 295, p. 309–343.
Meckler, A.N., Ziegler, M., Millán, M.I., Breitenbach, S.F.M., and Bernasconi, S.M., 2014, Long-term performance of the Kiel carbonate device with a new correction scheme for clumped isotope measurements: Rapid Communications in Mass Spectrometry, v. 28, p. 1705–1715, doi: 10.1002/rcm.6949.
Mook, W.G., 1986, 13C in atmospheric CO2: Netherlands Journal of Sea Research, v. 20, p. 211–223.
Murray, K.E., Reiners, P.W., and Thomson, S.N., 2016, Rapid Pliocene–Pleistocene erosion of the central Colorado Plateau documented by apatite thermochronology from the Henry Mountains: Geology, v. 44, p. G37733.1, doi: 10.1130/G37733.1.
Nelson, S.T., Davidson, J.P., and Sullivan, K.R., 1992, New age determinations of central Colorado Plateau laccoliths, Utah: Recognizing disturbed K-Ar systematics and re-evaluating tectonomagmatic relationships: Geological Society of America Bulletin, v. 104, p. 1547–1560, doi: 10.1130/0016-7606(1992)104<1547.
Nuccio, V.F., and Condon, S.M., 1996, Burial and thermal history of the Paradox Basin, Utah and Colorado, and petroleum potential of the Middle Pennsylvanian Paradox Basin, Reston, Virginia: U.S. Geological Survey Bulletin 2000-O: 1-41 p.
Ohtani, T., Fujimoto, K., Ito, H., Tanaka, H., Tomida, N., and Higuchi, T., 2000, Fault rocks and past to recent fluid characteristics from the borehole survey of the Nojima fault ruptured in the 1995 Kobe earthquake, southwest Japan: Journal of Geophysical Research: Solid Earth, v. 105, p. 16161–16171, doi: 10.1029/2000JB900086.
Olig, S.S., Fenton, C.H., McCleary, J., and Wong, I.G., 1996, The earthquake potential of the Moab Fault and its relation to salt tectonics in the Paradox Basin, Utah, *in* Geology and resources of the Paradox Basin: Utah Geological Association Guidebook 25, p. 251–264.
Parry, W.T., 1998, Fault-fluid composition from fluid-inclusion observations and solubilities of fracture-sealing minerals: Tectonophysics, v. 290, p. 1–26, doi: 10.1016/S0040-1951(98)00013-4.
Passey, B.H., and Henkes, G.A., 2012, Carbonate clumped isotope bond reordering and geospeedometry: Earth and Planetary Science Letters, v. 351–352, p. 223–236, doi: 10.1016/j.epsl.2012.07.021.
Petit, J.P., Wibberley, C.A.J., and Ruiz, G., 1999, “Crack-seal”, slip: A new fault valve mechanism? Journal of Structural Geology, v. 21, p. 1199–1207, doi: 10.1016/S0191-8141(99)00038-3.
Pevear, D.R., Vrolijk, P.L., and Lomgstaffe, F.J., 1997, Timing of Moab fault displacement and fluid movement integrated with burial history using radiogenic

and stable isotopes, *in* Geofluids II Extended Abstracts, p. 42–45.
Philit, S., Soliva, R., Labaume, P., Gout, C., and Wibberley, C., 2015, Relations between shallow cataclastic faulting and cementation in porous sandstones: First insight from a groundwater environmental context: Journal of Structural Geology, v. 81, p. 89–105, doi: 10.1016/j.jsg.2015.10.001.
Robert, F., Boullier, A.-M., and Firadous, K., 1995, Gold-quartz veins in metamorphic terranes and their bearing on the role of fluids in faulting: Journal of Geophysical Research, v. 100, p. 12,861-12,879.
Sample, J.C., Reid, M.R., Tobin, H.J., and Moore, J.C., 1993, Carbonate cements indicate channeled fluid flow along a zone of vertical faults at the deformation front of the Cascadia accretionary wedge (northwest U.S. coast): Geology, v. 21, p. 507–510, doi: 10.1130/0091-7613(1993)021<0507.
Schauble, E.A., Ghosh, P., and Eiler, J.M., 2006, Preferential formation of 13C–18O bonds in carbonate minerals, estimated using first-principles lattice dynamics: Geochimica et Cosmochimica Acta, v. 70, p. 2510–2529, doi: 10.1016/j.gca.2006.02.011.
Schauer, A.J., Kelson, J., Saenger, C., and Huntington, K.W., 2016, Choice of 17O correction affects clumped isotope (Δ47) values of CO2 measured with mass spectrometry: Rapid Communications in Mass Spectrometry, doi: 10.1002/rcm.7743.
Shackleton, N.J., 1986, Paleogene Stable Isotope Events: Palaeogeography, Palaeoclimatology, Palaeoecology, v. 57, p. 91–102.
Shackleton, N.J., and Kennett, J.P., 1975, Palaeotemperature history of the Cenozoic and the initiation of Antarctic glaciation: Oxygen and carbon isotope analysis in DSDP sites 277, 279 and 281: Deep Sea Drilling Project Reports and Publications, v. 29, p. 743–755, doi: 10.2973/dsdp.proc.29.117.1975.
Shelly, D.R., Taira, T., Prejean, S.G., Hill, D.P., and Dreger, D.S., 2015, Fluid-faulting interactions: Fracture-mesh and fault-valve behavior in the February 2014 Mammoth Mountain, California, earthquake swarm: Geophysical Research Letters, v. 42, p. 5803–5812, doi: 10.1002/2015GL064325.
Shipton, Z.K., Evans, J.P., Kirschner, D., Kolesar, P.T., Williams, A.P., and Heath, J., 2004, Analysis of CO2 leakage through "low-porosity" faults from natural reservoirs in the Colorado Plateau, east-central Utah, *in* Baines, S.J. and Worden, R.H. eds., Geological Storage of Carbon Dioxide - Geological Society Special Publication, p. 43–58.
Sibson, R.H., 1990, Conditions for fault-valve behavior, *in* Deformation Mechanisms, Rheology, and Tectonics, Geological Society Special Publication, p. 15–28.
Sibson, R.H., 1987, Earthquake rupturing as a mineralising agent in hydrothermal systems: Geology, v. 15, p. 701–704, doi: 10.1130/0091-7613(1987)15<701.
Sibson, R.H., 1992, Implications of fault-valve behaviour for rupture nucleation and recurrence: Tectonophysics, v. 211, p. 283–293, doi: 10.1016/0040-1951(92)90065-E.
Snell, K.E., Koch, P.L., Druschke, P., Foreman, B.Z., and Eiler, J.M., 2014, High elevation of the 'Nevadaplano' during the Late Cretaceous: Earth and Planetary Science Letters, v. 386, p. 52–63, doi: 10.1016/j.epsl.2013.10.046.

Solum, J.G., van der Pluijm, B.A., and Peacor, D.R., 2005, Neocrystallization, fabrics and age of clay minerals from an exposure of the Moab Fault, Utah: Journal of Structural Geology, v. 27, p. 1563–1576, doi: 10.1016/j.jsg.2005.05.002.

Spangler, L.E., Naftz, D.L., and Peterman, Z.E., 1996, Hydrology, chemical quality, and characterization of salinity in the Navajo aquifer in and near the Greater Aneth Oil Field, San Juan County, Utah:, http://books.google.com/books?id=XmfuAAAAMAAJ.

Stolper, D.A., and Eiler, J.M., 2015, The kinetics of solid-state isotope-exchange reactions for clumped isotopes: A study of inorganic calcites and apatites from natural and experimental samples: American Journal of Science, v. 315, p. 363–411, doi: 10.2475/05.2015.01.

Swanson, E.M., Wernicke, B.P., Eiler, J.M., and Losh, S., 2012, Temperatures and fluids on faults based on carbonate clumped-isotope thermometry: American Journal of Science, v. 312, p. 1–21, doi: 10.2475/01.2012.01.

Tindall, S.E., 2014, Simple calculations of fluid flow across jointed cataclastic deformation bands: Marine and Petroleum Geology, v. 57, p. 152–159, doi: 10.1016/j.marpetgeo.2014.05.016.

Tindall, S.E., and Davis, G.H., 2003, Joint spacing and distribution in deformation band shear zones: Geological Magazine, v. 140, p. 1–9, doi: 10.1017/S0016756802007082.

Tindall, S., and Eckert, A., 2015, Geometric and mechanical-stiffness controls on jointing in cataclastic deformation bands: Journal of Structural Geology, v. 77, p. 126–137, doi: 10.1016/j.jsg.2015.05.008.

Tobin, T.S., Schauer, A.J., and Lewarch, E., 2011, Alteration of micromilled carbonate δ18O during Kiel Device analysis: Rapid Communications in Mass Spectrometry, v. 25, p. 2149–2152, doi: 10.1002/rcm.5093.

Torabi, A., Fossen, H., and Braathen, A., 2013, Insight into petrophysical properties of deformed sandstone reservoirs: AAPG Bulletin, v. 97, p. 619–637, doi: 10.1306/10031212040.

Tripati, A.K., Hill, P.S., Eagle, R.A., Mosenfelder, J.L., Tang, J., Schauble, E.A., Eiler, J.M., Zeebe, R.E., Uchikawa, J., Coplen, T.B., Ries, J.B., and Henry, D., 2015, Beyond temperature: Clumped isotope signatures in dissolved inorganic carbon species and the influence of solution chemistry on carbonate mineral composition: Geochimica et Cosmochimica Acta, v. 166, p. 344–371, doi: 10.1016/j.gca.2015.06.021.

Trudgill, B.D., 2011, Evolution of salt structures in the northern Paradox Basin: controls on evaporite deposition, salt wall growth and supra-salt stratigraphic architecture: Basin Research, v. 23, p. 208–238, doi: 10.1111/j.1365-2117.2010.00478.x.

Veizer, J., 1989, Strontium Isotopes in Seawater Through Time: Annual Review of Earth and Planetary Sciences, v. 17, p. 141–167.

Watkins, J.M., and Hunt, J.D., 2015, A process-based model for non-equilibrium clumped isotope effects in carbonates: Earth and Planetary Science Letters, v. 432, p. 152–165, doi: 10.1016/j.epsl.2015.09.042.

Williams, R.T., Goodwin, L.B., Sharp, W.D., and Mozley, P.S., 2017, Reading a 400,000-year record of earthquake frequency for an intraplate fault: Proceedings of

the National Academy of Sciences, v. 114, p. 4893–4898, doi: 10.1073/pnas.1617945114.
Zaarur, S., Affek, H.P., and Brandon, M.T., 2013, A revised calibration of the clumped isotope thermometer: Earth and Planetary Science Letters, v. 382, p. 47–57, doi: 10.1016/j.epsl.2013.07.026.
Zhang, Y.G., and Frantz, J.D., 1987, Determination of the homogenization temperatures and densities of supercritical fluids in the system NaClKClCaCl2H2O using synthetic fluid inclusions: Chemical Geology, v. 64, p. 335–350, doi: 10.1016/0009-2541(87)90012-X.